Characterising the Multi-Scale Properties of Flocculated Sediment by X-ray and Focused Ion Beam Nano-Tomography

Jonathan Antony Thomas Wheatland

A thesis presented for the degree of
Doctor of Philosophy
in Engineering & Materials Science
Queen Mary University of London
September 2016

Queen Mary
University of London

Declaration of Originality

I, Jonathan Wheatland, confirm that the research included within this thesis is my own work or that where it has been carried out in collaboration with, or supported by others, that this is duly acknowledged below and my contribution indicated. Previously published material is also acknowledged below.

I attest that I have exercised reasonable care to ensure that the work is original, and does not to the best of my knowledge break any UK law, infringe any third party's copyright or other Intellectual Property Right, or contain any confidential material.

I accept that the College has the right to use plagiarism detection software to check the electronic version of the thesis.

I confirm that this thesis has not been previously submitted for the award of a degree by this or any other university.

Date:

Publications and Conference Presentations

This work has thus far contributed to the following journal publications:

Wheatland, J.A.T., Bushby, A.J., Spencer, K.L. (Submitted). Quantifying the structure and composition of flocculated suspended particulate matter using focused ion beam nanotomography. *Environmental Science and Technology*.

Wheatland, J.A.T., Bushby, A.J., Droppo, I.G., Carr, S.C., Spencer, K.L. (In preparation).

Presentations of this work have been given at the following conferences:

Wheatland, J.A.T., Bushby, A.J., Spencer, K.L., Carr, J.S. (May 2014). Visualising the 3D structure of fine-grained estuarine sediments; Preliminary interpretations of a novel dataset obtained via volume electron microscopy. EGU General Assembly Conference Abstracts, EGU2014-15783, Vienna, Austria.

Wheatland, J.A.T., Spencer, K.L., Carr, J.S., Bushby, A.J. (June 2014). 3D FIB-SEM tomography of complex flocculated sedimentary materials consisting of inorganic and organic phases in an aqueous medium. Microscience Microscopy Congress, Manchester, UK.

Wheatland, J.A.T., Spencer, K.L., Droppo, I.G., Carr, J.S., Bushby, A.J. (Dec 2014). 3D Multi-scale visualisation of complex flocculated natural sediments. Society of Electron Microscopy Technology, London, UK.

Wheatland, J.A.T., Bushby, A.J., Droppo, I.G., Carr, J.S., Spencer, K.L. (April 2015). Multi length scale imaging of flocculated estuarine sediments; Insights into their complex 3D structure. EGU General Assembly Conference Abstracts, EGU2015-781, Vienna, Austria.

Wheatland, J.A.T., Spencer, K.L., Droppo, I.G., Carr, J.S., Bushby, A.J. (June 2015). Correlative multi-scale volumetric microscopy of flocculated sediments. Microscience Microscopy Congress, Manchester, UK.

Wheatland, J.A.T., Bushby, A.J., Carr, J.S., Droppo, I.G., Spencer, K.L. (Sep 2015). Characterising the multi length scale properties of flocculated sediment. Estuarine and Coastal Sciences Association 55, London, UK.

Wheatland, J.A.T., Droppo, I.G., Spencer, K.L., Bushby, A.J. (Feb 2015). Structure of aquatic flocs using correlative volumetric microscopy. RMS Meeting: Electron Microscopy Characterisation of Organic-Inorganic Interfaces, London, UK.

Wheatland, J.A.T., Spencer, K.L., Droppo, I.G., Carr, J.S., Bushby, A.J. (Sep 2016). Multi length scale characterisation of estuarine flocs using correlative tomography. Estuarine and Coastal Sciences Association 56, Bremen, Germany.

Abstract

The hydrodynamic behaviour of fine suspended aqueous sediments, and stability of the bedforms they create once settled, are governed by the physical properties (e.g., size, shape, porosity and density) of the flocculated particles in suspension (flocs). Consequently, accurate prediction of the transport and fate of sediments and of the nutrients and pollutants they carry depends on our ability to characterise aqueous flocs. Current research primarily focuses on characterising flocs based on their external gross-scale (>1 μm) properties (e.g., gross morphology, size and settling velocity) using *in situ* techniques such as photography and videography. Whilst these techniques provide valuable information regarding the outward behaviour of flocculated sediment (i.e. transport and settling), difficulties associated with extracting 3D geometries from 2D projections raises concerns regarding their accuracy and key parameters such as density can only be estimated. In addition, they neglect to inform on the internal micro- and nano-scale structure of flocs, responsible for much of their behaviour and development. Transmission electron microscope (TEM) and environmental electron microscope may be used to obtain nano-scale information in, essentially, 2D but there is a large scale gap between this information and the macro-scale of optical techniques.

To address this issue this study uses 3D tomographic imaging over a range of spatial scales. Whilst commonly used in materials science and the life sciences, correlative tomography has yet to be applied in the environmental sciences. Threading together 3D X-ray micro-computed tomography (X-ray μCT) and focused ion beam nano-tomography (FIB-nt) with 2D TEM makes material characterisation from the centimetre to nanometre-scale possible. Here, this correlative imaging strategy is combined with a non-destructive stabilisation procedure and applied to the investigation of flocculated estuarine sediment, enabling the multi length-scale properties of flocs to be accurately described for the first time.

This work has demonstrated that delicate aqueous flocs can be successfully stabilised via a resin embedding process and contrasted for both electron microscopy and X-ray tomography imaging. The 3D information obtained can be correlated across all length-scales from nm to mm revealing new information about the structure and morphology of flocs. A new system of characterising floc structure can be defined based on the association of particles and their stability in the structure rather than simply their size. This new model refutes the postulate that floc structures are fractal in nature.

Acknowledgements

Funding and resources for this project have been provided by:

Engineering and Physical Sciences Research Council (EPSRC)

Queen Mary University London (through the Post Graduate Research Fund)

Environment Canada

I would like to thank my supervisors, Dr. Andy Bushby and Prof. Kate Spencer for their continuing guidance and support. They have had and continue to have an unflagging enthusiasm for this project and the potential that it holds, which remains inspiration and motivation. I am grateful for their vision in putting together the support for this project and the unique expertise that each of them has generously made available to me throughout my own learning process.

I would also like to thank Ian Droppo (Environment Canada) and the staff at McMaster University, Ontario (Canada), Ernie Spitzer and Marcia West for the opportunity to collaborate and for in-kind contributions of microscope time, training and expertise.

Thanks are due to the staff of the NanoVision Centre [Queen Mary University of London (QMUL)], Russel Bailey and Nadja Tarakina, for their camaraderie and professionalism, especially for the sharing of their time and expertise. Jemima Burden (MRC Laboratory for Molecular Cell Biology, University College London) is also acknowledged for her help with the preparation of the samples investigated in this study. Thanks is given to Lucy Diggens of the QMUL Geography laboratory, who not only helped scan floc samples using X-ray μCT but also provided tea and biscuits in to the bargain.

I gratefully thank my family and friends for their constant support, good sense and good humour. Thanks especially to my nieces and nephews for making me take time to play, and with the clarity of childhood, put moments of frustration into perspective. To Poppy and Tilly, our long walks have been so important in allowing me time to reflect on my work; thanks for your always unconditional love. To my parents, Sarah and Martin Wheatland, thank you for all those summers spent in Wales; for encouraging (putting up with) the collection of fossils and identification of rocks and endless questions. This paper is dedicated to the memory of my grandfathers, Gabby Tom and Grandad Tony, who first inspired and

encouraged me to cultivate an interest in the natural world around me. Finally, I would like to express profound thanks for my partner, Alexandra Waechter, who has been sounding board, editor and moral support. She has learnt more about flocs than she probably ever thought she would need to know and yet still manages to agree that they're interesting.

Table of Contents

Abstract ..... *iv*
Acknowledgements ..... *v*
Table of Contents ..... *vii*
List of Figures and Tables ..... *x*
Glossary of Terms ..... *xiv*

Chapter One: Introduction 1

1.1. Introduction 1
1.2. Flocculation in Natural Aquatic Environments 2
1.2.1. Properties and Behaviour of Inorganic and Organic Constituents 2
1.2.2. Flocculation; Mechanisms of Aggregation, Break-up, Settling and Recycling 5
1.3. Characterisation of Flocculated Sediment 8
1.3.1. Current Techniques for Characterising Flocs 8
1.3.2. Size and Shape 8
1.3.3. Fractal Description 9
1.3.4. Density and Porosity 10
1.3.5. Floc Structure 11
1.4. Correlative Tomography 14
1.4.1. Applications in Materials Science and the Life Sciences 14
1.5. Concepts Addressed in this Thesis 16
1.5.1. Research Aims and Objectives 16

Chapter Two: Method Development 17

2.1. Introduction 17
2.1.1. Correlative Workflow 18
2.2. Stage 1: Floc Acquisition and Preparation 18
2.2.1. Acquisition of Flocs 18

2.2.2. Stabilisation Procedure 20
2.3. Stage 2: Acquisition and Reconstruction of Correlative Datasets 22
2.3.1. Nanometre Datasets; 2D TEM-EDS and STEM 22
2.3.2. Micrometre Datasets; 2D SEM-EDS and 3D FIB-nt 23
2.3.3. Millimetre Datasets; 3D X-ray μCT 24
2.4. Stage 3: Processing and Analysis of Correlative Datasets 25

Chapter Three: Results 26

3.1. Introduction 26
3.2. 2D Datasets Obtained at the Nanometre-Scale 26
3.2.1. Introduction 26
3.2.2. 2D STEM Images and TEM-EDS Spectra 26
3.2.3. Summary 33
3.3. 2D and 3D Datasets Obtained at the Micrometre-Scale 33
3.3.1. Introduction 33
3.3.2. 2D SEM Images and SEM-EDS Maps 34
3.3.3. 3D FIB-nt 40
3.3.4. Summary 55
3.4. 3D X-ray μCT Dataset Obtained at the Millimetre-Scale 55
3.4.1. Introduction 55
3.4.2. 3D X-ray μCT 55
3.4.3. Summary 50
3.5. Description of the Co-Registered Datasets 50
3.5.1. Introduction 50
3.5.2. 2D and 3D Correlated Datasets 50
3.5.3. Summary 61

Chapter Four: Discussion 62

4.1. Introduction 62
4.2. Critical Assessment of the Floc Stabilisation Technique 62

4.3. Critical Evaluation of the Information Obtained at the Different Length-Scales 66
4.4. Critical Evaluation of Correlative Tomography 74
4.4.1. Merits of the Correlative Workflow 74
4.4.2. The Suitability of Correlative Tomography for Future Floc Studies 76
4.5. Implications of Findings 78

Chapter Five: Conclusion 80

5.1. Concluding Remarks 80
5.2. Future Improvements and Applications 81

References 84

Appendices 102

Appendix I – Sample Site Location 102
Appendix II – Stabilisation Procedure 102
Appendix III – Refining FIB-nt Volume Acquisition 104
III.a. Imaging Parameters 104
III.b. FIB Milling Parameters 105
Appendix IV – Supplementary Methodological Information 107
IV.a. FIB-nt and X-ray CT Data Reconstruction and Segmentation 107
IV.c. Registration of Multi-Modal, Multi-Scale Datasets 110

List of Figures and Tables

Figure 1.1. Flocculation in natural aquatic environments, illustrating the cycling of suspended particulate matter (SPM) and settled bed sediment. 1

Figure 1.2. Simplified representation of the atomic structure of clays and schematic showing the electrical double layer (EDL) associated with the surfaces of charged particles in suspension. 4

Figure 1.3. Particle interaction in suspension. 6

Figure 1.4. Conceptual model descripting the (fractal) organisation of flocs first proposed by Krone (1962). Adapted from Krone (1986). 10

Figure 1.5. Length-scales over which the imaging tehcniques commonly used to characterise floc propertise. 12

Figure 2.1. Length-scales over which the imaging tehcniques employed within correlative workflow operate. 17

Figure 2.2. Correlative workflow applied to the multi-scale imaging of aqueous flocs. 18

Figure 2.3. Multi-preparatory method used to stabilise aqueous flocs for ultrastructural analysis as described by Liss *et al*. (1996). Modified from Liss *et al*. (1996). 21

Figure 2.4. Microscope set up for FIB-nt. 25

Figure 3.1. Selection of dark field STEM images showing examples of commonly observed features and more 'exotic' objects. 28

Figure 3.2. Selection of spectra from TEM-EDS applied to common floc constituents and accompanying TEM bright field micrographs. 29

Figure 3.3. Selection of dark field STEM images showing examples of the three categories of intracellular integrity used as an indicator of the fidelity of stabilised flocs to their original structure. 30

Figure 3.4. TEM bright field micrographs showing examples of the different morphotypes of fibrillar EPS commonly observed within the floc samples. 31

Figure 3.5. Dark field STEM images showing examples of defects in the thin sections. 32

Figure 3.6. Individual STEM images and image montages that show the structure of the floc samples with nanometre resolution. 34

Figure 3.7. SEM images of a FIB milled cross-section generated using SEs and BSEs respectively and sub-sets isolating a cluster of inorganic particles and a bacterium. 37

Figure 3.8. BSE image montages of the entire cross-section of flocs S4 and S5 exposed within the section block-face of samples. 38

Figure 3.9. X-ray elemental maps collected from RoI S4.2 and S4.5, the locations of which on the sample block-face are shown in Figure 3.8. 41

Figure 3.10. X-ray elemental maps collected RoI S5.2 and S5.3, the locations of which on the sample block-face are shown in Figure 3.8. 42

Figure 3.11. Feature recognition in SEM images in 2D and 3D. 45

Figure 3.12. Sub-volume of the FIB-nt volume shown in Figure 3.15 (labelled S5.2-2). 46

Figure 3.13. 3D reconstructions of FIB-nt volume S3.1 and S3.5 based on SE and BSE images respectively. 48

Figure 3.14. 3D reconstruction of FIB-nt volume S5.2 based on BSE images generated in the 3D viewer in Fiji/ImageJ. 51

Figure 3.15. 3D reconstructions of FIB-nt volume S5.2 based on BSE images generated in Drishti. 52

Figure 3.16. 3D visualisations of the floc samples S4 and S5 rendered in Drishti. 57

Figure 3.17. Visualisation of the correlative datasets obtained from floc sample S4. 59

Figure 3.18. Visualisation of the correlative datasets obtained from floc sample S5. 60

Figure 4.1. Schematic showing the hierarchical structure of the aqueous floc samples revealed by the correlative datasets. 67

Figure AI.1. Map indicating the location of sampling site Canvey Island, Thames Estuary, SE England. 111

Figure AII.1. Flowchart outlining the steps taken in the stabilisation procedure. 112

Figure AIII.1. Effect of electron beam conditions (specifically current) on image contrast and resolution. 113

Figure AIII.2. The effects of selecting the wrong ion beam parameters. 114

Figure AIII.3. The successful preparation of an RoI for FIB-nt. 115

Figure AIV.1. Workflow outlining the steps taken in FIB-nt data reconstruction and processing in Fiji/ImageJ. 116

Figure AIV.2. Workflow outlining the steps taken in X-ray CT data reconstruction and processing in CT-Pro 3D and Fiji/ImageJ. 117

Figure AIV.3. Workflow outlining the steps taken during 3D data rendering, segmentation and visualisation. 118

Figure AIV.4. Flowchart outlining the steps taken to create dark-field STEM and SEM-BSE image montages. 119

Figure AIV.5. Flow diagram outlining the major steps taken for the registration of the multi-scale datasets and their co-visualisation. 120

Table 3.1. Ion and electron beam parameters during SEM imaging and serial sectioning. 36

Table 3.2. Volume fractions for the segmented components of sub-volume S5.2-2. 47

Table 3.3. Volume fractions for the segmented components of FIB-nt datasets S3.1 and S3.5. 49

Table 3.4. Volume fractions for the segmented components of FIB-nt volume S5.2. 50

Table 3.5. Scanning parameters selected for the acquisition of X-ray datasets. 56

Table 3.6. Difference in the segmentation results for the metal pins used for registration. 61

Glossary of Terms

Backscattered electron(s) (BSEs) – High-energy electrons of the incident beam which have interacted with the atoms of a sample and have been elastically scattered back out of the sample surface. Since the degree of scattering is a function of average atomic number, this signal provides valuable compositional information.

Beam hardening – Common artefact in X-ray CT imagery that results in the edges of objects appearing brighter than their centre (an artificial reduction in X-ray attenuation). This is caused by an increase in the mean energy of X-ray beam.

Block-face scanning electron microscopy (SEM) – Term used here to describe systematic SEM imaging of the sample block-face/working surface which enables the generation of a high-resolution image mosaic.

Born repulsion – Short range (nm) electrostatic force which develops at the contacts between colloidal particles. Results from the overlap between the electron clouds of the particles.

Bound EPS – Extracellular polymeric material excreted by microorganisms and attached tightly to their exterior, which provides a means of attachment, nutrient assimilation and protection from predation (see also EPS).

Broad ion beam tomography (BIB-tomography) – An imaging procedure which makes use of a broad ion beam (BIB, Argon ion source) SEM workstations, employing BIB for *in situ* milling and SEM for high-resolution imaging. In comparison to FIB, BIB enables the preparation of larger cross-sections (mm^2 as opposed to μm^2).

Capsular EPS – See Bound EPS.

Cation exchange capacity (CEC) – The total number of exchangeable cations a (clay) particle can absorb.

Co-registration – Procedure involving the alignment of correlative datasets in 3D space. This is often achieved using feature 'landmarks' or fiducial markers identifiable in each of the datasets being aligned.

Confocal laser scanning microscopy (CLSM) – An optical (3D) imaging technique which uses the principle of fluorescence excitation. Images are generated point-by-point rather than projected, significantly reducing out-of-focus light and thus increasing resolution beyond that of traditional conventional optical microscopy (see also COM).

Conventional optical microscopy (COM) – Microscopy technique which employs visual light and a series of lenses to illuminate and magnify images of a sample.

Correlative microscopy – An imaging strategy which uses several overlapping imaging modalities (usually 2D) to collect datasets at different length-scales from a single sample.

Derjaguin-Landau-Verwey-Overbeek (DLVO) Theory – Describes the balance of forces (electrostatic repulsion and van der Waals attraction) between two approaching (colloidal) particles in suspension.

Dissolved organic matter (DOM) – Broad classification of organic molecules found with aquatic environments (<1 μm) of varied origin and composition.

Electrical double layer (EDL) – Layer of charged particles which forms around the surface of a particle in the presence of a fluid.

Electron microscopy (EM) – Imaging technique which employs electrons as the primary means of image formation (see also SEM, STEM and TEM).

Elemental mapping – Procedure for mapping the elemental composition of a material by energy dispersive spectroscopy (EDS).

Energy dispersive spectroscopy (EDS) – Technique for localised chemical analysis, which makes use of the X-ray spectrum emitted by a material when bombarded with a beam of focused electrons.

Equivalent spherical diameter (ESD) – In floc research, the ESD of a floc is the diameter of a sphere of equivalent volume usually extracted from a 2D image.

Extracellular polymeric substances (EPS) – Natural polymers of high molecular weight commonly produced by microorganisms. particles are sticky ($\alpha > 0.1$)

Field emission gun (FEG) – A type of electron gun which is used to create a small, focused electron beam.

Focused ion beam nanotomography (FIB-nt) – A volumetric imaging technique which makes use of FIB-SEM workstation, combining FIB for *in situ* milling and SEM for high-resolution imaging.

Fractal dimension – In fractal geometry a fractal dimension is a measure of an object or pattern complexity. The greater the fractal index (1-3), the greater its complexity.

Fractal geometry/theory – Fractal geometry is a means of describing, measuring and predicting complex structures or patterns. Structure or patterns are assumed to be the same at all length-scales, i.e. they are self-similar.

Grey-scale(s)/level(s) – Value assigned to each pixel/voxel in an 2D image/3D volume based on the properties of the material.

Image stack/sequence – Sequence of images which represent a sampled volume. For FIB-nt, an image stack is the resulting images collected from the front face of the sample block as it is eroded/milled sequentially by the FIB. For X-ray CT, radiographs collected from a sample are used to reconstruct individual 2D images which form a stack.

Immobilisation – The process through which aqueous floc samples are stabilised for a short period of time (several days) in low-melting-point agarose. The addition of agarose prevents structural changes during transport, storage (short-term) and subsampling prior to chemical stabilisation.

Partial volume effect – Term given when a pixel contains two or more materials and the pixel value is some combination (an average) of the property being measured (e.g., X-ray attenuation). The partial volume effect is most noticeable at the edges of objects, causing them to be poorly defined.

Particulate organic matter (POM) – Coarse detrital organic material (>1 μm) commonly of varied origin and composition (e.g., leaf litter and pollen etc.).

Pixel – Alternatively picture element, pixels are single data points on a raster image.

Polymer bridging – Term used to describe the mechanism by which particles in suspension (e.g., clays and silt grains etc.) are bound together by extracellular polymers (EPS) commonly produced by microorganisms.

Reconstruction – The segmentation/classification of all materials within an 2D image or 3D volume.

Regions of interest (RoI) – Term used here to denote areas identified for further analysis (e.g., for FIB-nt) based on visual assessment of the working surface exposed within the floc.

Registration – Process by which 2D images or 3D volumes covering or containing a common region are brought into alignment.

Scanning electron microscopy (SEM) – An electron microscope technique which involves scanning a focused beam of electrons over a sample surface to produce an image. Images are the product of interactions between the electrons of the incident beam and the atoms of the sample which are subsequently recorded.

Scanning transmission electron microscopy (STEM) – An electron microscope technique in which images are formed by recording the degree to which electrons transmitted through ultrathin-sections obtained from a sample are scattered. Unlike traditional transmission electron microscopy (see also TEM) the electron beam is focused and scanned across the sample ultrathin-section in a raster.

Secondary electron(s) (SEs) – The product of inelastic interactions between incident beam electrons and the atoms of the sample. SEs are emitted from near the surface of the sample and offer primarily morphological information.

Serial sectioning – Process by which a surface is imaged and cut/milled sequentially to obtain an image stack for volumetric reconstruction.

Signal to noise ratio – The ratio of useful signal to unwanted background noise within an image.

Soluble/slime EPS – Extracellular material either loosely attached or unassociated with microbial cells (see also EPS).

Spatial resolution – Term which refers to the number of pixels/voxels that a 2D image or 3D volume is composed of.

Stabilisation – The process by which samples/specimens are rendered vacuum stable for electron microscopy.

Surficial fine-grained laminae (SFGL) – Transitional layer between the water-column and the bed composed of the most recently deposited (usually flocculated) material. This layer often exhibits a low density and high porosity.

Suspended particulate matter (SPM) – Collective name for material in suspension, which is usually further subdivided by size into fine (<63 μm) and coarse-grained (>63 μm) SPM.

Transmission electron microscopy (TEM) – High-resolution (atomic scale) microscopy technique in which a beam of high-energy electrons is transmitted through an ultrathin section taken from a sample of interest. Transmitted electrons are said to have experienced 'forward scattering' the degree to which is dependent on atomic number of the sample.

Trenching – Critical step in the preparation of selected RoIs for FIB-nt. Trenches are excavated on three sides of the RoI to minimise imaging artefacts resulting from the re-deposition of milled material, following which the front trench is extended to reveal a surface for imaging with the electron beam.

van der Waals attraction – Weak attractive force between atoms and molecules. Responsible for cohesive properties exhibited by fine (clay) sediments.

Visualisation – The process of qualitatively analysing a sampled volume (via imaging software, e.g., Drishti) prior to quantitative analysis. Enables the identification of areas/features of interest.

Volumetric rendering – 3D visualisation(s) produced of a reconstructed/segmented data volume.

Volumetric microscopy – Alternative term for FIB-nt (see also FIB-nt).

Voxel - In a 3D dataset, the minimum volume element; analogous to a 2D picture element or 'pixel'.

X-ray computed tomography (X-ray CT) – A non-destructive analytical technique used for 3D visualisation and investigation of the internal composition and structure of materials based upon the principle of X-ray attenuation.

Chapter One: Introduction

1.1. Introduction

Within natural aquatic environments fine-grained (<63 μm) suspended particulate matter (SPM) is typically present as cohesive flocs, irregularly shaped structures consisting of microbial cells, bioorganic matter, minerogenic particles, and fluid-filled pore space (Kranck & Milligan, 1992; Liss *et al*., 1996; Droppo, 2001; Leppard & Droppo, 2005; Burd & Jackson, 2009). The physical properties of flocs, which reflect the combined interactions between various physical, chemical and biological processes (Figure 1.1), alter the

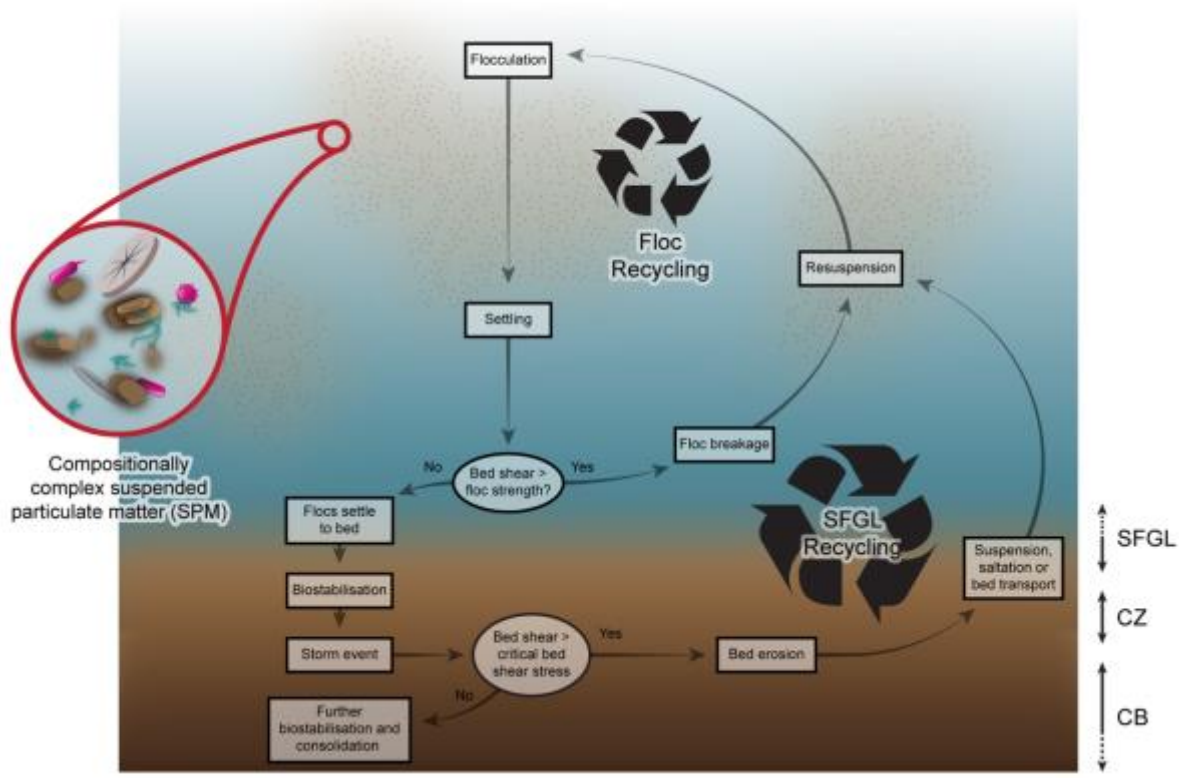

Figure 1.1. Flocculation in natural aquatic environments, illustrating the cycling of suspended particulate matter (SPM) and settled material. According to Droppo & Stone (1994) the bed is composed of three distinct layers: *Surficial Fine-Grained Lamina* (*SFGL*) – uppermost layer (~8 mm) of the bed composed of recently deposited material characterised by its 'fluffy' nature and high porosity and water content (Dyer, 1986); *Collapse Zone* (*CZ*) – transition zone between the SFGL and consolidated bed (CB) composed of material undergoing biostabilisation (usually 2 – 4 mm below bed surface and extending to a depth of 10 mm); *Consolidated Bed* (*CB*) – material that has been compacted following self-weight consolidation, the density of which remains relatively constant with depth (Droppo & Amos, 2001). Adapted from Droppo *et al*. (2001).

hydrodynamic behaviour of their constituents and dictate the stability of the landforms they create once settled (Bennett *et al.*, 1991; Droppo, 2001; Garcia-Aragon *et al.*, 2011; Grabowski *et al.*, 2011). Accurate quantification of floc properties is therefore critical for predicting the downward flux and transport patterns of sediment, as well as the impact and eventual fate of sediment-bound contaminants and nutrients (Droppo *et al.*, 1996; Williams *et al.*, 2008; Manning *et al.*, 2010; Droppo *et al.*, 2000; 2001; Baas *et al.*, 2013). However, unlike coarse-grained sediment (>63 μm) the properties of which can be measured with relative ease, the fragility and multi-scale structure of flocs makes both their sampling and characterisation problematic (Buffle & Leppard, 1995a; Liss *et al.*, 1996; Droppo *et al.*, 1996; Manning *et al.*, 2011).

Research related to suspended sediment has typically taken a top-down approach to floc characterisation, using *in situ* techniques such as photo- and videography to measure their external millimetre-scale properties (e.g., gross size, shape and settling velocity) (e.g., Eisma *et al.*, 1986; Dyer *et al.*, 1996; Manning & Dyer, 2002a; Mikkelsen *et al.*, 2004). These techniques are useful, providing valuable information regarding the outward behaviour of flocculated sediment (i.e. transport and settling). However, there are difficulties associated with extracting 3D geometries from 2D projections which raises concerns regarding their accuracy and many characteristics critical to predicting their dynamic behaviour e.g., density and porosity, are derived from these 2D projections may assumptions of spherical shape. In addition, these techniques neglect to inform on the internal structure of flocs, which is believed to be responsible for much of their behaviour and development (Liss *et al.*, 1996; Droppo, 2001). While high-resolution techniques exist that enable the analysis of nano- and micro-scale floc structure e.g., transmission electron microscopy (TEM) and scanning electron microscopy (SEM), methods for relating internal structure to outward morphology and behaviour have not yet been fully developed.

1.2. Flocculation in Natural Aquatic Environments

1.2.1. Properties and Behaviour of Inorganic and Organic Constituents

Cohesive sediment or 'mud' is ubiquitous in most aquatic systems, and consists of a complex mixture of inorganic particles, organic material, water and gas (Bennett *et al.*, 1991; Winterwerp & van Kesteren, 2004; Grabowski *et al.*, 2011). The relative proportions of these constituents vary both spatially and temporally, changing between freshwater, brackish and

saltwater environments, and also seasonally and with depth (Uncles *et al*., 1998; Chen *et al*., 2005; Verney *et al*., 2009; Manning *et al*., 2010).

The mineral solids fraction of natural sediment, either settled or in suspension, is usually comprised of a mixture of particle sizes ranging from fine clays (diameter, <2 μm) to coarser silts and sand-sized grains (diameter, 2 – 63 μm and >63 μm respectively). In cohesive sediments, the particle size distribution tends to be skewed towards finer materials (i.e. clays and silts). Clay minerals are characterised by their small size, flat platy morphology, large surface area to mass ratio and electrical charge (Bennett & Hulbert, 1986; Mitchell & Soga, 2005). Due to their unique properties clays are highly electro-chemically active, and are mainly responsible for the cohesive nature of fine-grained sediment (Winterwerp & van Kesteren, 2004). Unlike *tectosilicates* such as quartz and feldspar, the atoms of which are bonded into a three-dimensional framework, clays are multi-layered structures (so-called *phyllosilicates*) that consist of 2-dimensional sheets of silica tetrahedra and aluminium or magnesium octahedra (Figure 1.2) (Grim, 1968; Gillott, 1987; Mitchell & Soga, 2005). The sequence in which these layers are stacked determines the group to which a clay mineral belongs. Amongst the more common clay minerals are kaolinite, illite, montmorillonite and chlorite (Bennett & Hulbert, 1986; Winterwerp & van Kesteren, 2004).

Most clay minerals exhibit a net negative charge that is a result of two distinct types of surface charges: (i) a permanent negative charge on their flat faces due to isomorphic substitutions within the clay mineral structure; and (ii) a variable charge at their edges, which is dependent on mineralogy and water chemistry (i.e. pH) (Figure 1.2) (Grim, 1968; Dyer, 1986; Bennett *et al*., 1991; Furukawa *et al*., 2009). In solution, mobile oppositely charged ions interact with clay minerals to establish what is known as an electrical double layer (EDL) at the solid-liquid interface (Mitchell & Soga, 2005; Curry *et al*., 2009; Grabowski *et al*., 2011). A consequence of this is that similarly charged particles will experience electrostatic repulsion when in close proximity, preventing particle-to-particle interaction through short range molecular van der Waals forces (see § 1.2.2 and Figure 1.3). Early models hypothesising the structure of sediment proposed that clay minerals behaved as single plate particles (e.g., Terzaghi, 1925; Casagrande, 1932; Lambe, 1958), however, numerous electron microscopy (EM) investigations (e.g., Moon, 1972; Collins & McGown, 1974) have shown that clays are rarely observed in isolation and are found instead in multi-platelet particles or 'domains' (Bennett & Hulbert, 1986; Bennett *et al*., 1991).

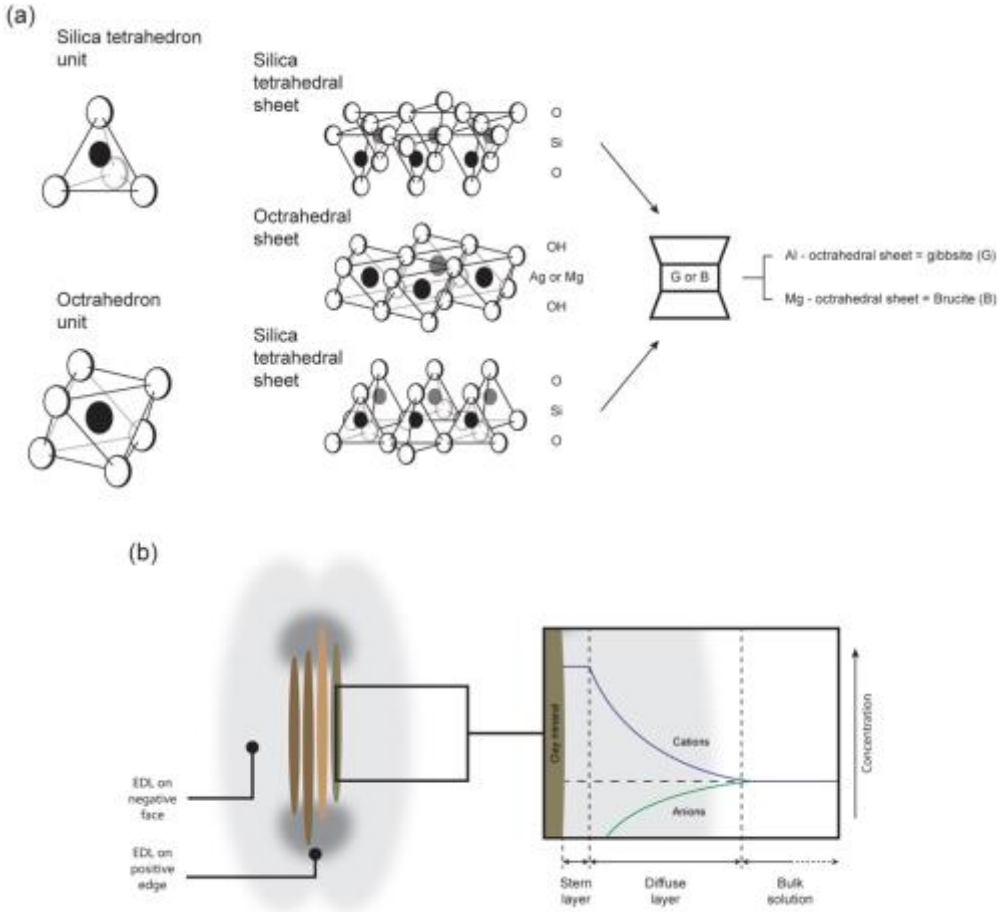

Figure 1.2. (a) Simplified representation of the atomic structure of clays which consist of sheets of silica tetrahedra and aluminum-hydroxide (gibbsite) or magnesium-hydroxide octahedra (brucite) (Winterwerp & van Kesteren, 2004). (b) Schematic showing the electrical double layer (EDL) which forms around charged particles (such as clays) in solution. The EDL is comprised of the electrical charges on the surface of the particle and ions in solution which are opposite in sign (Curry *et al*., 2009). In the example shown the particle is a negatively charged clay platelet that is surround by a diffuse 'cloud' of positively charged cations. Cation concentration is a function of distance, increasing as the distance from the surface of the clay mineral decreases. Immediately adjacent to the surface of the particle is the Stern Layer, which is composed of a specific number of tightly packed ions (Stern, 1924; Mitchell & Soga, 2005). The electro-chemical activity of a clay mineral is determined by its cation exchange capacity (CEC), i.e. the capacity of a clay to absorb cations to it surface, and the it particle size. Clay minerals that exhibit a high CEC (e.g., montmorillonite) will bond strongly as opposed to species such as kaolinite which have a lower CEC (Schindler *et al*., 2015).

Sources of organic matter within flocs can be those derived *ex situ* (allochthonous) from terrestrial environments and delivered to the aquatic environment from the catchment contained within soil aggregates and those generated internally (autochthonous). As a result, natural aquatic sediment often contains a wide variety of bioorganic structures and compounds. Flocs can contain both living organisms and those that have been incorporated

into detrital matter *post mortem* (Droppo, 2001). The range of material can vary significantly depending on the nature of the water body including living organisms (e.g., microbial cells and plankton) as well as non-living material (e.g., living and decayed plant matter, faecal pellets and humic substances) (Ransom *et al*., 1998; Droppo, 2001; Rogerson *et al*., 2003; Leppard & Droppo, 2005; Winterwerp & van Kesteren, 2004). Micro-organisms can include diatoms (siliceous skeleton of eukaryote cells in either freshwater or marine environments), radiolaria (found in marine environments and consisting mostly of silica), and foraminifera (calcium carbonate shell secreted by marine eukaryotes) (Ransom *et al*., 1999; Mitchell & Soga, 2005). An additional important organic component within flocs are the substances exuded by bacteria and certain higher organisms (e.g., diatoms) – extracellular polymeric substances (EPS) – the sticky nature of which [stickiness (α) typically >0.1 (Costerton *et al*., 1995; Engel, 2000; Burd & Jackson, 2009)] help stabilise floc structures through polymer bridging (Figure 1.3) (Droppo and Ongley, 1992; Buffle & Leppard, 1995a; Myklestad, 1995; Passow, 2002). EPS found within aquatic sediments are typically composed of proteins, carbohydrates, uronic acids and DNA (Bura *et al*., 1998), and range in size from 4 – 20 nm (Leppard, 1992b; Liss *et al*., 1996; Droppo, 2001). These polymeric fibrils often display a variety of morphotypes, ranging from discrete particles to gels (Chin *et al*., 1998; Leppard *et al*., 1997; Passow, 2002; Verdugo *et al*., 2004). The size of organic matter ranges from discernible particulate organic matter (POM) to colloidal (>0.1 μm) dissolved organic matter (DOM) (Grabowski *et al*., 2011).

1.2.2. Flocculation; Mechanisms of Aggregation, Break-up, Settling and Recycling

Suspended sediments in rivers and estuaries are usually derived from overland run-off and bed/bank erosion (Walling & Woodward, 2000; Droppo *et al*., 2005a; 2014). Regardless of origin, fine-grained SPM will flocculate and settle out over time, as turbulent flow promotes particle-to-particle collisions and flocs grow in size incorporating pore space (Winterwerp & van Kesteren, 2004; Furukawa *et al*., 2009) and decreasing in density (Klimpel & Hogg, 1986) such that flocculation efficiency (i.e. likelihood of collision) is partly controlled by both SPM concentrations and turbulence (Verney *et al*., 2009). Aggregation is then facilitated by two important mechanisms that depend upon the cohesive and adhesive properties characteristic of fine-grained particles (Hunter &Leonard, 1998; Liss, 2002; Grabowski *et al*., 2011). Cohesion, (e.g., electrochemical flocculation) describes the attraction of chemically similar particles (e.g., clay minerals), whilst adhesion (e.g., bioflocculation) reflects the

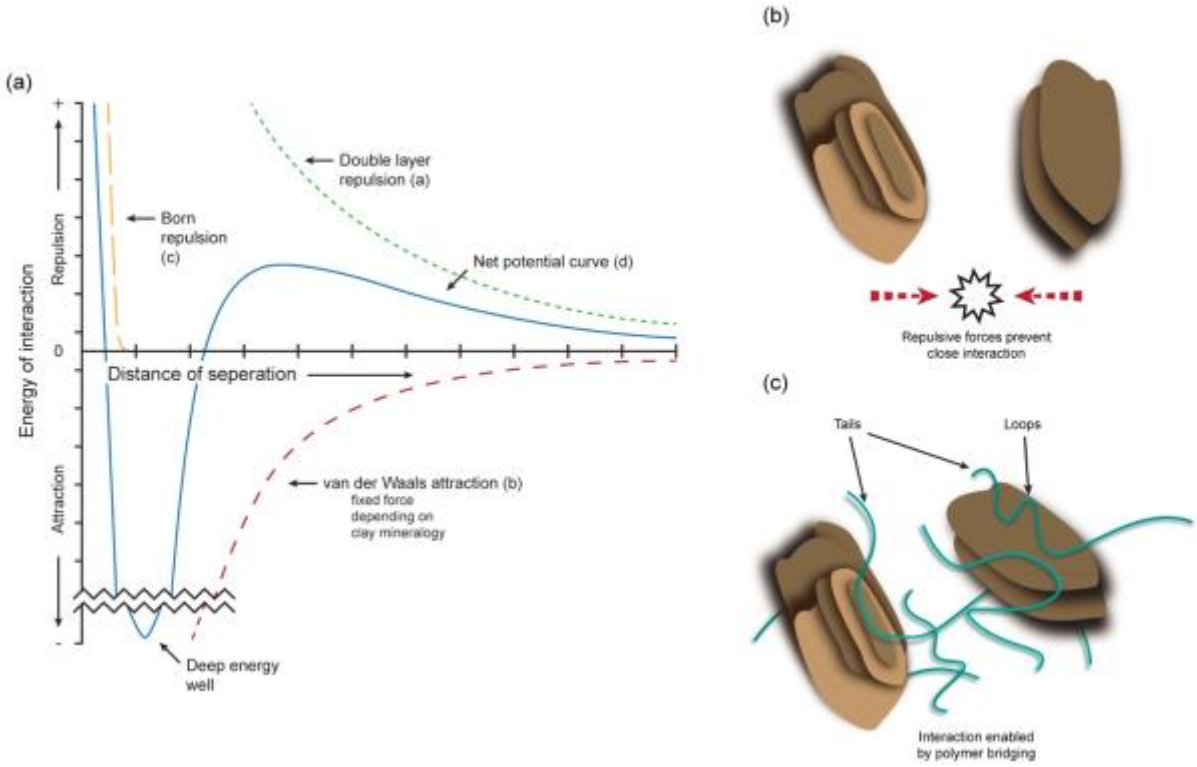

Figure 1.3. Particle interaction in suspension; (a) Potential energies of repulsion (yellow dotted line) and attraction (green dotted line) with distance for two (clay) particles. With decreasing distance, the electrical barrier between the particles increases and more energy is required to enable closer interaction (solid blue line) Valioulis (1983); (b) Close interaction between clay platelets is made difficult in suspensions where ionic concentration is low, i.e. freshwater systems, and the positive charge at the edge of mineral grains will be masked by their EDL (see Figure 1.2b). However, with increasing cation concentration the EDL will decrease in size, revealing the positively charged edges of clays and increasing the potential of interaction (Furukawa *et al*., 2009). (c) Neutrally charged extracellular polymers (EPS – see main text) may be readily absorbed to the surface of clay minerals as polymer-clay interactions are not influenced by repulsive forces. Polymer-clay will be much stronger than between clay minerals, due to the strength of bipolar forces relative to weaker Van der Waal's forces (Winterwerp & van Kesteren, 2004). EPS may adhere to the surface of clays in several locations, forming one or two 'tails' and 'loops' that can interact with other clay minerals in suspension (Hunter, 2001). In this way clays may be brought into contact despite the repulsive forces that exists between them, and in freshwater systems flocculation is primarily driven by polymer bridging (Droppo *et al*., 1997).

additional binding forces between chemically dissimilar particles, e.g., between organic EPS and minerogenic clay platelets (Paterson, 1997; Whitehouse *et al*., 2000; Righetti & Lucarelli, 2010; Droppo *et al*., 2014).

Electro-chemical flocculation is dependent upon surface charge, ionic strength of solution and the nature of the clays. Clay minerals exhibit characteristic EDL and are influenced by short range van der Waal's forces. Direct observations of clays in suspension

(e.g., Mehta & Partheniades, 1982) show that the number of successful collisions, i.e. those resulting in aggregation, varies depending on the electrolyte (salt) concentration of the solution. This is best explained by the Derjaguin-Landau-Verwey-Overbeek (DLVO) theory (Derjaguin & Landua, 1941; Verwey & Overbeek, 1948), which states that the interaction energy between two similarly charged particles is the sum of the attractive van der Waal's forces between the particle surfaces and electrostatic repulsion expressed by their EDL. In aquatic environments with a high concentration of electrolytes, e.g., estuaries, the net negative charge on the surface of clays will be neutralised allowing short range attractive van der Waals forces to dominate (Tsai *et al*., 1987; Droppo & Ongley, 1994). Consequently, if a particle is sufficiently close for van der Waals forces to be effective flocculation will occur. This is schematically depicted in Figure 1.3. Clay mineral composition is also important, for example flocs formed from a weakly bonding clay mineral such as kaolinite, will be smaller, with a very different structural composition to flocs composed of montmorillonite (Schindler *et al*., 2015).

A range of organisms in the aquatic environment, such as diatoms and bacteria, also secrete extracellular polymeric substances (Gehr & Henry., 1983; Geesey, 1982; Costerton *et al*., 1995; Myklestad, 1995; Frølund *et al*., 1996; Passow, 2002; Palomino *et al*., 2011), which help to bind and stabilise both settling and settled cohesive sediments (e.g., Filella *et al*., 1993; Paterson, 1997; Droppo, 2001). EPS can be classified as both colloidal or water soluble, and EDTA-extractable (e.g., Sanin & Vesilind, 1994; Lundkvist *et al*., 2007), and the EPS excreted by bacteria forms a capsule surrounding it ('bound' EPS), which both protects it and maintains a microhabitat (Droppo, 2001; Costerton *et al*., 1987), which in turn increases the cohesive strength of the floc as the EPS polymers form bridges that link particles within the floc (Droppo, 2001; Curry *et al*., 2002; McConnachie & Petticre, 2004; Wotton, 2005). However, flocs are dynamic, continually interacting with each other and the surrounding medium, and just as flocs aggregate, increasing turbulence and particle collisions can also lead to disaggregation (Van Leussen, 1988; Dyer, 1989; Droppo, 2001; Manning, 2004). Ultimately, flocs are inherently fragile, and their overall size and stability will attain an equilibrium with the surrounding environment that is dependent upon both the composition of the floc (e.g., nature of clay minerals, presence of organic matter and EPS) and the physico-chemical conditions in the water column (turbulence and ionic strength).

1.3. Characterisation of Flocculated Sediment

1.3.1. Current Techniques for Characterising Flocs

Settling velocity is the most important dynamic characteristic that determines SPM fate and transport (Mehta *et al*., 2014), and this is dependent on the size, shape, density and porosity of the flocs formed in suspension (Droppo, 2001; Williams *et al*., 2008 Maerza *et al*., 2011). Accurate quantification of these properties is therefore critical for parameterising sediment transport models, and in particular flocculation models. However, as a consequence of their complex structure, dynamically active nature and fragility, few standard methods with good reproducibility are available for characterising flocs (Liss, 2002).

1.3.2. Size and Shape

Measurements of flocs and their properties are usually derived from either photographic (e.g., Eisma *et al*., 1983; 1990; Stemmann *et al*., 2008) or videographic (e.g., Mikkelsen *et al*., 2005; Manning *et al*., 2010) methods, which allow flocs to be observed as 2D projections. These methods are favoured as they can be conducted *in situ* and thus do not expose flocs to destructive forces that may occur during sampling (Manning & Dyer, 2002a). Microscopic techniques [i.e. conventional optical microscopy (COM)] are also widely used and provide imagery with a higher resolution (Droppo & Ongley, 1992; Droppo *et al*., 1999; Liss *et al*., 2005). However, analysis via COM requires floc sampling, a process which may alter the natural stress environment of the floc and damage the natural floc structure (Li & Ganczarczyk, 1986; Droppo *et al*., 1996; 1997; Manning & Dyer, 2002). Additionally, flocs are highly unstable, and long storage times between sampling and observation may result in structural changes due to settling and self-weight consolidation (Droppo *et al*., 1996). COM studies must therefore stabilise flocs (ideally at the time of collection) to prevent floc breakage or storage-induced aggregation, and methods employed to achieve this are discussed in further detail in Section 2.2.2.

The assumption of equivalent spherical diameter (ESD) is widely used both because of its simplicity in extracting a 3D object from a 2D plane, and its application in Stokes' Law (Agrawal & Pottsmith, 2000; Soulsby *et al*., 2013). Yet flocs of equivalent diameter from different aquatic environments can have settling velocities that differ by an order of

magnitude (e.g., Verney *et al*., 2009), indicating that other characteristics must be important, and/or that current techniques for defining floc size are too rudimentary.

Floc populations are frequently classified into two groups: microflocs (diameter, <160 μm) and macroflocs (diameter, >160 μm) (Manning, 2001). Although this classification is largely arbitrary (Mikkelsen *et al*., 2005), the two populations do have distinct characteristics. In estuarine environments, microflocs have high particle concentration and are considered to be the building blocks for larger aggregates (Spencer *et al*., 2010). Macroflocs are less numerous but due to their large size have rapid settling velocities [1 – 15 mm • s^{-1} (Manning & Schoellhamer, 2013)] and hence are a significant contribution to downward mass flux, particularly within the turbidity maxima (Eisma, 1986; Dyer *et al*., 2002; Benson & French, 2007). Measuring the characteristics of both micro- and macrofloc populations is therefore frequently considered fundamental to understanding fine sediment transport dynamics (Manning, 2001), but this approach falls short of furthering an understanding of the mechanisms driving floc development and behaviour (Mikkelsen *et al*., 2005).

Particle shape affects settling velocity, with more elongate flocs increasing drag (Li & Ganczarczyk, 1987). Shape is commonly measured as simple 2D height to width ratios, whilst some sediment transport models use characteristic shapes based on fractal mathematics (Winterwerp, 1998; Lee *et al*., 2011; Williams *et al*., 2008).

1.3.3. Fractal Description

Fractal geometry is a commonly used to describe the properties of aqueous flocs in predictive models (e.g., Li & Ganczarczyk, 1989; Logan & Wilkinson, 1991; Hill, 1996; Winterwerp, 1998; Manning *et al*., 2010), and assumes that floc structure is independent of scale (Kranenburg, 1994; Winterwerp & van Kesteren, 2004; Jarvis *et al*., 2005), i.e. that flocs are self-similar entities. This concept was first hypothesised by Krone (1962), who later developed this theory into an order of aggregation model (Krone, 1963; 1978; 1986; Van Leussen, 1988) (Figure 1.4). The fractal dimension of an object describes its space-filling capacity, and ranges from 1 to 3. The greater the fractal dimension, the more uniform and compact a floc will be. Free-settling tests (e.g., Tambo & Watanabe, 1979; Li & Ganczarczyk, 1989; Kranenburg, 1994; Johnson *et al*., 1996; Tang *et al*., 2002), light scattering (e.g., Axford & Herrington, 1994; Jung *et al*., 1995; Bushell *et al*., 2002; Wu *et al*., 2002), and 2D image analysis (e.g., Chen & Eisma, 1995; Cousin & Ganczarczyk, 1998;

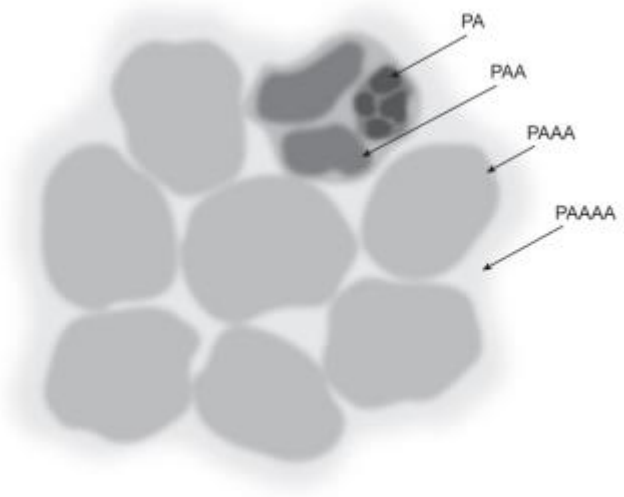

Figure 1.4. Conceptual model descripting the (fractal) organisation of flocs first proposed by Krone (1962); The smallest units are particle aggregates (PA) which consist of primary particles. These all exhibit the same porosities and are bound together to form larger particle aggregate aggregates (PAA). Particle aggregate aggregate are then organised into larger particle aggregate aggregate aggregates (PAAA) and so on. Adapted from Krone (1986).

Chakraborti *et al*., 2003) have all been employed to probe floc fractal dimension; however, measurements are limited by the scale of observation and these techniques are inadequate where floc composition is complex (Jarvis *et al*., 2005; Khelifa & Hill, 2006). Consequently, these approaches are not fit for purpose where flocs composition is complex (e.g., contains both inorganic and organic material) and/or it is a mud-sand mixture (i.e. cohesive and non-cohesive) (Paterson & Hagerthey, 2001; van Ledden, 2002; Manning *et al*., 2010; Spencer *et al*., 2010; Manning *et al*., 2013). As a consequence, the use of a single fractal dimension has been deemed an inadequate descriptor of floc structure, and several studies have suggested an amendment to floc fractal theory whereby the fractal dimension varies with floc size (e.g., Dyer & Manning, 1999; Chu & Lee, 2004; Khelifa & Hill, 2006).

1.3.4. Density and Porosity

Floc density and porosity are 3D characteristics that have a significant impact on settling velocity and it is the low density, highly porous [porosity, >95% (Manning *et al*., 2010)] macroflocs [diameter, >160 μm (Manning, 2001)] that have the most influence on mass settling flux due to the reduced drag caused by their high porosity (Mehta & Lott, 1987; Liss *et al*., 2005). Floc density and porosity cannot currently be measured at all, and transport model parameters are estimated from Stokes' Law or modified Stokes' Law (ten Brinke,

1993; Manning & Dyer, 2002b), based on assumptions of spherical shape (e.g., Soulsby *et al*., 2013) and fractal behaviour (Winterwerp, 1998). Zahid & Ganczarczyk (1990) note that density and porosity measurements made in this way are at best approximations, and that a number of uncertainties remain that make the validity of this approach questionable. Consequently, density and porosity is often omitted from models with flocs treated as impermeable entities (e.g., Zahid & Ganczarczyk, 1990; Stolzenbach & Elimelich, 1994; Gregory, 1978). In addition, these are estimated as gross floc characteristics with little understanding of how density or porosity may be distributed or the mechanics of flow through these porous macroflocs. Droppo *et al*. (2005a) showed that flocs in the water column are often hybrid structures consisting of different forms of agglomerated units (e.g., denser soil aggregates and more porous flocculated material).

1.3.5. Floc Structure

Floc structure can be directly observed via optical or EM imaging techniques (Leppard *et al*., 1992a; 1992b; Liss *et al*., 1996). For the latter of these methods fragile flocs must first be rendered vacuum stable prior to analysis (Buffle & Leppard, 1995b). Several techniques for stabilising aqueous floc samples have been developed, but by far the most successful has been outlined by Liss *et al*. (1996). This protocol for floc stabilisation is discussed at length in Section 2.2.2.

Figure 1.5 shows the imaging techniques that are most commonly employed by floc studies and the length-scales over which they operate. COM, described previously in Section 1.3.2, is primarily used as a means of analysing the external millimetre-scale (or gross scale) properties of flocs (e.g., size and shape) (Droppo & Ongley, 1992; Liss, 2002; Liss *et al*., 1996; 2005), which in conjunction with settling velocity measurements can be used to infer floc structure based on fractal theory. Further inferences regarding internal floc structure can, however, be drawn based on the degree of light penetration (Liss *et al*., 1996; Droppo, 2004). It is suggested that for more densely packed regions within flocs light penetration is impeded (Droppo, 2004), and Droppo *et al*. (2005a) used this approach as a means of differentiating between material within 'hybrid' flocs that contained material from different sources (e.g., denser water stable soil aggregates and more porous material flocculated in suspension). Due to the limited resolution and 2-dimensionality of COM this approach may be misleading, and Liss *et al*. (1996) notes that extreme caution should be taken when interpreting datasets in

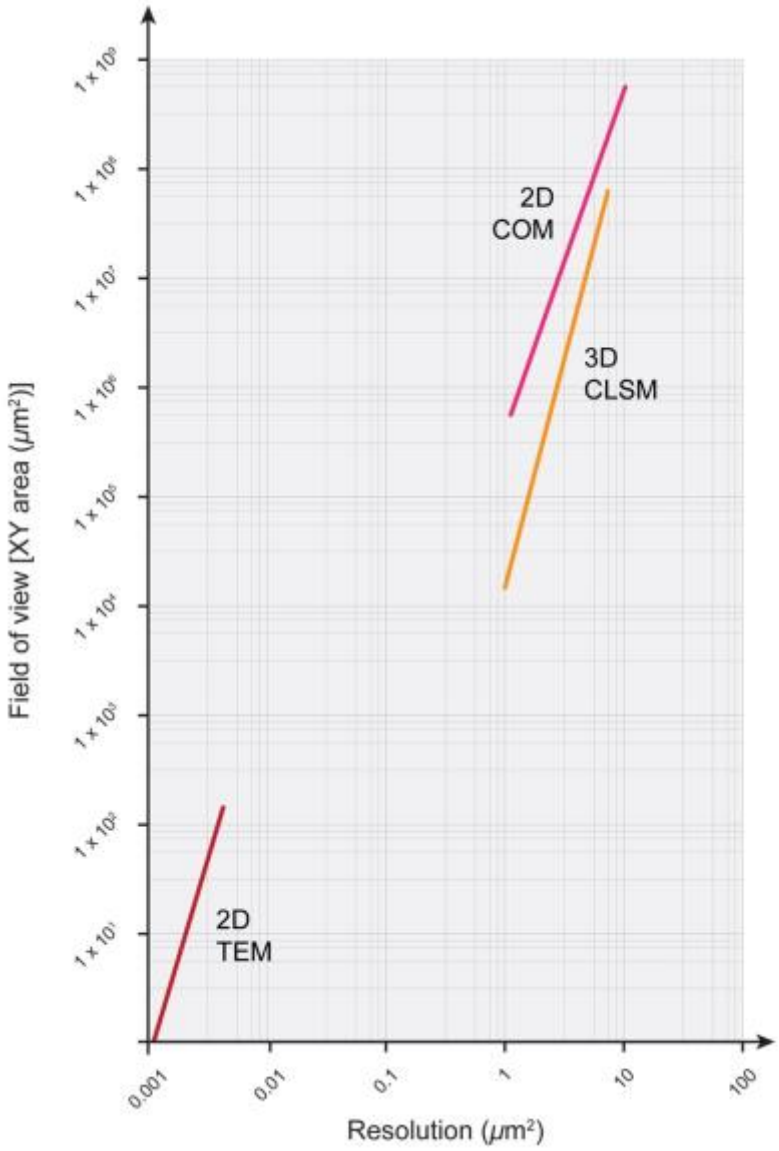

Figure 1.5. Length-scales over which the imaging techniques commonly used to characterise floc properties (e.g., size, shape and structure) operate, with corresponding typical cross-section (XY) and resolution achieved by each technique.

this way, as errors in interpretation may be incurred by the position of the floc relative to the light source.

Measurements of the internal 3D distribution of flocculated material can be made using confocal laser scanning microscopy (CLSM) (Thill *et al*., 1999; Liss *et al*., 2005). This is achieved by combining CLSM with two-photon laser scanning microscopy (2P LSM), which when applied to floc samples the organic components of which have been fluorescently labelled via staining, enables the spatial distribution of bacterial cells and polymeric material within the flocs to be examined non-destructively (Decho *et al*., 1999; Lawrence *et al*., 2003; Liss *et al*., 2005; Mahendran *et al*., 2012). CLSM can achieve a higher image resolution

compared to COM due to reduced image blurring caused by light scattering (Caldwell *et al*., 1992; Decho *et al*., 1999), but cannot resolve floc constituents in the nanometre range.

Investigation of the nanometre-scale properties of aqueous flocs requires TEM, which when used in conjunction with energy dispersive spectroscopy (EDS) enables both internal structure and composition of flocs to be described (e.g., Leppard *et al*., 1992a; Zartarian *et al*., 1994; Jorand *et al*., 1995; Rogerson *et al*., 2003; Kim *et al*., 2012). Imaging is conducted on ultrathin-sections (thickness, 50 – 100 nm) obtained from resin embedded floc samples, and has a field of view limited of 10's of μm (Goodhew *et al*., 2000; Williams & Carter, 2013). At this length-scale structural elements such as fibrillar EPS can be recognised, and several studies have observed EPS linking inorganic clay particles (e.g., Liss *et al*., 1996; Leppard *et al*., 1996; Ransom *et al*., 1997; Snidaro *et al*., 1997) confirming their structural role within flocculated sediments (Droppo, 2001). Elemental analysis of flocculated particles via EDS also provides information regarding the compartmentalisation/association of aquatic pollutants and contaminants (e.g., Fortin *et al*., 1993; Leppard *et al*., 1998; Droppo & Amos, 2001; Leppard *et al*., 2003; Kim *et al*., 2005). Observations of the distribution of EPS within flocs has been used to assess floc permeability, which is difficult to describe using COM. Indeed, Liss *et al*. (1996) demonstrated that the pores of floc samples that appeared to be devoid of structure in COM imagery were found to be filled with polymeric material when observed using high-resolution TEM. Such insights are critical for understanding mechanics of fluid flow through the internal structure of flocculated sediment (Zahid & Ganczarczyk, 1990; Droppo, 2001), and determining hydrodynamic resistance which directly influences floc settling dynamics (Liss *et al*., 2005).

Similar to COM, the 2-dimensionality of TEM prevents the accurate reconstruction of 3D geometries (Holzer *et al*., 2014). This has prevented TEM data from being used as a means of validating the assumption that flocs are fractal entities. It is possible to extract 3D structural information using TEM by aligning images taken from successive thin-sections, but this is labour intensive and time-consuming (Bushby *et al*., 2011). In addition, the poor *z* resolution, which will be equivalent to the thickness of the thin-sections, and the likelihood of sectioning artefacts [e.g., tears and wholesale compression (Williams & Carter, 2013; Goodhew *et al*., 2000)] render the benefits of this technique small compared to the input effort, and this approach has not been applied to flocs. Zartarian *et al*. (1997) did conduct a similar imaging programme using COM which involved taking observations of sequential thin-sections, and in so doing succeeded in creating a 3D model of floc structure based on

interpolation between the 7 μm-thick slices. However, they acknowledged the above difficulties and the approach has not been since applied elsewhere.

More recently, studies have adopted an imaging methodology that combines TEM, CLSM and COM that enables the acquisition of structural information from individual floc samples at the nano- and millimetre-scale respectively (Leppard, 1992a; Liss *et al.*, 1996; Leppard *et al.*, 1996; Heissenberger *et al.*, 1996b; Lawrence *et al.*, 2003). This technique allows multi-scale and multi-modal datasets obtained from a single sample of interest to be correlated, an approach which has proven insightful, even admitting the limitations of these techniques for investigating flocs (Mavrocordatos *et al.*, 2007).

1.4. Correlative Tomography

1.4.1. Applications in Materials Science and the Life Sciences

As described in the previous section, studies investigating the multi-scale characteristics of flocculated sediment have traditionally relied on correlative microscopy, a strategy involving the spatial registration of information collected at different scales using several imaging modalities (Leppard, 1992a; Liss *et al.*, 1996; Mavrocordatos *et al.*, 2007). By combining COM and TEM, floc properties at the millimetre and nanometre scales respectively can be visualised. However, there remains a critical spatial gap between the resolutions of the two primary techniques used (COM and TEM) that prevents a complete understanding of how structures at different scales are related (see Figure 1.5). Additionally, since it is impossible to extract accurate 3D geometries from 2D projections (Holzer *et al.*, 2004; Münch *et al.*, 2006; Uchic *et al.*, 2007), the information provided by COM and TEM is potentially misleading. CLSM has been deployed alongside TEM and COM and does provide 3D information (e.g., Lawrence *et al.*, 2003); however, it does not overlap with TEM and is usually applied in an uncorrelated manner.

Over the last decade the use of 3D imaging techniques, specifically micro-computed tomography (3D μCT) and focused ion beam nanotomography (FIB-nt), has gained in popularity across multiple disciplines. 3D μCT, which is based on the principle of X-ray attenuation by matter (Duliu, 1999; Mees *et al.*, 2003; Davis & Elliott, 2006), has proven itself to be a powerful characterisation tool and has been applied extensively in the environmental sciences (e.g., Orsi *et al.*, 1994; Denison *et al.*, 1997; Van Geet *et al.*, 2000;

Selomulya *et al*., 2005; Carlson, 2006; Kettridge & Binley, 2008; Long *et al*., 2009; Dewanckele *et al*., 2012; Bendle *et al*., 2015). The maximum spatial resolution of X-ray μCT varies between instruments, but typically ranges between 5 – 10 μm^3 (Cnudde *et al*., 2009; Cnudde & Boone, 2013). In comparison, FIB-nt has a resolution approaching that of TEM (up to 10 nm^3) (Holzer *et al*., 2004; Uchic *et al*., 2007; Bushby *et al*., 2011; Cantoni & Holzer, 2014), and an upper resolution limit that approaches that of μCT (Möbus & Inkson, 2007). This gap was closed by Desbois *et al*. (2013) and Hemes *et al*., 2015) using broad ion beam (BIB)-SEM, which enables large sample areas (mm^2 to cm^2) to be analysed with a slice thickness of 100's of nanometres via BIB-tomography (Desbois *et al*. 2009). FIB-nt makes use of FIB scanning electron microscopes (FIB-SEM), which incorporate FIB for *in situ* milling and SEM for high-resolution imaging (Volkert & Minor, 2007; Schiffbauer & Xiao, 2009; Peddie & Collinson, 2014). Most significantly, both μCT and FIB-nt provide accurate 3D data which is suitable for quantitative analysis, the results of which can be used to parameterise computational models (Holzer *et al*., 2004; Ketcham, 2005; Holzer *et al*., 2007; Patterson *et al*., 2012; Maire & Withers, 2014).

In materials and the life sciences 'correlative tomography', a 3D expression of traditional 2D correlative microscopy (Burnett *et al*., 2014), has exploited the development of these and other 3D imaging techniques (e.g., Armer *et al*., 2009; Caplan *et al*., 2011; Murphy *et al*., 2011; Lucas *et al*., 2012; Cao *et al*., 2014; Burnett *et al*., 2014; Hemes *et al*., 2015). Whilst conceptually similar, the task of aligning multiple datasets in 3D space is somewhat more challenging than in 2D, as the region or regions of interest (RoI) may lie beneath the sample surface (Caplan *et al*., 2011; Burnett *et al*., 2014). However, several solutions to this technical problem have been proposed [e.g., the use of fiducial landmarks implanted within a sample (Maes *et al*., 1997; Rohr *et al*., 2001; Caplan *et al*., 2011)], which have allowed datasets to be registered with a high degree of accuracy (Braet & Geerts, 2009; Peddie & Collinson, 2014). For example, Handschuh *et al*. (2013) was able to align datasets collected at several observational length scales using μCT, COM and TEM with only minor geometric deviations observed in peripheral regions of the specimen.

1.5. Concepts Addressed in this Thesis

1.5.1. Research Aims and Objectives

The overall scientific aim of this thesis is to demonstrate for the first time that correlative tomography can be used to explore the 3-dimensional properties of aqueous flocs. Adapting the correlative workflow to the investigation of flocculated sediment involved three subsidiary objectives:

- To demonstrate that fragile floc samples can be successfully prepared for correlative tomography;
- To quantitatively describe and correlate floc properties at different length-scales;
- To propose a conceptual model for floc structural hierarchy.

Chapter Two: Method Development

2.1. Introduction

This chapter describes the methods and materials used in the development of the correlative workflow applied in this study to the multi-scale imaging of aqueous flocs. The correlative workflow is initially outlined in Section 2.1.1. Following this a description is given of the three stages of floc acquisition (§ 2.2), data collection and reconstruction (§ 2.3) and the

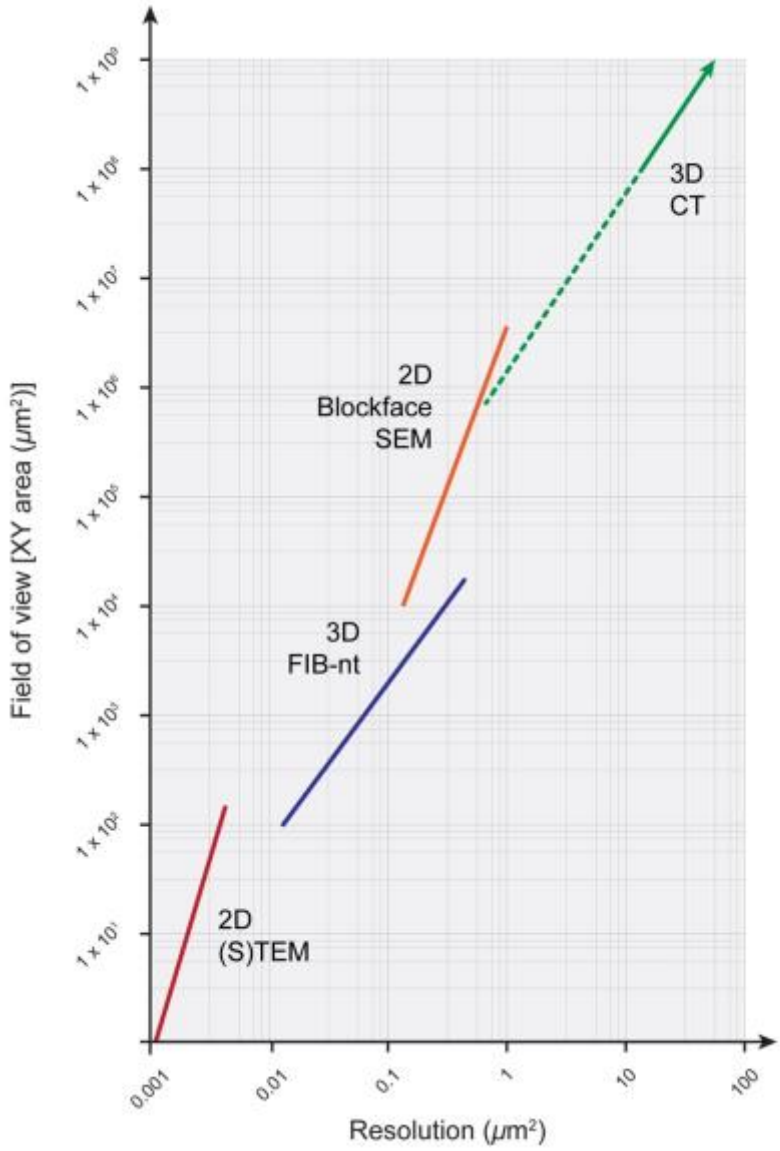

Figure 2.1. Length-scales over which the imaging tehcniques employed within correlative workflow operate, with corresponding typical cross-section (XY) and resolution ahcievable by each technique. Note that the solid green line represents the limits of 3D μCT whilst the dotted line shows the limit of nano-CT.

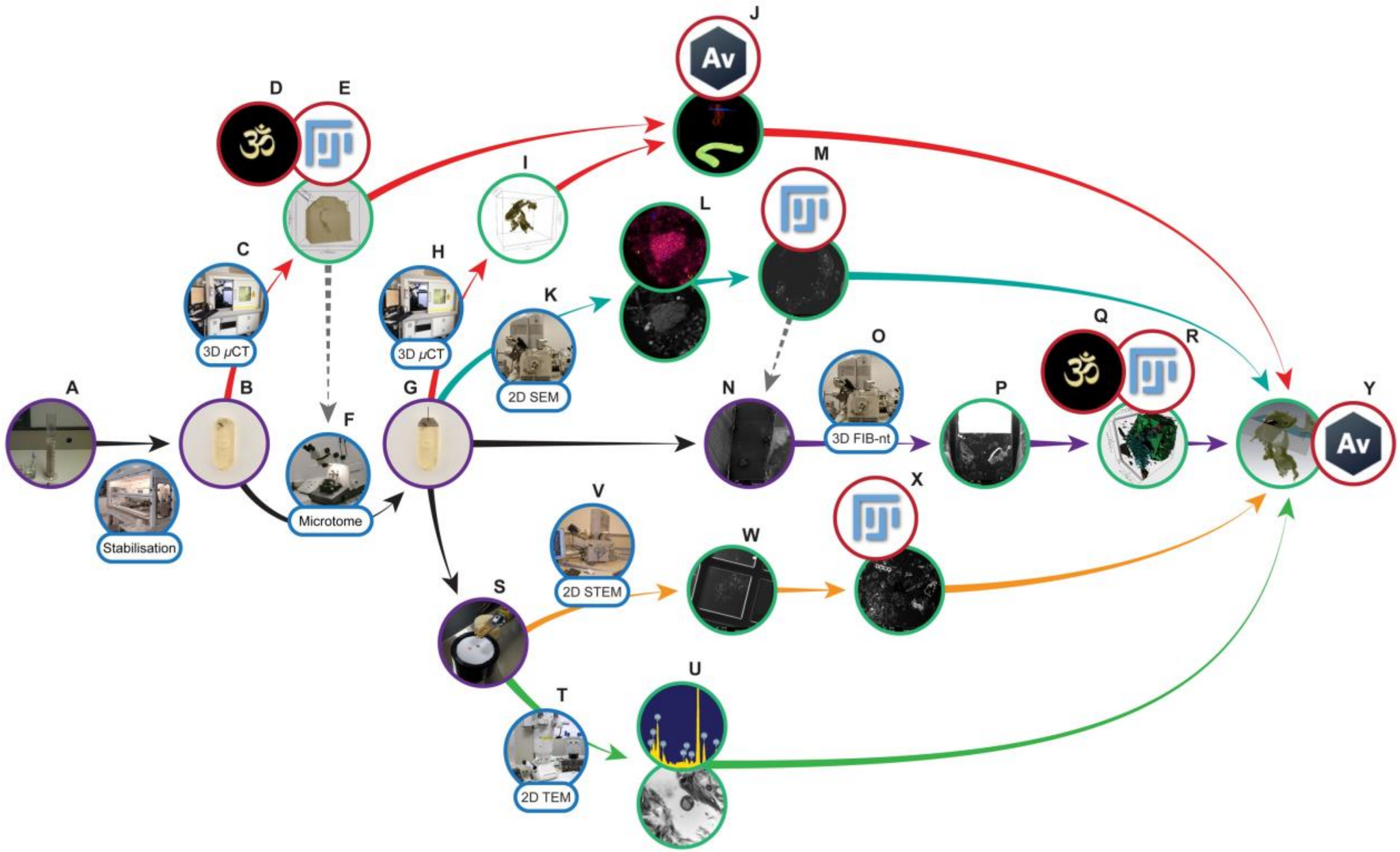

Figure 2.2. Correlative workflow applied to the multi-scale imaging of aqueous flocs. The coloured arrows indicate the different data collection pathways: black arrows indicate the path of the sample, red arrows indicate steps taken to acquire and process 3D μCT datasets; turquoise arrows 2D SEM block-face images and SEM-EDS maps; purple 3D FIB-nt data volumes; orange 2D STEM imagery, and green arrows 2D TEM micrographs and TEM-EDS spectra. **A**, Flocculation of natural estuarine sediment, sampling and stabilisation; **B**, Resin embedded floc sample; **C**, 3D μCT; **D**, Rendering of μCT dataset; **E**, Analysis of μCT data; **F**, μCT used to locate RoI during ultramicrotome (represented by dotted grey arrow); **G**, Sectioned sample blocks; **H**, 3D μCT scans of section block; **I**, Drishti rendered CT data; **J**, visualisation of data sets; **K**, 2D SEM; **L**, SEM imagery (to create montages) and SEM-EDS; **M**, Characterised working surface (high-resolution SEM montages) (represented by dotted grey arrow); **N**, SEM montages used to identify RoI for FIB-nt; **O**, 3D FIB-nt; **P**, FIB-nt image stack; **Q**, Rendering of FIB-nt datasets with Drishti; **R**, Analysis of FIB-nt datasets using Fiji/ImageJ; **S**, Ultrathin-sections collected during ultramicrotomy; **T**, 2D TEM; **U**, acquisition of TEM imagery and TEM-EDS spectra; **V**, 2D STEM; **W**, STEM imagery; **X**, Stitching of STEM imagery to create STEM montages; **Y**, Co-visualisation of correlative datasets.

processing and analysis of the multi-modal, multi-scale datasets (§ 3.3).

2.1.1. Correlative Workflow

This study further develops the strategy of correlative tomography (e.g., Handschuh *et al.*, 2013; Burnett *et al.*, 2014), threading together 3D μCT and FIB-nt with 2D STEM and TEM to enable fragile flocs to be characterised, for the first time, from the millimetre to nanometre-scale. Figure 2.1 shows the length-scales over which the individual imaging techniques operate, whilst the correlative workflow is presented in Figure 2.2.

Stabilised floc samples were initially observed at the millimetre-scale using non-destructive μCT (described in § 2.3.3). At this scale, individual components of the flocs (e.g., bacteria and clay minerals) were beyond the resolution limit of the μCT datasets. Despite this, the floc samples exhibited internal variations in X-ray attenuation values (i.e. grey-scale, see § 3.4). This enabled region(s) with the flocs to be targeted for further analysis at higher-magnification, an approach known as 'scout and zoom' (Zhang *et al.*, 2013; Burnett *et al.*, 2014). Once identified, flocs were sectioned to expose the RoI in a working surface (process described in § 2.2.2). Thin-sections cut from the surface of the blocks were retained for nanometre structural and compositional analysis via TEM and STEM and TEM-EDS (described in § 2.3.1). The acquisition of 100's of high-resolution SEM images from the sectioned block-face of the samples (2D block-face SEM) was required to characterise the working surface and pin-point RoI. 2D block-face SEM also bridged the gap between millimetre μCT scans and micrometre FIB-nt datasets. FIB-nt datasets were collected from the samples (described in § 2.3.2), and provided an understanding of the 3D arrangement of the constituents of the flocs that was impossible using μCT.

2.2. Stage 1: Floc Acquisition and Preparation

2.2.1. Acquisition of Flocs

To produce floc samples fine-grained cohesive sediment collected from the Thames Estuary, SE England (see Figure AI.1 in Appendix I) was added to an artificial seawater solution (Sigma® sea salts 34 g L^{-1}) and gently agitated using a magnetic stirrer. This suspension had a SPM concentration of ~500 mg L^{-1}, within the typical range of values observed within natural estuaries (e.g., Manning *et al.*, 2010). Individual flocs were then sampled using a wide-

mouthed pipette to avoid floc breakage (Gibbs & Konwar, 1982; Droppo *et al*., 1996). Subsequently, the sampled flocs were transferred directly to 1.5 mL vials for stabilisation.

2.2.2. Stabilisation Procedure

Due to their fragile and hydrated nature flocs cannot be described in their native state but must be rendered vacuum stable prior to their investigation (Leppard, 1992a; Buffle & Leppard, 1995b), and electron dense contrast agents need to be introduced to reveal organic materials in electron microscopy and X-ray tomography. Whilst the primary aim of stabilisation is to maintain the structural integrity of flocculated material during preparation and subsequent analysis, laboratory manipulation itself often introduces some preservation artefacts (Leppard, 1992a; Leppard *et al*., 1996). To mitigate against artefacts associated with individual stabilisation techniques, studies investigating the internal structure of aqueous flocs have adopted a multi-method protocol for floc stabilisation (Liss *et al*., 1996; Leppard *et al*., 1996). This approach, which is outlined in Figure 2.3, combines four treatment procedures (pathways) and applies them in a comparative manner to allow artefacts inherent to each to be identified and assessed.

Stabilisation pathways 1 and 2 utilise a hydrophobic epoxy resin as an embedding medium [Spurr resin (Spurr, 1969)], and thus samples must be dehydrated in a solvent series (e.g., ethanol) prior to resin infiltration. This procedure can be traumatic, particularly for organic material (e.g., bacteria) which contain significant quantities of water. An intermediate step known as 'fixation' is therefore required to prevent the collapse of delicate organic structures (Hayat, 1981; Smart & Tovey, 1982; Baerwald *et al*., 1991; Bozzola & Russell, 1999). Where organics play an important structural role, such as in marine flocs, fixation is critical. Inevitably, however, some physical modifications to the sub-cellular structure of the target specimen will occur, as fixatives essentially change the original chemical composition of the organic material they are intended to preserve (Glauert, 1987). Additionally, there is no one fixative that provides perfect results for all organics. This is significant since flocs are compositionally diverse and often contain a variety of organic material with different characteristics. By employing more than one fixative solution effective for different components (double fixing), these issues can be overcome. The use of glutaraldehyde ($C_5H_8O_2$) as a primary fixative followed by osmium tetroxide (OsO_4) as a secondary fixative

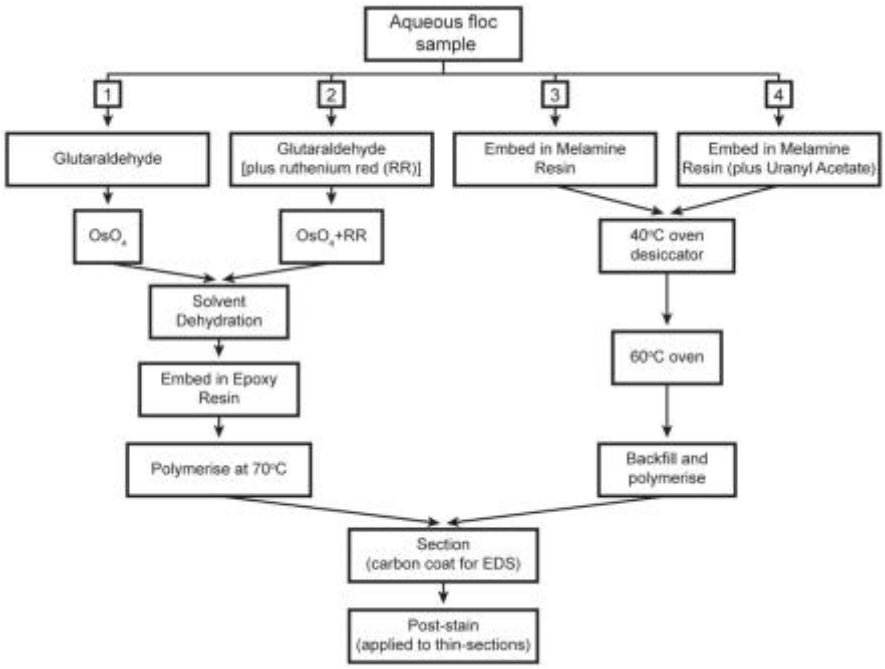

Figure 2.3. Multi-preparatory method used to stabilise aqueous flocs for ultrastructural analysis as described by Liss *et al*. (1996). Pathways 1 and 2 are designed to prepare flocs for embedding in a hydrophobic epoxy resin, and thus require flocs to be dehydrated in a solvent series (e.g., ethanol or methanol) prior to resin infiltration. Glutaraldehyde ($C_5H_8O_2$) and osmium tetroxide (OsO_4) are employed as primary and secondary fixing agents respectively, and are used to fix fragile organic structures prior to solvent dehydration. Pathways 3 and 4 utilise a hydrophilic melamine resin as an embedding medium, which negates the need for fixation and dehydration as in 1 and 2. In Pathway 2 glutaraldehyde and osmium tetroxide are combined with ruthenium red ($H_{42}N_{14}O_2Ru_3$ • 6Cl) which reduces the extraction of fibrillar EPS but degrades the image quality, resulting in 'grainy' imagery (Leppard *et al*., 1996). The addition of uranyl acetate [$UO_2(CH_3COO)_2$ • 2 H_2O] as an en bloc stain in Pathway 4 helps to improve low contrast problems when using a melamine resin (Mavrocordatos *et al*., 1994; Liss *et al*., 1996); however, some structures remain unstained and thin sections taken for TEM must be counter stained to provide differential contrast between organic structures (Leppard *et al*., 1996; Webb *et al*., 2000). Note that this workflow was designed for preparing ultrathin-sections for TEM and that last two steps in the procedure are required specifically for TEM. Adapted from Liss *et al*. (1996).

has been found to provide excellent results for a wide variety of specimens (Sabatini *et al*., 1963; Glauert, 1987).

Inorganic particles which strongly absorb electrons are much easier to see in EM than weakly electron-dense components (e.g., organic macromolecules). Chemical stains (often metal-based), which bind to the object of interest, are therefore required to increase the electron density of organic material (Wilkinson *et al*., 1995; Buffle & Leppard, 1995b; Mavrocordatos *et al*., 2007). In pathways 1 and 2 several stains can be applied prior to resin

embedding, allowing different organic structures to be preferentially stained throughout the sample (in 3D).

In comparison, stabilisation pathways 3 and 4 advocate the use of a hydrophilic melamine resin [Nanoplast resin, Frösch & Westphal (1989)] in which to embed fragile floc samples. The use of resin miscible with water means that fixation and solvent dehydration can be omitted from the workflow. Deformation of the sample is considered to be minimised due to the retention of pore water and thus matrix surface tension within the sample (Liss *et al*., 1996; Leppard *et al*., 1996). Furthermore, cross-linkages between EPS within the floc are made prior to water loss, allowing accurate measurements to be potentially made concerning the characteristics of colloidal EPS (Frösch & Westphal, 1989; Liss *et al*., 1996; Webb *et al*., 2000). However, this pathway has not been developed for through block staining necessary for FIB-nt and the suitability of melamine resins for FIB milling has not been established.

Here, a preparation protocol for through block staining developed by Deerinck *et al*. (2010) was employed to render floc samples vacuum stable. Whilst designed for the stabilisation and 3D EM of biological tissue, the protocol is similar to procedures described by Liss *et al*. (1996) and Leppard *et al*. (1997) (Pathway 1; Figure 2.3). The reader is referred to Appendix II were a detailed description of the various steps taken during the stabilisation procedure is presented (see Figure AII.1). To minimise the effect of storage artefacts [i.e. morphological changes caused by aggregation and disaggregation (Droppo *et al*., 1996)], floc samples were immediately stabilised following their acquisition. Flocs were first fixed in a buffered solution of 0.15 M sodium cacodylate [$Na(CH_3)_2AsO_2 \bullet 3\ H_2O$] (pH 7.4) containing 2.5% glutaraldehyde and 2% formaldehyde (CH_2O) with 2mM calcium chloride before being embedded in Durcupan, a hydrophobic resin. Other epoxy resins (e.g., Epon and Spurr) have been used for FIB-nt (e.g., Denk & Horstmann, 2004; Cardona *et al*., 2010; Bhawana *et al*., 2014), however, Durcupan, which provides good contrast and is slightly softer, has been shown to have favourable cutting properties for FIB (Bushby *et al*., 2011). Intermediate steps were implemented to improve contrast and remove pore water, achieved by the addition of heavy metal stains (uranyl acetate, thiocarbohydrazide and lead aspartate] and washing samples in an ethanol series (20%, 50%, 70%, 90%, 100% and 100%) followed by anhydrous acetone. This procedure renders the organic material electron dense throughout the resin block and is suitable for both EM and μCT.

Following embedding, scans of the stabilised samples were conducted using X-ray μCT (see § 2.3.3). The 3D millimetre-scale datasets from these initial μCT scans were subsequently reconstructed using the imaging software Drishti (see § 2.4), and visually inspected to identify a suitable region within the floc sample to create a working surface. Preference was given to regions of the flocs that exhibited differing X-ray attenuation properties (i.e. contained both high and low grey-scale values, see § 3.4). Once a location was identified, resin-embedded flocs were trimmed using a diamond knife mounted in an ultramicrotome (Leica UCT ultramicrotome). Ultrathin-sections (thickness, 70 – 100 nm) cut directly adjacent to the working surface were retained for nanometre investigation (see § 2.3.1). Trimmed samples were then mounted on aluminium SEM stubs using carbon cement, and carbon coated in a vacuum evaporation unit (Balzers CED030). Coating the samples in conductive carbon ensured imaging artefacts resulting from material charging, due to exposure to the electron and ion beam, were kept to a minimum (Bushby *et al*., 2011), while having minimum influence on BSE imaging and X-ray spectroscopy.

2.3. Stage 2: Acquisition and Reconstruction of Correlative Datasets

2.3.1. Nanometre Datasets; 2D TEM-EDS and STEM

Thin-sections were collected from the top of the sample block by ultramicrotomy. The final sections, adjacent to the block-face, were removed and mounted on formvar-covered copper grids (Gilder Grids) and carbon coated for stabilisation during EDS analysis. The sections were then transferred to a JEOL 1200 EX-II TEMSCAN STEM (Peabody, Massachusetts, USA) and examined in transmission mode (bright-field TEM) at an accelerating voltage of 80 kV. The elemental composition of constituents identified within the thin-sections was analysed using the same STEM equipped with a Princeton Gamma-Tech Si(Li) X-ray detector (Princeton, New Jersey, USA) in conjunction with IMIX image processing software, which provided spectra for higher weight atomic elements (z >10). Dark-field STEM imagery was obtained from the same thin-sections using an FEI Inspect-F™ field emission gun (FEG) SEM (Hillsboro, Oregon, USA) operating at 30 kV and fitted with a split detector STEM stage.

2.3.2. Micrometre Datasets; 2D SEM-EDS and 3D FIB-nt

EDS elemental mapping of selected RoI was performed directly on the block-face of the samples using an FEI Inspect-F™ FEG SEM equipped with an Oxford Instruments (Oxford, UK) INCA x-act™ energy dispersive X-ray spectrometer. Analysis was conducted at an accelerating voltage of 10 kV over a counting period (range, 10 – 30 mins) selected to minimise sample damage and varied between RoI.

SEM imagery and FIB-nt datasets were obtained using an FEI Quanta™ 3D FEG FIB-SEM (Hillsboro, Oregon, USA). For FIB-nt block preparation and data collection, samples were inserted into the stage of the Quanta and raised to the eucentric height (10 mm) where the electron and (gallium) ion beams converge (Figure 2.4). With both beams focused on a coincident point on the sample surface, the stage was tilted to an angle of 52° to bring the trimmed block-face into a position perpendicular to the ion beam. This enabled precision milling and imaging of the exposed subsurface. Prior to serial sectioning a smooth, dense, protective platinum coating with a consistent thickness of ~1 μm, was deposited over the RoI to minimise milling fluctuations that can result in 'curtaining artefacts' (morphological defects on the milled cross-section, Cairney *et al*., 2000; Orloff *et al*., 2003; Uchic *et al*., 2007; Münch *et al*., 2009), and also to prevent 'pitting' (localised deformation of the sample, Volkert & Minor, 2007; Bushby *et al*., 2011; Bassim *et al*., 2012) caused by stray ions. Such precautions help to ensure an atomically smooth cross-section for FIB-nt.

The target site was then isolated from the surrounding material by milling trenches on three sides of its perimeter to create a suitably sized cube (Figure 2.4c). Optimal imaging and milling parameters were determined through experimentation on a test dataset (labelled S3, see § 3.3.3) before being applied to the sample blocks (S4 and S5). Tests revealed an accelerating voltage of 30 kV and a current of 0.5 – 5 nA for the ion beam to be optimal for milling. Prolonged exposure of the sample to beam currents greater than 5 nA resulted in charging of the sample and eventual damage. Once a cube was prepared the front trench was enlarged to reveal a cross-section for imaging (Figure 2.4c). Trenches flanking the cube acted as repositories into which sputtered material could collect to help minimise imaging artefacts resulting from the re-deposition of milled material (e.g., Holzer *et al*., 2004; Bushby *et al*., 2011). Serial sectioning was achieved using auto Slice & View™ software (FEI, Dufek, 2005) and an image sequence acquired using either the BSE or SE signal. The accuracy of this procedure is reliant on the stability of the FIB during image collection and its ability to

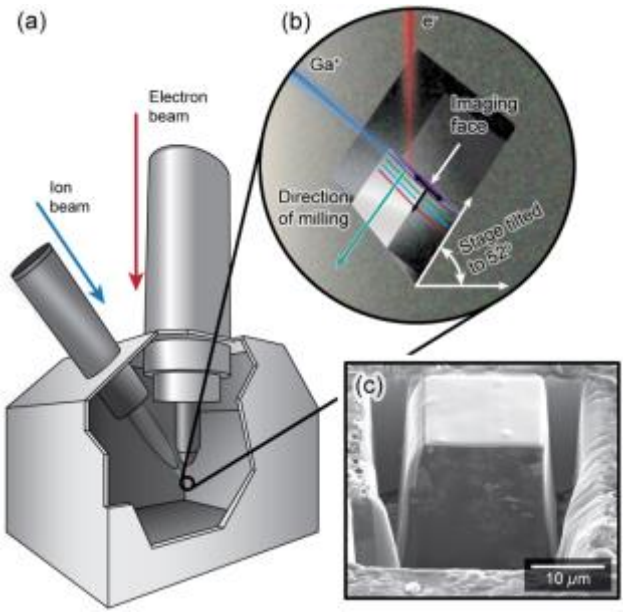

Figure 2.4. Microscope set up for FIB-nt: (a) Simplified graphic of a dual beam FIB-SEM instrument showing the orientation of the ion and electron beams; (b) Standard geometry of sample within FIB-SEM chamber for milling and FIB-nt [adapted from Holzer *et al*. (2004)]; (c) Example showing a sample (S3.1 – reconstructed volume shown in Figures 3.13a and b) prepared for FIB-nt; the sample is oriented at an oblique angle relative to the electron beam as shown in (b) enabling imaging of the ion milled cross-section (image captured using secondary electron).

maintain regular intervals (i.e. slice thicknesses) between consecutive image slices. Slice thickness should be the same magnitude as the pixel size of the volume to ensure an isotropic voxel resolution (3D pixel) (Holzer *et al*., 2006; Bushby *et al*., 2011). This is achieved by applying automated correction algorithms during the serial sectioning procedure, which reduce or eliminate drift phenomena. The regular spacing between individual image slices allows entire image sequences to be transformed directly into voxel-based (3D pixel) data volumes suitable for quantitative analysis (Holzer *et al*., 2006; Bushby *et al*., 2012).

2.3.3. Millimetre Datasets; 3D X-ray μCT

μCT scanning was performed using a Nikon (Tokyo, Japan) Metrology XT-H 225™ microtomograph. This CT scanner is equipped with an X-ray source that generates polychromatic X-rays from a tungsten metal target with a focal spot size of ~10 μm. During data acquisition the source was operated at a voltage of 150 kV and a current of 160 μA. A 1 mm thick copper (Cu) filter was used to absorb X-rays in the lower end of the energy spectrum, i.e. 'soft' X-ray with energies <30 kV (Davis & Elliott, 2006). The elimination of soft X-rays creates a more monochromatic beam (i.e. decreases the spectral spread), reducing

the effects of beam hardening and ring artefacts (Mees *et al*., 2003; Ketcham & Carlson, 2001; Davis & Elliott, 2006; Cnudde & Boone, 2013). However, whilst this is a necessary correction procedure, it results in a decrease in the signal to noise ratio of the scans (Davis & Elliott, 2006; Remeysen & Swennen, 2008). The result of scanning was 1,024 × 1,024 pixel radiographs with a 16-bit grey-scale depth (65,535 grey-scales) that represent differences in X-ray attenuation, related to material density and the absorbing material's attenuation coefficient (Duliu, 1999; Mees *et al*., 2003). The acquisition time selected for each projection was 2829 ms. Each scan produced ~1,600 individual X-ray projections, which after reconstruction within CTPro3D (Nikon Metrology, Ray, 2011), yielded cubic volumes with dimensions of 1,024 × 1,024 × 1,024 voxels. During reconstruction imaging artefacts such as beam hardening and positioning error were also addressed.

2.4. Stage 3: Processing and Analysis of Correlative Datasets

All image processing steps were conducted using the imaging software Fiji/ImageJ v2 (Abramoff, 2004; Schindelin *et al*., 2012; 2015). The reader is referred to Appendix IV for comprehensive description of the steps taken during image/dataset reconstruction, processing, and visualisation. To address the inherent misalignment between consecutive images within FIB-nt stacks and remove artefacts associated with the drift of the electron beam or sample, an alignment algorithm was applied using the StackReg plugin (Thévenaz *et al*., 1998). Image sequences were then cropped to retain the maximal overlapping area. Image enhancing filters were applied to each of the multi-modal datasets individually to improve their signal to noise ratio. To remove large spatial variations in image intensity, sequences were subjected to a background correction filter, whilst noise reduction was achieved using a 2D/3D median filter (e.g., Goldstein *et al*., 2007; Holzer *et al*., 2004). Segmentation was performed initially within Fiji using the Trainable Weka Segmentation (TWS) plugin v2.1.0 (Arganda-Carreras, 2015), a semi-automated tool capable of machine learning (see § 3.3.3), after which volumes were imported into Avizo® v9.0 (Visualization Sciences Group, 2015) for further manual feature splitting. Subsequently, volumetric renderings were produced within the software package Drishti v2.6.2 (Limaye, 2006), in which the transfer function editor, in addition to colour and transparency settings, permitted specific properties (i.e. false colour and opacity) to be assigned to segmented materials.

Chapter Three: Results

3.1. Introduction

In this chapter the results of the correlative multi-modal and multi-scale investigation of estuarine flocs are presented. In total two floc samples, S4 and S5, were subjected to correlative analysis. Datasets were obtained using different imaging techniques at three scales or levels of observation: the nanometre (using TEM and STEM), micrometre (using SEM and FIB tomography) and millimetre-scale (using X-ray μCT). In order to distinguish the features that can be recognised at each observational level these datasets are organised into separate sections according to the scale from which they were collected, and are described and analysed separately. Subsequently, the multiple datasets are fused into a single '3D scene' to understand better the relationships and interactions between floc components across the length-scales.

3.2. 2D Datasets Obtained at the Nanometre-Scale

3.2.1. Introduction

This section describes the results of 2D TEM and STEM imaging and TEM-EDS point chemical analysis of the floc samples. The nanometre resolution of TEM and STEM images provided a means of characterising the constituents of the flocs, the identification of which could be confirmed by TEM-EDS. Visual inspection of the image data also provided information regarding the spatial arrangement of the constituents of the flocs in 2D.

3.2.2. 2D STEM Images and TEM-EDS Spectra

The classification of floc components at the nanometre-scale relied upon a combination of shape, size, electron opacity and elemental analysis by TEM-EDS and STEM imaging, a guide to which is outlined in Leppard (1992a). Figure 3.1 shows a selection of dark-field STEM images with pixel resolutions of 6 – 20 nm^2 taken from microtomed thin-sections across the top of sample blocks S4 and S5. Figures 3.1a and c – g are in normal contrast, whilst Figure 3.1b is in inverted contrast as would normally be seen in bright-field TEM. Figures 3.1a – e illustrate the different materials commonly observed within the floc samples,

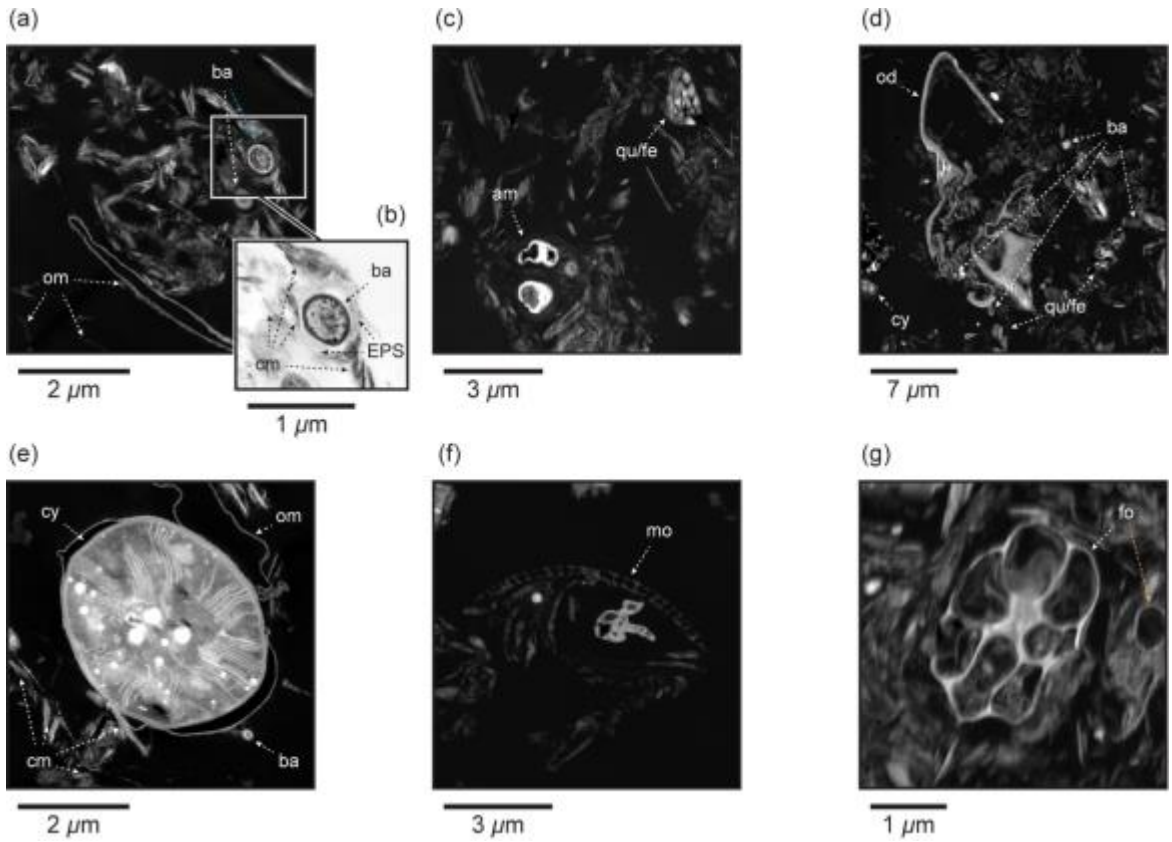

Figure 3.1. Selection of dark-field STEM images showing examples of commonly observed features and more 'exotic' objects; (a) Planar clay minerals (cm), bacterial cells (ba) and organic membranes (om); (b) Magnified sub-set of (a) showing the internal structure of a bacteria and surrounding EPS matrix filling the void space between the cell and radially arranged clay minerals (contrast inverted); (c) An amoeba (am) and 'bulky' non-clay mineral [likely to be quartz (qu) or feldspar (fe)] surrounded by clay platelets. Note how the non-clay mineral appears shattered and individual crystals appear dislocated; (d) Large particle of organic detritus (od) surrounded by clay minerals and bacterial cells. A filamentous cyanobacteria (cy) is also observable in the bottom left corner of the image; (e) Cyanobacterium surrounded by clay minerals; (f) Mollusc larvae (mo); (g) Foraminifera (fo) surrounded by clay minerals. The blue arrow in (a) denotes a bacterium around which clay minerals are organised radially, whilst the orange arrow in (g) denotes a partially visible foram.

which include clay minerals, non-clay mineral grains (e.g., quartz, feldspar and mica etc.), microbial cells, EPS and amorphous organic detritus. Less common features including plankton (e.g., mollusc larvae and foraminifera, examples of which are shown in Figures 3.1f and g respectively) and bioclasts (e.g., frustules and foram tests) were also recognised.

Bioorganic constituents and biota were distinguished from minerogenic particles within STEM images based on their grey-scale values, which were relatively high due to heavy metal staining. Further confirmation of the identity of organic constituents was provided by TEM-EDS, which showed signals for Os, Pb and U in the stained organic structures, illustrated in Figures 3.2a – c. Distinction between different 'species' of organic constituents

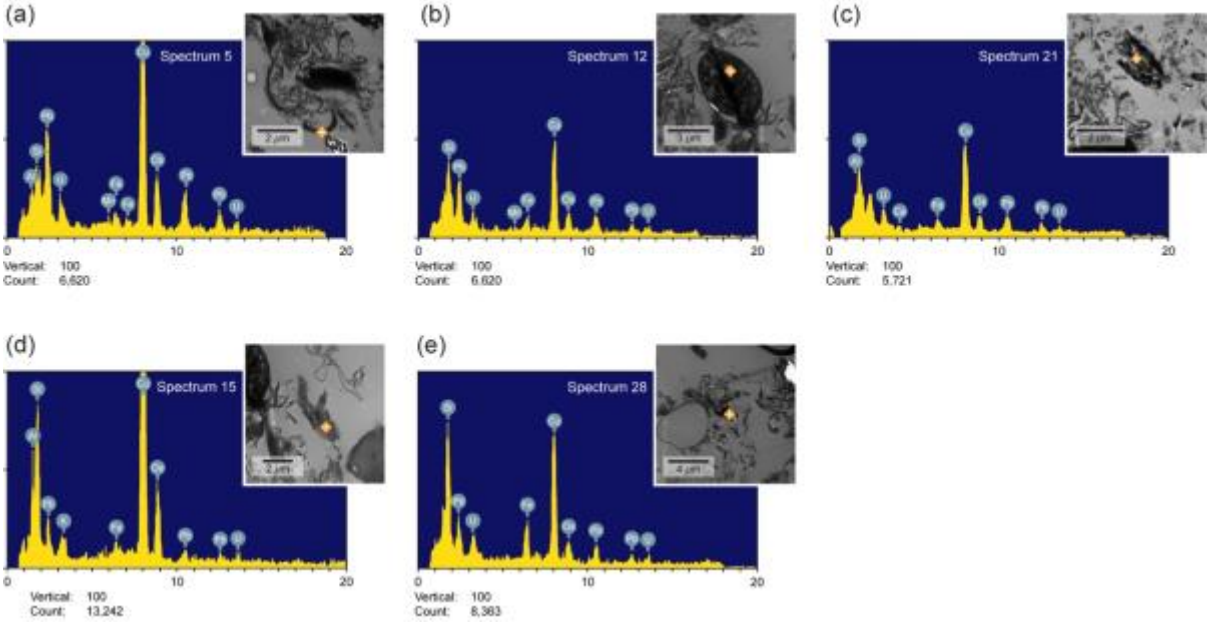

Figure 3.2. Selection of spectra from TEM-EDS applied to common floc constituents and accompanying TEM bright field micrographs. The cross on micrographs indicates the position of the beam that the X-ray spectra were acquired from. Note that the copper peak present within all spectra is a background signal from the supporting grid; (a) Organic detritus associated surrounded by clay platelets; (b) Filamentous cyanobacterium; (c – d) Multi-particle units of tightly packed clay minerals. The inter-particle pore space between clay minerals is likely to be filled with organic matter, hence the signals for Os, Pb and U. Signals for calcium and aluminium in (c) and potassium and aluminium in (d) indicate the presence of montmorillonite (Ca+Al+Si+Mg) illite (K+Al+Fe+Mg) clays respectively; (e) Non-clay mineral grain surrounded by clay platelets, probably quartz or iron oxide.

was possible through analysis of their ultrastructural detail, morphology and size. Particles of organic detritus (e.g., decayed plant matter) were characterised by their complex morphology and lack of internal structure, often appearing homogenous and ranging in size up to 20 μm in diameter (e.g., Figure 3.1d). Unicellular organisms were found to be present in both floc samples and could be distinguished as either planktonic eukaryotes or prokaryotes on the basis of their dissimilar size and distinctive morphologies. Whilst the majority of prokaryotes were relatively small, with diameters of <1 μm, eukaryotes were observed to be an order of magnitude larger with diameters often >10 μm. Further distinction between eukaryotic and prokaryotic cell types was provided through investigation of their complex sub-cellar structure, which at high magnifications was shown to be preferentially stained. This is illustrated in Figures 3.1b, d and e in which the ultrastructural details of cells are clearly visible, enabling eukaryotic cells to be recognised from prokaryotes by the presence of a nucleus.

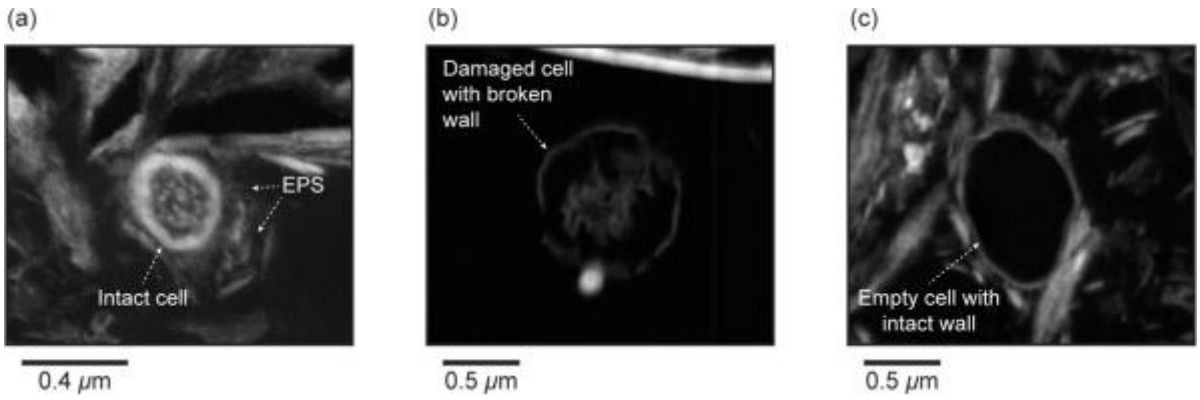

Figure 3.3. Selection of dark-field STEM images showing examples of the three categories of intracellular integrity used as an indicator of the fidelity of stabilised flocs to their original structure; (a) intact bacteria displaying an undamaged cell wall, cytoplasm (grainy structure) and nucleoplasm (denser region towards the centre of the cell); (b) damaged bacterial cell with a broken cell wall and degraded cytoplasm and/or nucleoplasm; (c) empty cell lacking plasma.

Certain eukaryotes were observed to be encased within shells and identified as 'testate', enabling their distinction from 'naked' forms of eukaryotes (e.g., amoebas) which lacked hard external shells. Based on the distinctive geometric structure and elemental composition of tests/shells several groups of eukaryotic plankton were identified including coccolithophores, diatoms and foraminifera. Fragments of biogenic mineral constituents (e.g., diatoms frustules) were also observed and could be allocated to the group from which they originated depending on their state of preservation. The 2D nature of the image data made it impossible to separate planktonic prokaryotes based on their morphotype (e.g., cocci, bacilli and vibrio etc.). However, three types of filamentous cyanobacteria, with diameters of ~1 μm, ~2.5 μm and 4 – 5 μm, were identified which appeared to be occupied by a diverse range of structures including thylakoids and granules (e.g., Figures 3.1d and e).

Careful examination of the internal and external structure of microbial cells provided information regarding their integrity, and cells could be classified as intact, damaged or empty following the criteria described by Heissenberger *et al*. (1996a). Examples of these three categories of intracellular integrity are given in Figure 3.3. Cells recognised as intact were undeformed and possessed all cell components, including an intact cell membrane and undegraded cytoplasm and nucleoplasm. Damaged cells were defined as lacking at least one of the above criteria for intact cells, and were usually easily identifiable due to their deformed or ruptured cytoplasmic membrane. Empty cells displayed intact or partly intact membranes but lacked internal structure. Intact bacterial cells typically exhibited well-developed capsular envelopes or 'sheaths' composed of fibrillar EPS (Figures 3.1b and c) whilst damaged and

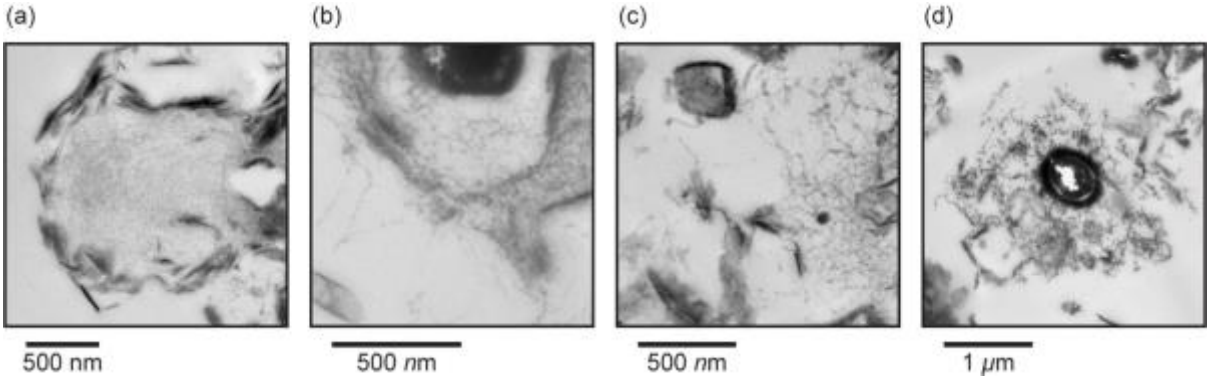

Figure 3.4. TEM bright field micrographs showing examples of the different morphotypes of fibrillar EPS commonly observed within the floc samples; (a) Meshwork of fine fibrils; (b) Fine fibrils and more 'ribbon like' EPS; (c) Predominantly ribbon like fibrils; (d) Thick capsular fibrils with 'globular' attachments, likely to be humic substances.

empty cells usually lacked such envelopes. This bound EPS, closely associated with the walls of bacterial cells, could be distinguished from soluble EPS that was loosely or unassociated with cells. Soluble EPS (diameter, 2 – 15 nm) was observed to be abundant in both floc samples and displayed a variety of morphotypes as shown in Figure 3.4.

Elemental analysis of inorganic particles by EDS showed signals for Al, Ca, K, Fe and Si (Figures 3.2d – 3.2e). Considering the spectra and accompanying TEM images, the principal mineral phases of the floc samples are likely to be clays, non-clay silicates (e.g., feldspar, mica and quartz) and carbonate minerals. Clay minerals were characterised by their small size (diameter, <3 μm), planar morphology and low to mid-range grey-scale values (Figure 3.1a). In contrast, non-clay minerals ranged in size from 2 – 30 μm in diameter and displayed mid-range grey-scale values. A certain degree of distinction could be made between different species of non-clay particles based on their shape and size as described by Mitchell & Soga (2005). Common species found within the floc samples such as calcite, plagioclase feldspar, pyrite and quartz were characteristically angular in 2D cross-sections (Figure 3.1c), whilst other species including orthoclase feldspar were more elongated. In comparison, mica is composed of thin plates which made it easily recognisable within the STEM micrographs (see Figure 3.6a). Further confirmation of the identity of non-clay minerals was provided by EDS investigations in addition to grey-scale contrast which could be used to distinguish minerals which had significantly different backscattering coefficients. Most non-clay silicate minerals within the STEM images displayed some degree of shattering, and were observed to have dislocations in their crystal structure (Figure 3.5). While such features do occur naturally it is more likely that they are defects known as 'slip

planes' caused by deformation during the sectioning procedure. This is confirmed by the presence of loose particles on the face of the thin-sections which are recognised as having been plucked from their proper positions within the mineral grains. A number of loose grains can be identified in Figure 3.5 in close proximity to a shattered non-clay mineral which overlap particles within the thin-sections underneath.

Individual TEM and STEM images were suitable for characterising the constituents of the flocs but have a limited field of view. Therefore, in order to describe the abundance and spatial arrangement of different constituents, systematic imaging of the thin-sections in a

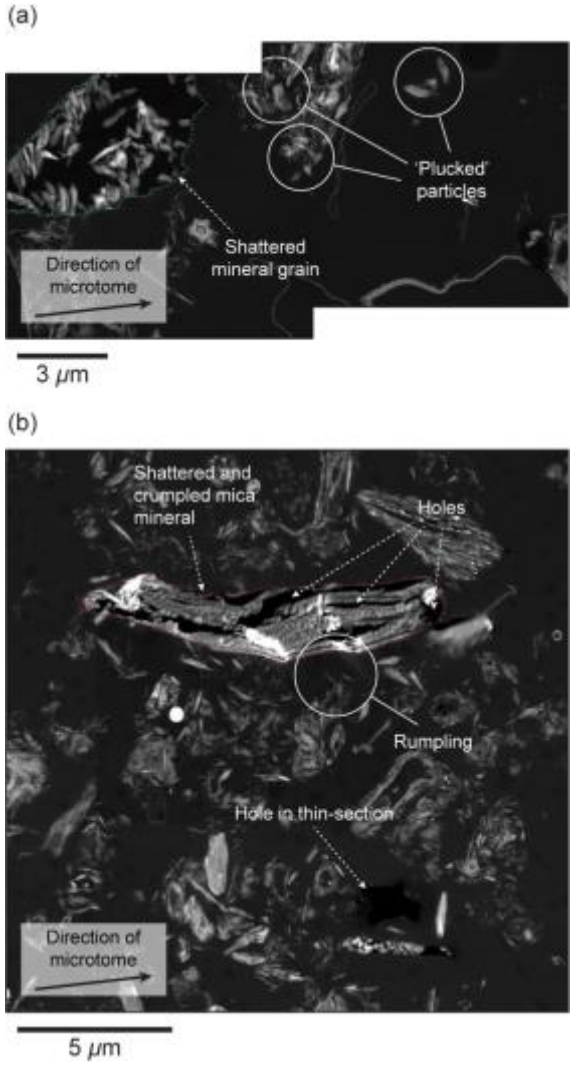

Figure 3.5. Dark-field STEM images showing examples of defects in the thin sections; (a) Shattered mineral grain (denoted by the dashed green line) and plucked particles in close proximity. Note that the plucked particles are loose on the surface of the thin-section and can be seen here to overlap particles in the underlying thin-section; (b) Crumpled mica grain (denoted by the dashed red line), small holes and signs of thin-section dishevelment in the form of 'rumples'. The direction of the microtome cut is indicated in both images.

grid-pattern produced STEM image montages which provided 'panoramic' views of the floc sample at nanometre resolution. Figure 3.6a shows an STEM image montage collected from floc S5. This montage, which covers roughly half the floc matrix exposed within the sectioned block-face, was created by stitching together ~170 images each with a pixel size of 6 nm^2 using the Grid/Collection Stitching plugin in Fiji/ImageJ (see Figure AIV.3 in Appendix AIV) (Preibisch *et al*., 2009).

It can be observed from Figure 3.6 that floc constituents are not evenly distributed within the floc matrix but are assembled into structural units at different spatial scales. At the nanometre-scale individual particles – particularly clay minerals – are rarely observed in isolation but are instead found in multi-particle units. These typically consist of 10's of clay minerals aligned parallel with face-to-face contacts in stacked or slightly offset arrangements (Figures 3.6c and d). Associations consisting of these multi-particle units were observed throughout flocs S4 and S5, and commonly exhibited face-to-face or edge-to-face contacts (Figures 3.6c and d). Alternatively, where associated with either individual microbes, several microbes or larger non-clay mineral grains, multi-platelet particles of clays were found to be arranged around these larger particles (Figures 3.1a and 3.6e and f). Larger structural units composed of mixtures of both individual particles and multi-particle units were observed to exist at higher spatial scales within the STEM image montage. These ranged in size from 5 – 40 μm and were typically highly porous, exhibiting open 'card-house' structures as illustrated in Figures 3.6g and h. More 'compact' units (diameter, ~30 μm) comprised of densely packed clay minerals were also observed albeit less frequently (Figure 3.6i). Here we term these structural units 'microflocs' (Figure 3.6h) and note that this is a different definition to that traditionally used in floc characterisation (see § 1.2 and 1.3). Detailed observation of the intra-aggregate pores of these microflocs shows that they are typically filled with fibrillar EPS (see Figures 3.1a and 3.6g). This is in contrast to the larger inter-aggregates pores that separate microflocs which usually appeared to be devoid of physical structure.

Observations of the cell types present within the individual STEM images and larger STEM montage from S5 suggests prokaryotes to be the dominant microbiota of the floc samples. These are shown to be abundant in both samples and are observed in various assemblages from single cells (some of which are in the process of division) to groups consisting of several bacteria. Of the 236 cells identified in the STEM image montage 131 (55.5%) were identified as being intact whilst 66 (28.0%) cells were shown to be damaged and 39 (16.5%) were recognised as empty.

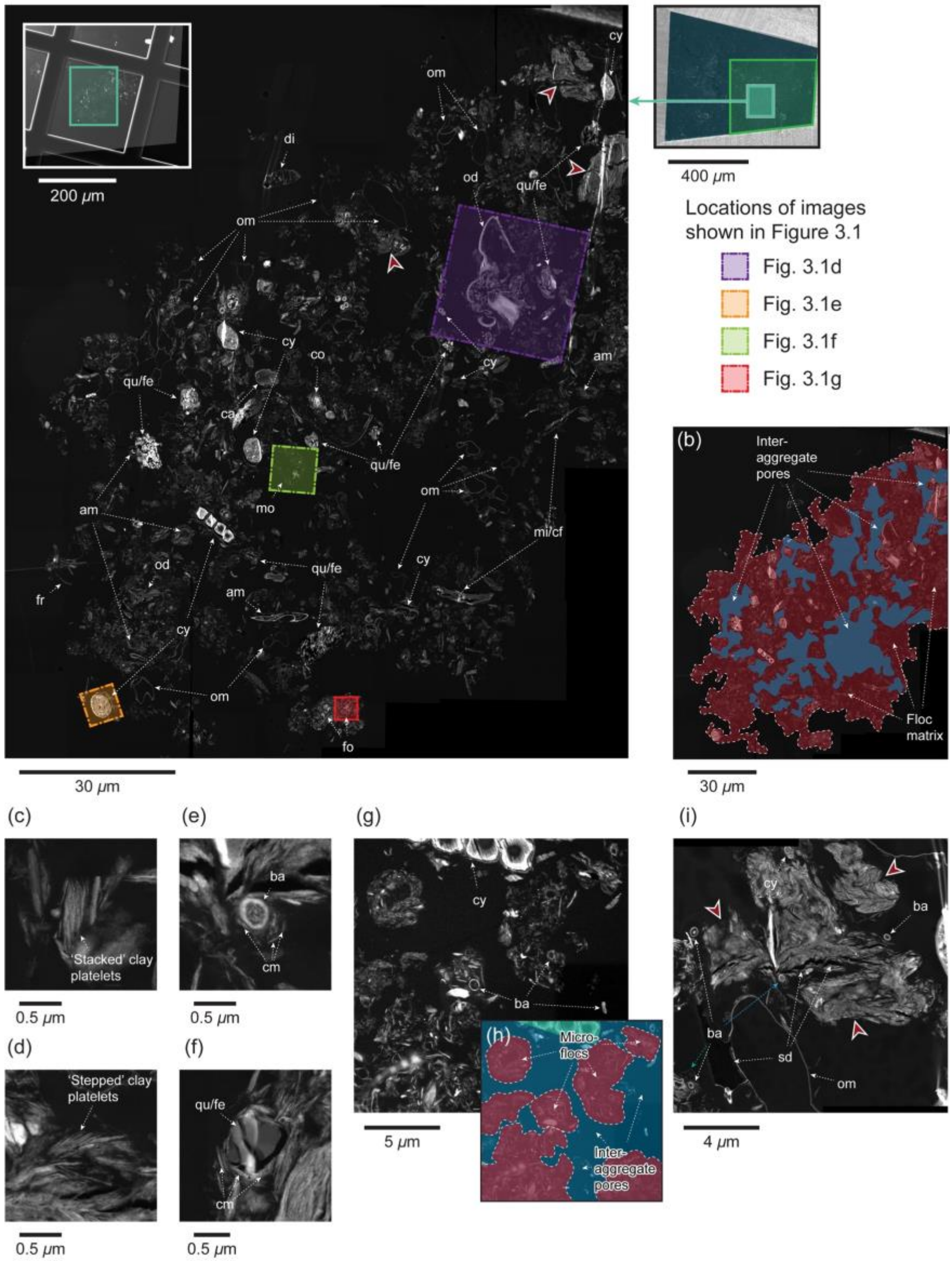

Figure 3.6. Individual dark-field STEM images and image montages that show the structure of the floc samples with nanometre resolution: (a) Dark-field STEM montage collected from floc S5; the inset image in the top left corner shows an overview of the thin-section from which the montage was collected, whilst in the top right hand corner an SEM-SE image shows its position in relation to the sectioned block-face of the sample (denoted in both instances by a light-green box); (b) Binary mask of (a) which distinguishes inter-aggregate pore space from the floc matrix; (c – d) Multi-platelet particles consisting of clay minerals assembled in stacked (c) or stepped (d) arrangements; (e – f) Primary associations consisting of clay minerals arranged radially around a central particle, in this instance an individual bacterium (e) and a mineral grain (f); (g) Typical microflocs composed of several multi-particle units organised in an open card-house structure; (h) Binary mask of (h) showing microflocs and inter-aggregate pores; (i) Compact microfloc unit consisting of closely associated clay minerals. Compact regions of the floc (often comprised of closely associated clay minerals) are indicated by the red arrows. am, eukaryotic cell; ca, carbonate; cf, large clay mineral; co, coccolith; cy, cyanobacterium; di, diatom; fe, feldspar; fo, foraminifera; fr, frustule; mi, mica grain; mo, mollusc larvae; od, organic detritus; om, organic membrane; qu, quartz.

Visual inspection of the STEM image montage revealed defects caused during ultramicrotomy by the shear stresses imposed on the thin-sections when they were cut. These defects included: (1) *folds and rumples* – identified as regions of irregular contrast caused by the increased thickness of the thin-section where it has been folded over on itself (Figures 3.5b and 3.6a); (2) *slip planes* – recognised as defects in the crystal structure of large non-clay minerals which appeared shattered as a result (described above, Figures 3.1c and 3.5a); (3) *holes and tears* – typically observed around mineral grains but also in isolation (Figure 3.5b). Compression of the whole thin section is also likely to have occurred. Whilst difficult to quantify, compression can be studied by comparing measurements between features aligned in the direction of the cut observed in the thin-sections with measurements between the same features identified on the surface of the sample block (using SEM). Measurements made in this way determined the thin-sections to have been linearly compressed by ~14%.

3.2.3. Summary

High-resolution TEM-EDS and STEM applied to ultrathin-sections collected from the block-face of the samples demonstrate the complex composition and nano-scale structure of the estuarine floc samples. The flocs are revealed to be composed of a diverse range of organic and inorganic constituents which can defined by their size, shape, electron opacity and elemental signature. Visual evidence suggests that flocculated material is assembled into structural units at different spatial scales.

3.3. 2D and 3D Datasets Obtained at the Micrometre-Scale

3.3.1. Introduction

This section describes the results of 2D SEM imaging and SEM-EDS mapping in addition to 3D FIB-nt. As noted in Section 3.1, correlative datasets were obtained from two samples, S4 and S5. Here, a third floc sample labelled S3 is introduced to assess the relative utility of the primary imaging modalities of the SEM (SE and BSE) to identify different features in both 2D and 3D. The preliminary results obtained from S3 helped guide the imagining conditions subsequently selected for the collection of 2D and 3D datasets from S4 and S5 (shown in Table 3.2).

Operation	Sample (and ROI)	Probe	Process	Voltage (kV)	Current (nA)	Time
SEM Imaging	S3	SEM	SE Imaging	3	0.373	5 mins
		SEM	BSE Imaging	3	1.47	
SEM Montaging	S4	SEM	SE Imaging	3	2.55	1 hr 30 mins
	S5	SEM	BSE Imaging	3	4	
FIB-nanotomography	S3.1	FIB	Trenching	30	1 – 0.5	4 hrs 35 mins
			Serial Sectioning	30	0.5	8 hrs 10 mins
		SEM	SE Imaging	10	0.082	
	S3.5	FIB	Trenching	30	1	3 hrs 15 mins
			Serial Sectioning	30	0.5	18 hrs 50 mins
		SEM	BSE Imaging	10	0.373	
	S5.1	FIB	Trenching	30	1 – 5	4 hrs 30 mins
			Serial Sectioning	30	0.5	13 hrs 30 mins
		SEM	BSE Imaging	3	4	
	S5.2	FIB	Trenching	30	1 – 5	1 Day 4 hrs
			Serial Sectioning	30	3	19 hrs 50 mins
		SEM	BSE Imaging	3	4	

Table 3.1. Ion and electron beam parameters during SEM imaging and serial sectioning.

Section 3.3.2 describes the 2D micrometre-scale datasets obtained from the floc samples S4 and S5. These were used to characterise the entire 2D working surface of the flocs and locate sites suitable for FIB-nt. In Section 3.3.3 3D data volumes obtained via FIB-nt are described which provide insights into the arrangement of floc constituents in 3D.

3.3.2. 2D SEM Images and SEM-EDS Maps

Figure 3.7 shows individual SEM images taken from a FIB-milled cross-section of floc sample S3 which highlight the different features that can be resolved using either SEs or BSEs. Images formed using SEs typically have a higher spatial resolution enabling individual clay platelets to be identified as shown in Figure 3.7a. Although at 10 kV many SEs will be generated by BSEs, the secondary electron detector produces weak atomic number contrast

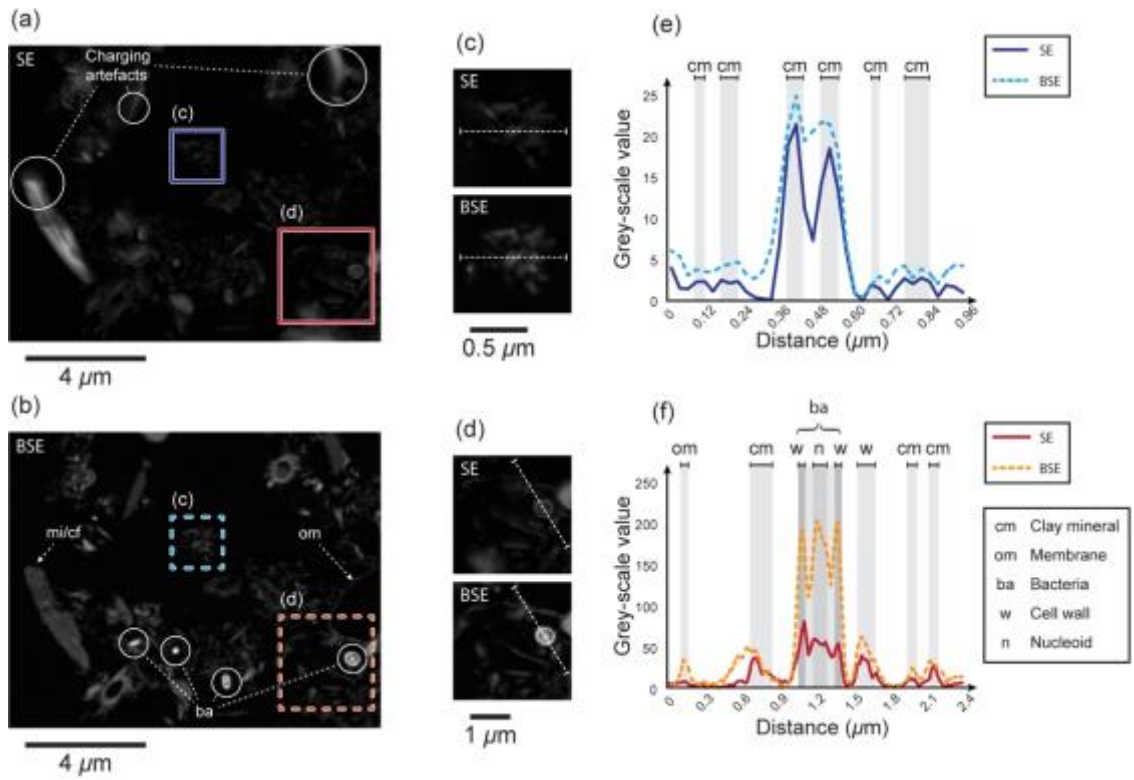

Figure 3.7. SEM images of a FIB milled cross-section generated using SEs (a) and BSEs (b) respectively and sub-sets isolating a cluster of inorganic particles (c) and a bacterium (d). The dashed lines in (c) and (d) indicate the position of the adjacent grey-scale line profiles shown in (e) and (f).

compared to the direct detection of the BSEs (Figure 3.7b), resulting in organic and inorganic constituents exhibiting similar grey level values (see Figures 3.7d and f). The large numbers of SEs generated can lead to charging artefacts appearing as bright patches in the image. In comparison, the grey level contrast of BSE images typically reflects the composition (average atomic number) of a specimen. This is clearly demonstrated in Figure 3.7b in which stained organic structures (e.g., bacteria and organic membranes) that cannot be distinguished in the SE images are shown to be enhanced in the BSE image. Fine structural detail (e.g., individual clay platelets) recognisable in SE images is, however, more difficult to resolve in images formed using BSEs due to the poorer spatial resolution of the signal, even at the low (3 kV) accelerating voltages used (see Figures 3.7c and e).

For the purpose of registration 'reference' images were taken from the block-face of samples S4 and S5 using SEs (Figures 3.8b and e). The SE images provided topographical contrast necessary to recognise the trimmed block-face of the samples, which, measured from the 'top' of the flocs (relative to their position within the sample blocks), were 504.3 μm (22.3%) and 201.2 μm (4.5%) from the tops of flocs S4 and S5 respectively (see § 3.5.2,

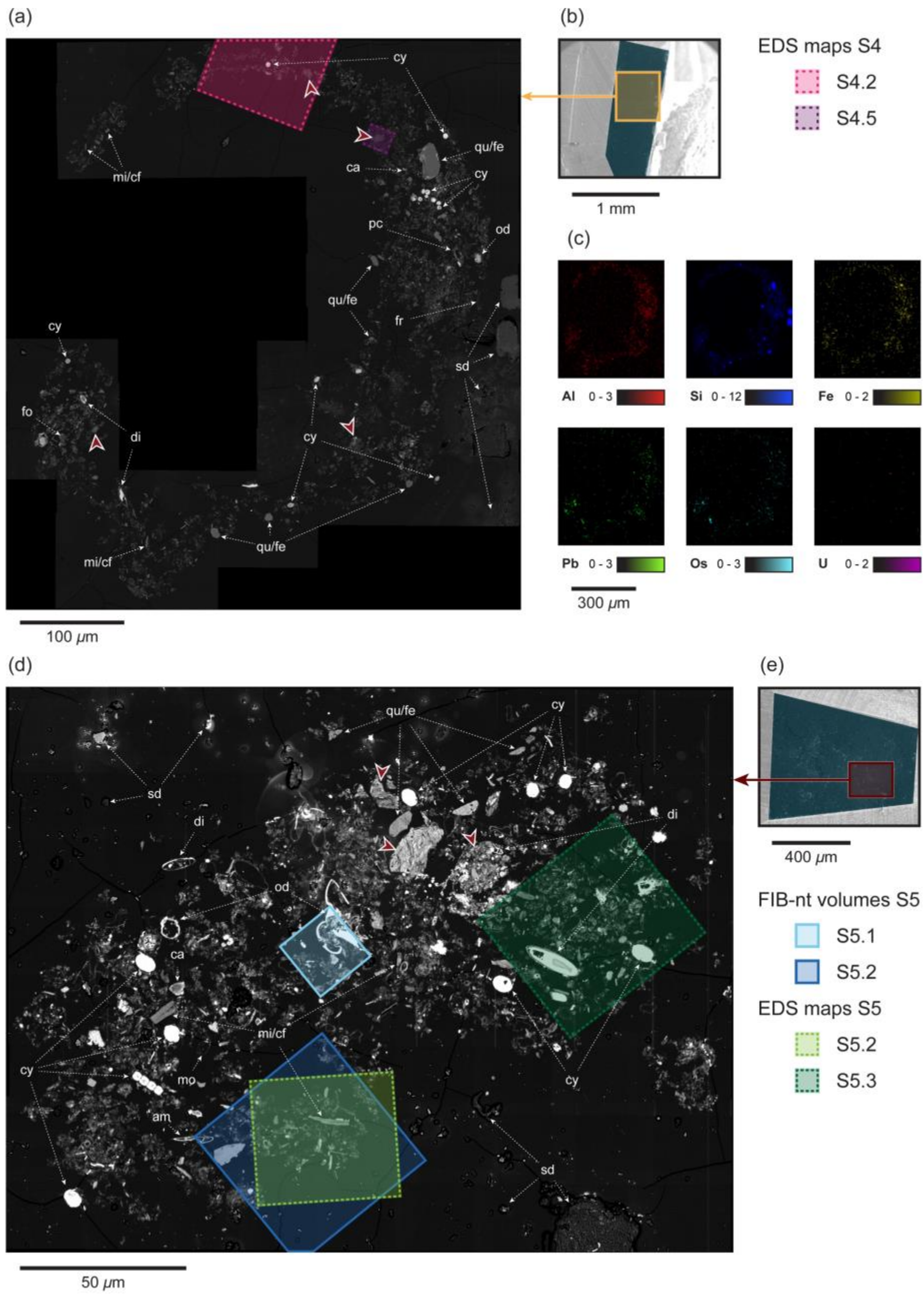

Figure 3.8. SEM-BSE image montages of the entire cross-section of flocs S4 (a) and S5 (e) exposed within the section block-face of samples. The locations of RoI selected for further analysis via elemental mapping and 3D FIB-nt volumes are also shown. (b and e) SE images taken from the block-face of the samples that give the location of the montages; (c) EDS elemental maps taken from the surface of S4. Compact regions of the floc (often comprised of closely associated clay minerals) are indicated by the red arrows; note the example on the left which appears to contain frustules. am, eukaryotic cell; ca, carbonate; cf, large clay flake; cy, cyanobacterium; di, diatom; fe, feldspar; fo, foraminifera; mi, mica grain; od, organic detritus; mo, mollusc larvae; pc, plant cell; qu, quartz; sd, surface damage (e.g., salt deposits, dust etc.).

Figures 3.16 and 3.17). However, their lack of compositional information made them unsuitable for characterising the floc matrix. For this, BSE images with compositional contrast were acquired. Figures 3.8a and d show SEM-BSE image montages collected from samples S4 and S5 respectively. Similar to the STEM montages described in Section 3.2, the acquisition of montages via SEM involved systematic imaging of the sample blocks in a grid-pattern to collect 10's – 100's of images which were subsequently stitched together using the Grid/Collection Stitching plugin in Fiji/ImageJ (Preibisch *et al.*, 2009). Whereas the acquisition of STEM images is time-consuming, limiting the feasibility of STEM montaging to sub-regions of the flocs exposed surface, SEM images with their wider field of view can be acquired relatively quickly with a small sacrifice in resolution. SEM montaging is therefore ideal for obtaining a complete picture of a flocs cross-section. This provides the context to allow the identification of suitable regions of interest (RoI) to target for further analysis, and subsequently interpret the results of these analyses in relation to the entire floc. The montages collected from S4 and S5 were created by stitching together 80 – 150 individual images each with a pixel resolution of 30 – 60 nm^2, and show the entire cross-section of the flocs exposed within the sectioned surface of the sample blocks.

The 2D cross-sections of flocs S4 and S5 are distinctly different in both their outward morphology and size. Whilst the cross-section of floc S4 is more elongated, displaying a distinctive 'horse shoe' shape with a diameter of ~560 μm (Figure 3.8a), the cross-section of S5 is comparatively smaller (>250 μm) and more compact (Figure 3.8b). It must be noted that the appearance of the flocs in the cross-sections is determined by the characteristics of the individual flocs themselves, and the location and orientation of the sectioned block-face within the floc samples. Despite the apparent differences in their outward morphology, S4 and S5 share similarities in their structural organisation. Material within both flocs are shown to be organised into structural units at different spatial scales, which corroborate TEM and STEM investigations at the nanometre scale. However, unique to floc S4 were narrow, elongated channels delimited by organic membranes. The position of RoI S4.2 shown in Figure 3.9a locates an example of one of these channels. Material can be seen to be closely associated with the organic membranes which define the pore channel, which are likely to act as a physical barrier separating the channel from the intra-aggregate pores of the surrounding floc matrix.

Similar to STEM, floc constituents within the SEM-BSE montages can be defined based by their shape, size and grey-scale value. For floc sample S4, further confirmation of the floc's composition was provided by SEM-EDS, which showed strong signals for Al, Si, Fe, Pb, Os and U (Figure 3.8c). Trace signals for other elements including Mg, Mn and Ca were also observed but are not presented. Selected materials are labelled in Figures 3.8a and d which were identified following the same criteria used to classify constituents in STEM images and montages described in Section 3.2. The more limited resolution of SEM restricts the individual constituents that can be resolved, and small features in the nano-range (e.g., EPS and individual clay minerals) are impossible to observe. However, despite their coarser resolution, large constituents can be identified in the SEM-BSE montages that can be directly related to those seen in STEM images (e.g., non-clay minerals, cyanobacteria, large organic structures and plankton).

For each of the floc samples several RoIs were identified which contained structural features considered to be representative of those observed within the cross-section of the flocs. Having established the capacity of SEM-EDS elemental mapping in conjunction with contrast and morphological analysis of SEM-BSE images to identify materials and structures within the floc cross-sections, these methods were applied to investigate the RoI at higher magnification. Figures 3.9 and 3.10 show BSE images alongside SEM-EDS elemental maps obtained at 10 kV for RoI S4.2 and S4.5 (located within floc S4), and S5.2 and S5.3 (located within floc S5) respectively. The RoI varied in size depending on the structural feature(s) of interest, ranging between ~20 and 120 μm^2.

The RoIs S5.2 and S5.3 were comparable in size (~50 μm^2, see Figure 3.8) and positioned to capture individual microflocs, aggregate features consisting of mixtures of both individual particles and multi-particle units organised into open card-house structures. S5.2 was taken from a periphery position relative to the main body of the floc, and its boundary is clearly defined by surrounding inter-aggregate pore space (Figure 3.10a). In contrast, S5.3 was taken from a more central, denser region of occupation within floc S5 (Figure 3.10d). The superimposition of three or more elemental maps into a single multi-colour phase map provided a means of determining elemental associations, which, when compared with BSE images, enabled the precise classification of constituents and materials within the RoI. Figure 3.10g shows the phase map created by combining the signals for Os, Pb and U, which shows the distribution of organic material within S5.3. Strong organic signals relate to large

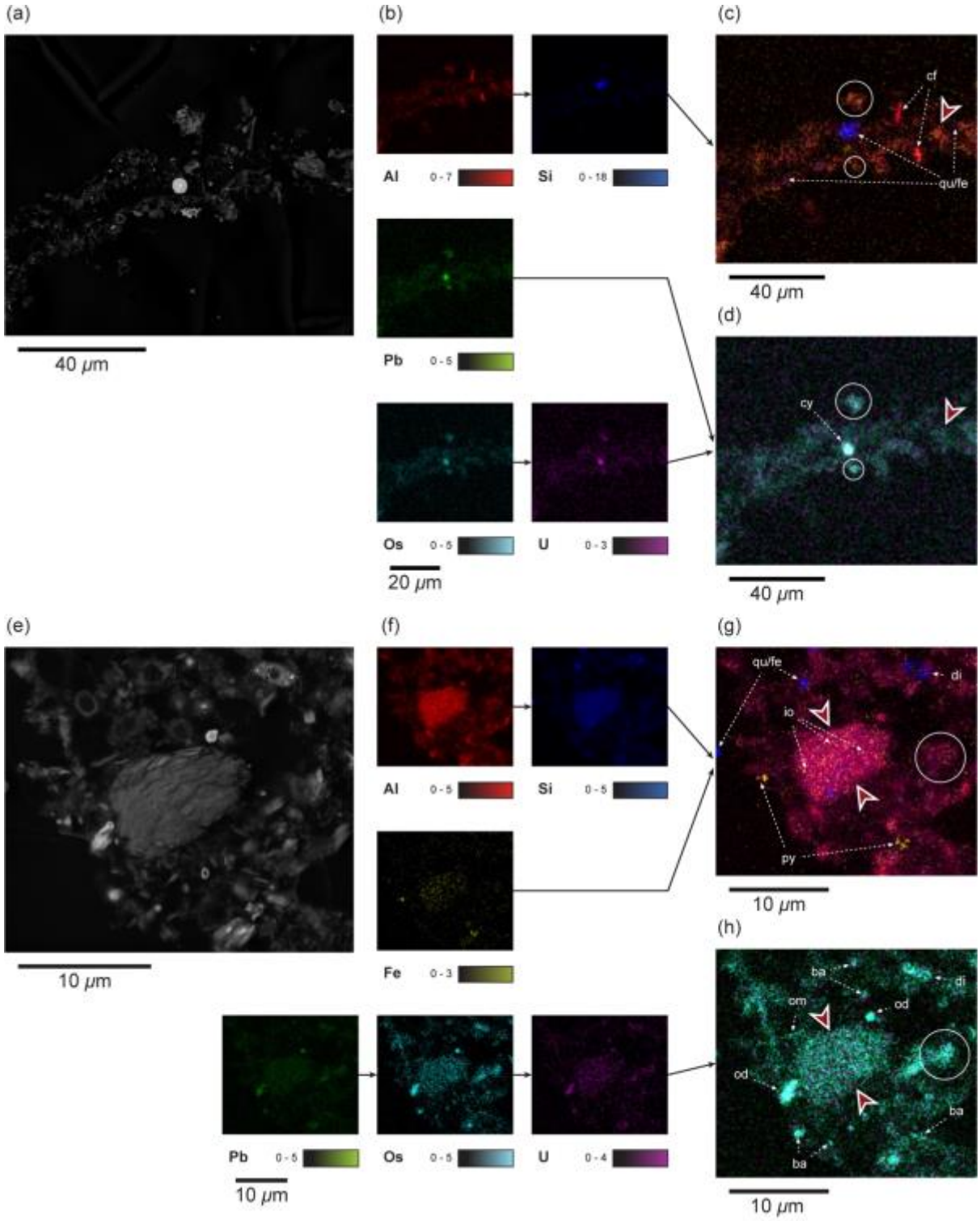

Figure 3.9. X-ray elemental maps collected from RoI S4.2 and S4.5, the locations of which on the sample block-face are shown in Figure 3.8. Different signals indicative of organic (e.g., Pb, Os and U) and inorganic (e.g., Al, Si and Fe) constituents are merged into separate false coloured phase maps. Compact regions within the RoI (often comprised of closely associated clay minerals) are indicated by the red arrows. Circles indicate organic rich areas. ba, bacteria; cf, large clay flake, cy, cyanobacterium; di, diatom; fe, feldspar; io, iron oxide; od, organic detritus; om, organic membrane; py, pyrite; qu, quartz.

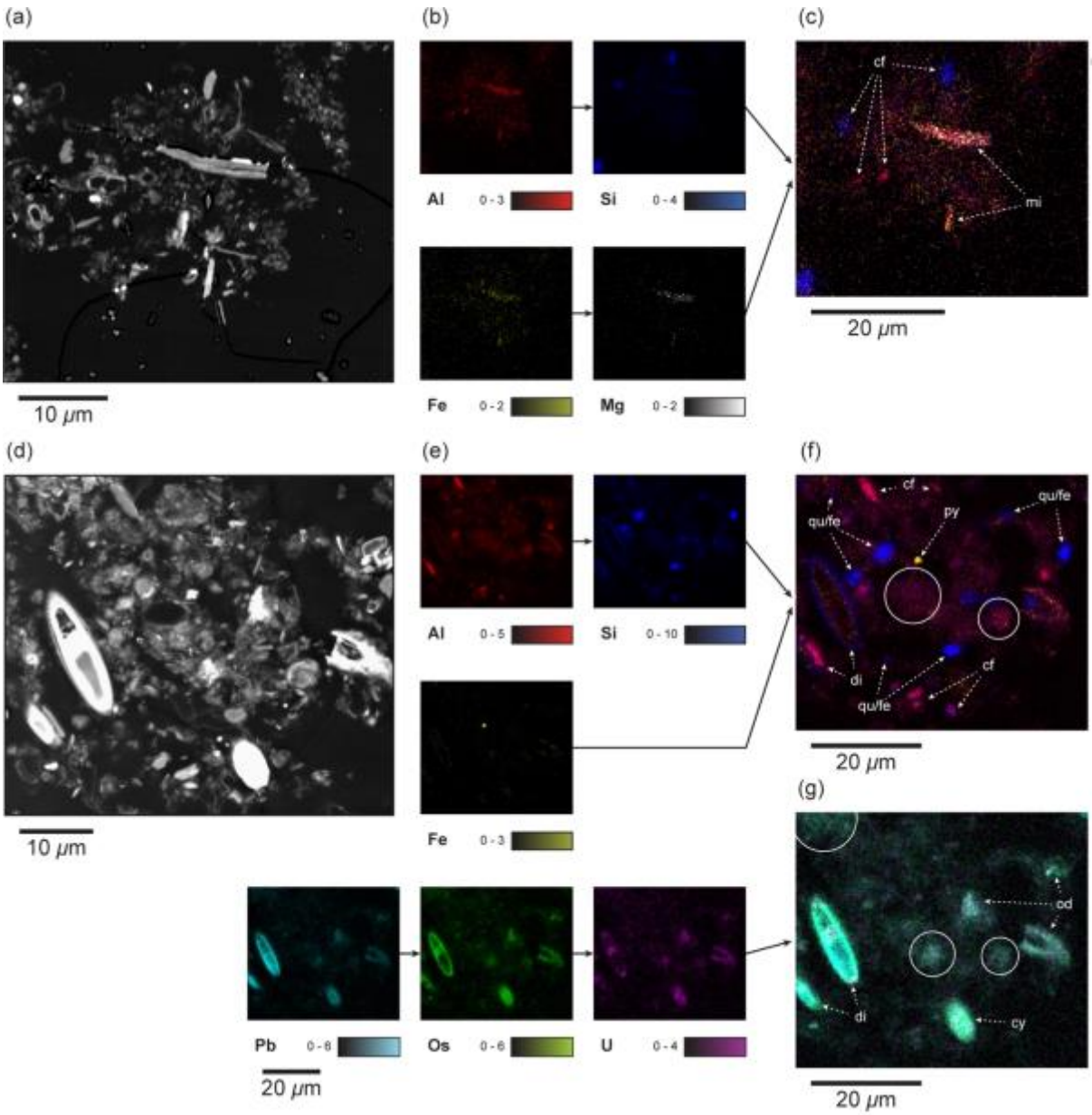

Figure 3.10. X-ray elemental maps collected RoI S5.2 and S5.3, the locations of which on the sample block-face are shown in Figure 3.8. Different signals indicative of organic (e.g., Pb, Os and U) and inorganic (e.g., Al, Si, Fe and Mg) constituents are merged into separate false coloured phase maps. Compact regions within the RoI (often comprised of closely associated clay minerals) are indicated by the red arrows. Circles indicate organic rich areas. cf, large clay flake, cy, cyanobacterium; di, diatom; fe, feldspar; od, organic detritus; py, pyrite; qu, quartz.

structures including diatoms, cyanobacteria and organic detritus. Figure 3.10b shows the signal for Si (blue), which is frequently corresponds to the positions of diatom shells. A weaker background signal of Pb, Os and U not correlated with any particular structure(s) is also observed from within the microfloc, but is noticeably absent from surrounding inter-

aggregate pores. This weaker signal is likely to originate from colloidal organic material within the intra-aggregate pores of the microfloc.

In comparison to S5.3, the signal from organic material within S5.2 (Figure 3.10a) is considerably lower and so the phase map for stained organics is not presented in Figure 3.10. The lack of an organic signal from S5.2 is not considered to be due to the absence of organic material, but a consequence of the relatively short dwell time (compared to S5.3) selected in order avoid severe electron beam damage and maintain a workable surface for FIB-nt. Signals for some elements, however, were strong enough to allow the identification of certain materials. Figure 3.10c shows the phase map created by combining the signals for Al, Fe, Mg and Si from S5.2, which gives an understanding of the inorganic constituents present within this microfloc and their distribution. The relatively large excitation volume (at accelerating voltage of 10 kV this will be on the order of microns) from which X-rays originate makes the identification of individual clay minerals difficult due to their small size. However, comparison of the phase map with the BSE image taken from S5.2 (Figure 3.10a) suggests that this microfloc is primarily composed of kaolinite type clays (Al+Si). Due to their larger size, individual non-clay minerals could be identified, including mica (Na+Al+Fe+Mg+Si), quartz (Si) and feldspar (Al+K+Si), and can be seen to be dispersed randomly throughout the microfloc. A similar assemblage of inorganic material is observed in S5.3 but the higher count rate enabled materials to be identified with more confidence (Figure 3.10f).

Although observed less frequently, compact microflocs consisting almost exclusively of closely associated clay platelets were observed to exist in both floc samples. Accordingly, RoI S4.5 was positioned to capture one of these. The example selected (shown in Figure 3.9e) was typical of other compact microflocs observed within the floc cross-sections. EDS elemental maps revealed the microfloc to be comprised of a mixture of illite (K+Al+Fe+Mg) and kaolinite (Al+Si) type clays and in iron rich phases (Fe+O) (Figures 3.9f and g). Pyrites (Fe+S) dispersed between the clay minerals were also identifiable based on their elemental signature, angular morphology and high grey-scale value in BSE images. Compared with open card-house structure microflocs, the intra-aggregate pores of the compact microfloc posed a much stronger organic signal as demonstrated in Figures 3.9f and h.

As described above, the outward morphology of floc S4 resembled that of a horse shoe, with material loosely organised into narrow extensions projecting from what was perceived to be the main body of the floc that was by comparison more compact (Figure 3.8a). Closer

inspection revealed that these narrow extensions consisted of primary particles (e.g., clays, non-clay minerals and organic debris etc.) arranged around filamentous organic membranes, the interior of which were usually devoid of structure. RoI S4.2 shown in Figure 3.9a (dimensions, ~100 μm^2), was positioned to intersect a typical example of one of these. EDS maps taken from the RoI corroborate visual interpretations of the BSE images, showing material to be arranged around a central membrane (Figures 3.9c and d). Unlike other regions which exhibited a 'ragged' transition between the exterior and interior of the floc, this boundary was found to be better defined along these narrow extensions.

3.3.3. 3D FIB-nt

3D reconstruction of the FIB-nt volumes required the identification of different components within 2D image sequences. This was achieved by simple grey-scale thresholding of the image data combined with 3D shape recognition. Modern software allows for a hybrid of these approaches to semi-automate data segmentation and greatly speed-up the process. Furthermore, the advantage of 3D datasets is that the segmentation in 2D can be verified by comparing adjacent images in 3D.

Figure 3.11 shows a comparison of simple thresholding versus a semi-automated segmentation tool for a single 2D image containing a cluster of floc components from a sub-volume (S3.1-1; Figures 3.11h – j) of the dataset presented in Figure 3.13a. 8-bit grey-scale images are divided into 256 grey levels with zero representing black and 255 representing white. A threshold level is set to create a binary mask to differentiate particles from their background, were particles appear white and background appears black. Three different grey-scale thresholding levels were applied to the same image (Figures 3.11b – d), although application of a simple threshold alone does not allow the discrimination of different floc components. The three thresholds applied identify different numbers of particles and occupied pixel areas from the same image (see Figure 3.11g). To confirm particle identity, the semi-automated software TWS (see § 2.4) (Schindelin *et al.*, 2012; 2015; Arganda-Carreras, 2015) for recognising shapes and grey-scale value were used to separate objects. In TWS a small number of images are annotated and used to train the classifier which can then be applied to the larger image stack. This process is illustrated in Figure 3.11e where the separate particles are manually recognised and identified. The result of applying this algorithm is demonstrated in Figure 3.11f, showing the particles visible in the SE image

Figure 3.11a have been correctly identified. The process can then be verified by comparing the results with adjacent slices before the classifier is applied to the whole image stack. It is necessary to verify that the different shapes have been recognised correctly by examining the result in 3D. The results shown in Figure 3.11 demonstrate the highly irregular 3D shape of primary particles found within flocs, the geometries of which would be impossible to reconstruct from 2D images alone. The identification process may be iterated to ensure optimal identification of particle.

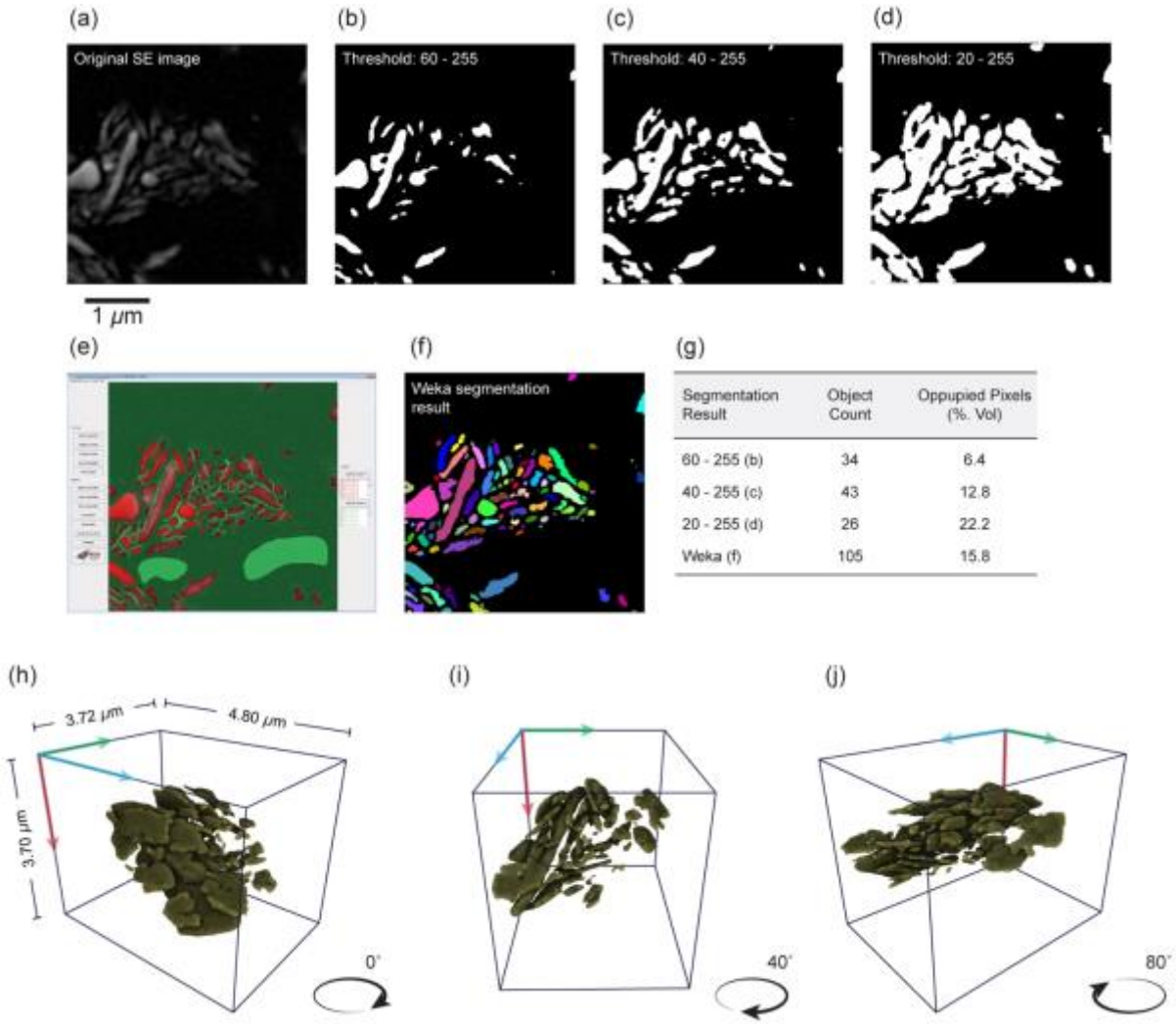

Segmentation Result	Object Count	Oppupied Pixels (%. Vol)
60 - 255 (b)	34	6.4
40 - 255 (c)	43	12.8
20 - 255 (d)	26	22.2
Weka (f)	105	15.8

Figure 3.11. Feature recognition in SEM images in 2D and 3D; (a) Original SE image (pixel size 24 nm^2); (b – d) Binary masks achieved by histogram based thresholding; (e) Screenshot of the Trainable Weka Segmentation Tool v2.1.0 (Arganda-Carreras, 2015) window showing semi-automated segmentation procedure; (f) Binary mask achieved using the Trainable Weka Segmentation Tool; (g) Table showing the number of objects counted and the %. Vol. of occupied pixels for the different threshold values (b – d) and Weka segmentation (f); (h – j) 3D reconstruction of the clay particle-particle association identified in sub-volume S3.1-1 showing 3 different orientations.

When this procedure is applied to the same data but in 3D, the resulting 3D image, a sub-volume identified in Figures 3.11h – j, is recognisable as a set of clay platelets spatially arranged to form a multi-particle unit approximately 5 μm in diameter. Rotating the image data confirms that the particles have a plate-like morphology and are clearly separated. Hence, a combination of grey-scale and 3D shape are required for feature classification. The apparently empty space between particles may be filled or partially filled with EPS but cannot be resolved due to the resolution limitation of the FIB-nt. Other floc components (e.g., bacteria) can be identified by further combinations of grey-scale thresholding and shape analysis.

Image stacks obtained from FIB-nt provide the opportunity to compare metrics generated from 3D data volumes to those extrapolated from 2D imagery. Figure 3.12 shows a sub-volume (S5.2-2) taken from the dense region of clay particles in the dataset presented in Figures 3.15a and e (position not shown), the constituents of which have been segmented

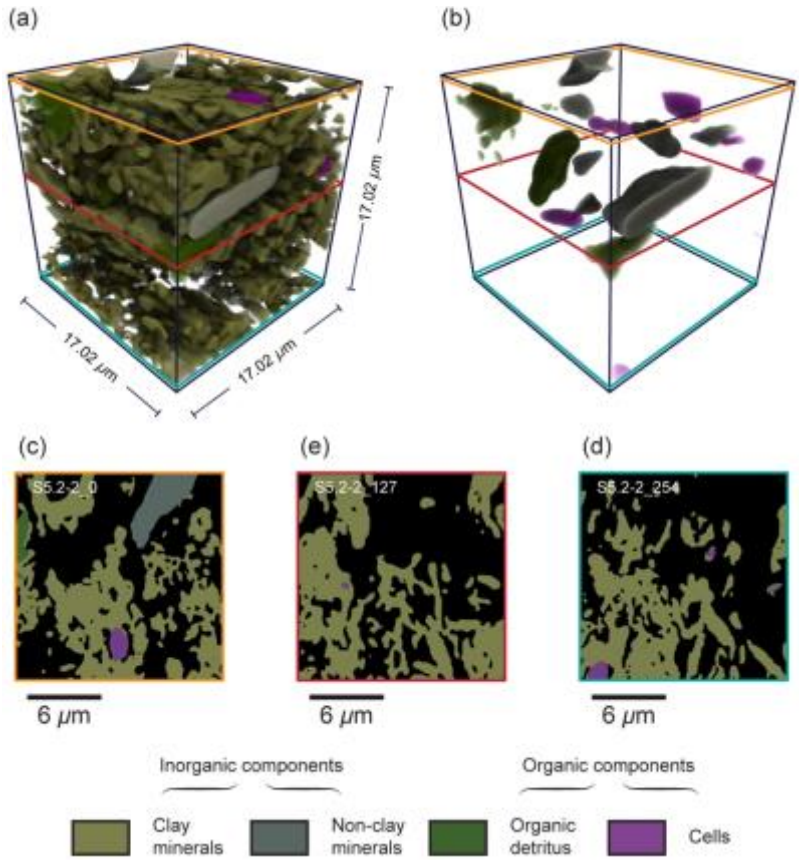

Figure 3.12. Sub-volume of the FIB-nt volume shown in Figure 3.15a (labelled S5.2-2); (a) Reconstructed volume containing clays, non-clay minerals, organic detritus and microbial cells; (b) Same as (a) but with the clay matrix rendered transparent; (c – d) 2D cross-sections taken from the sub-volume the positions of which are shown by border colour in (a).

Sample	Total Size of Sub Volume (μm^3)	Total Occupied Volume (%)	Total-Porosity (Vol. %)	Clay Minerals (Vol. %)	Non-Clay Min. (Vol. %)	Organic Material (Vol. %)	Bacteria (Count)
S5.2-2	~6.16×10^2	36.38	63.62	33.94	1.75	4.25	8
S5.2-2_0	~7.24×10^1	47.73	52.27	39.35	5.42	2.95	1
S5.2-2_127	~7.24×10^1	42.57	57.43	42.49	0	0.09	1
S5.2-2_254	~7.24×10^1	35.42	64.58	34.32	0.23	0.87	2
	Range	12.31	12.31	8.17	5.42	2.86	1

Figure 3.2. Volume fractions for the segmented components of the sub-volume (S5.2-2; shown in Figure 3.15a) of S5.2.

based on their grey-scale value and morphology for quantitative characterisation. Measurements obtained from three 2D cross-sections (Figures 3.12c – d) are shown in Table 3.2 alongside those obtained from the original 3D volume from which the slices were selected. Results varied considerably between the three 2D cross-sections, with measures for the occupied volume varying by ~12%. Compared with the actual value derived from the 3D data volume, values obtained from 2D cross-sections overestimated occupied volume of ~11%. This overestimation of total occupied volume was associated with an underestimation of total porosity (~11%). Significantly, the 2D cross-sections performed poorly when attempting to measure small, isolate structural entities that were irregularly distributed within the volume (i.e. non-clay mineral grains, organic material and bacterial cells). Extrapolating the number of discrete features (e.g., bacteria) from a 2D plane to a 3D volume would require consideration of the item geometry, and assumptions of the regularity of their distribution throughout the volume.

For the purpose of demonstrating the different features that can be recognised in 3D using the primary imaging modes of the SEM, two separate FIB-nt volumes were collected from floc sample S3. Figures 3.13a and e show 3D reconstructions of these two test datasets, S3.1 and S3.5, which were generated using SEs and BSEs respectively. Each data volume consisted of between 470 – 600 images, and as the slice thickness was the same magnitude as the pixel resolution of these images (between 22 – 24 nm^2) an isotropic (cubic) voxel size was obtained (Bushby *et al.*, 2012).

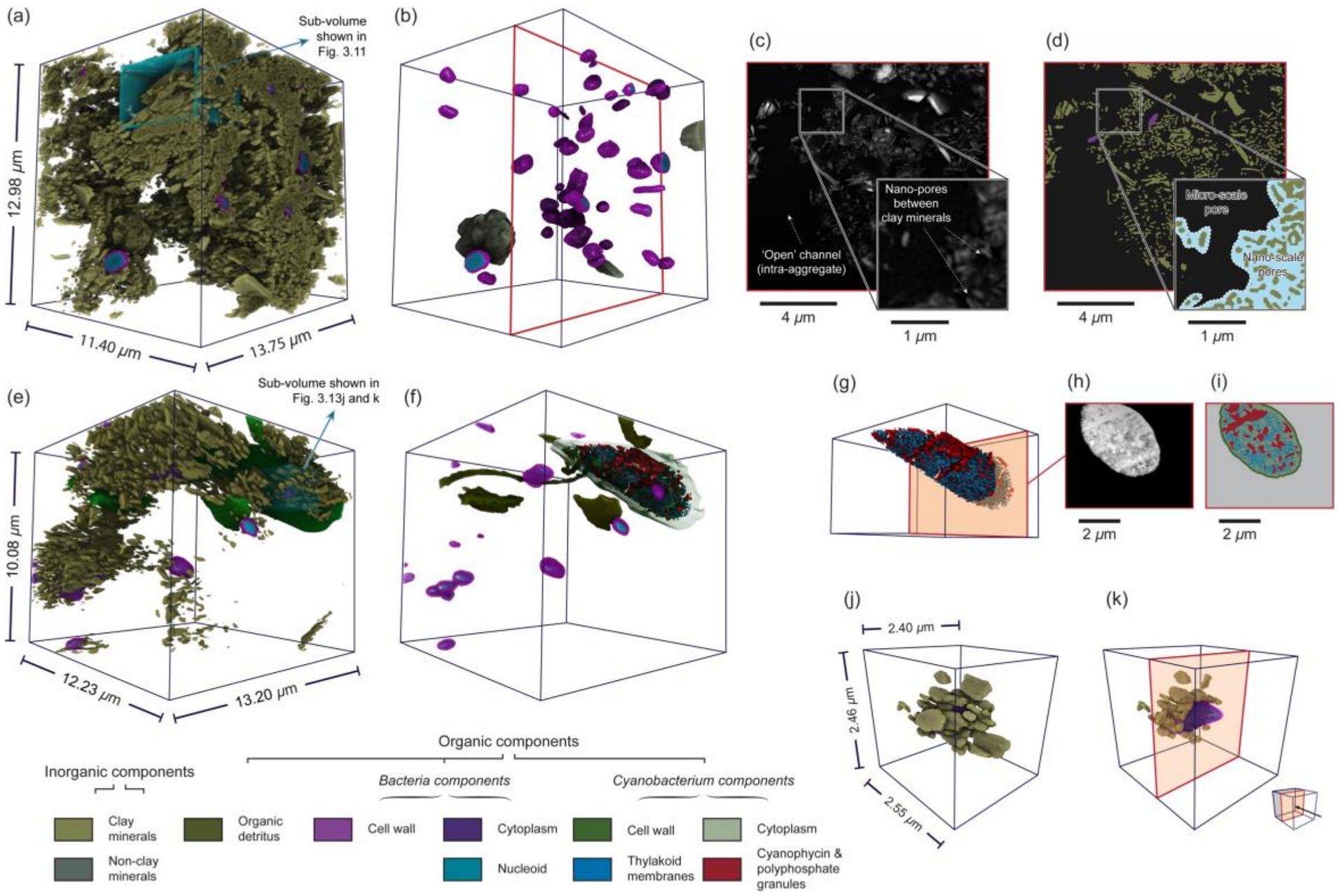

Figure 3.13. 3D reconstructions of FIB-nt volume S3.1 and S3.5 based on SE and BSE images respectively: (a) Segmented components identified within volume S3.1 and the location of the magnified sub-volume depicted in Figure 3.11; (b) Same as (a) but with clay minerals rendered transparent to reveal the bacteria and non-clay minerals; (c) Selected SE image from the original image stack (location within S3.1 indicated by red line shown in (b)) showing larger micro-scale 'channels' and nano-scale pore space; (d) Binary mask of (c) generated by semi-automated Weka segmentation; (e) Segmented components identified within S3.5 and the location of the sub-volume shown in (j) and (k); (f) Same as (e) but clay minerals rendered transparent to reveal organic components; (g) Isolated cyanobacterium with cell wall rendered transparent; (h) Selected BSE image from original image stack (location with S3.5 identified in (g)) showing the ultrastructure of the cyanobacterium; (i) Segmented subcomponents of the cyanobacterial cell; (j) Sub-volume selected from S3.5 showing an individual micro-floc (location of sub-volume shown in S3.5 shown in (e)); (k) Same as (j) but clay minerals have been trimmed back to reveal a bacterium at the centre of the micro-floc in the process of division. Pixel dimension of original image stacks: 1,024 x 884; voxel size of S3.1 and S3.5: 24 and 22 nm respectively.

Sample	Total Size of Analysed Volume (μm^3)	Micro-Porosity (Vol. %)	Nano-Porosity (Vol. %)	Clay Minerals (Vol. %)	Non-Clay Min. (Vol. %)	Organic Detritus (Vol. %)	Bacteria (Vol. %)	Bacteria (Count)
S3.1	~2.0×10^3	65.8	21.4	11.8	0.7	-	0.3	48
S3.5	~1.6×10^3	86.0	7.5	2.3	-	0.2	4.0	18

Table 3.3. Volume fractions for the segmented components of FIB-nt datasets S3.1 and S3.5.

Semi-automated segmentation of the 3D datasets as described previously enabled the recognition of five basic floc constituents: i) pore space, ii) clay minerals, iii) non-clay minerals, iv) microbial cells and v) organic detritus. Pore-space was defined as structureless regions of the datasets exhibiting low, homogenous grey level values. Within both data volumes clay minerals were readily identified based on their 3D planar morphology and their mid-range grey-scale value. Whilst the isolation of individual clay minerals was less effective in images captured using BSEs (S3.5) the enhanced spatial resolution provided by SEs (S3.1) enabled their segmentation. Bacteria were primarily identified based on their 3D rod- and sphere-like morphologies, in addition to their high grey level values compared to background clay and pore-space (for BSE images – S3.5). Additionally, contrast provided by the BSE images (S3.5) permitted the identification of differentially stained sub-cellular structures. This is illustrated in Figures 3.13g – i in which the ultrastructural detail within a cyanobacterial cell (identified based on bright grey-scale values, size and filamentous morphology in 3D) can be resolved. Irregularly shaped objects with high grey level values were considered to be organic detritus. Non-clay minerals were differentiated based on their distinct blocky/irregular morphology and in some cases uniform grey-scale value. However, the grey-scale contrast between non-clay minerals and the clay mineral matrix within both datasets was often insufficient to facilitate complete segmentation. Manual segmentation of non-clay minerals was therefore conducted where necessary and involved classifying the pixels within an image and comparing the results with adjacent images. The resulting binary masks generated by the segmentation procedure formed the basis for subsequent 3D visualisations (Figures 3.13a and e) and quantitative analysis (Table 3.3).

Within the 3D datasets inter-aggregate pores can be easily identified together with smaller elongated intra-aggregate nano-pores along the boundaries of clay particles (Figures 3.13c and d and Table 3.3). Combined, these give a total porosity of 87.2 (S3.1) and 93.5 (S3.5) vol. %. The occupied volume of S3.1 is composed largely of inorganic material, with

clay platelets accounting for ~92 % of the occupied space. Non-clay minerals are distinguishable and account for a further ~5 % of the occupied volume. Clay platelets are arranged in close association with each other, which produces a large surface area to volume ratio and accounts for the higher nano-porosity values observed in S3.1 compared to S3.5. In contrast, the dominant feature of S3.1 is a single cyanobacterium occupying nearly 60 % of the occupied space. The inorganic fraction is comparatively smaller (~36 %), comprising clustered clay platelets in loose association with the cyanobacterium and organic debris. Investigation of the 3D datasets revealed units of clay minerals to be arranged into associations with either face-to-face or edge-to-face contacts, similar to those identified in 2D TEM and STEM images (see § 3.2.2). An example of one of these units is shown in Figures 3.11h – j. Other types of primary particle associations included units of clay platelets arranged around bacteria or larger non-clay minerals (Figures 3.13j and k).

Figures 3.14 and 3.15 show 3D reconstructions of the two FIB-nt volumes (S5.1 and S5.2) collected from floc sample S5, the locations of which are given in Figure 3.8d. S5.1 was position in order to analyse a relatively dense region of the floc, whilst S5.2 was located to capture what was identified within the 2D SEM-BSE montage taken from the surface of floc S5 as a microfloc (as defined in § 3.2.2 and Figure 3.6). Both data volumes consisted of between 600 – 950 images which were generated using BSEs. S5.1 was acquired with a high voxel resolution (15 nm), and consequently the analysis was based on a relatively small data volume (~4.8×10^3 μm^3). In comparison, S5.2 encompassed a larger volume (~7.6×10^4 μm^3) and had a significantly lower voxel resolution (67 nm).

The five main constituents identified in the test datasets S3.1 and S3.5 (pore space, clay minerals, non-clay minerals, microbial cells and organic detritus) were also identifiable in S5.1 and S5.2. Table 3.4 shows the quantitative results obtained from volume S5.2. Closer scrutiny of the data volumes allowed the differentiation of sub-categories of materials.

Sample	Total Size of Analysed Volume (μm^3)	Micro-Porosity (Vol. %)	Nano-Porosity (Vol. %)	Clay Minerals (Vol. %)	Non-Clay Min. (Vol. %)	Organic Detritus (Vol. %)	Organo-mineral debris (Vol. %)	Bacteria (Vol. %)	Bacteria (Count)
S5.2	~ 7.7×10^4	91.4	3.80	4.08	0.41	0.23	0.01	0.07	239

Table 3.4. Volume fractions for the segmented components of FIB-nt volume S5.2.

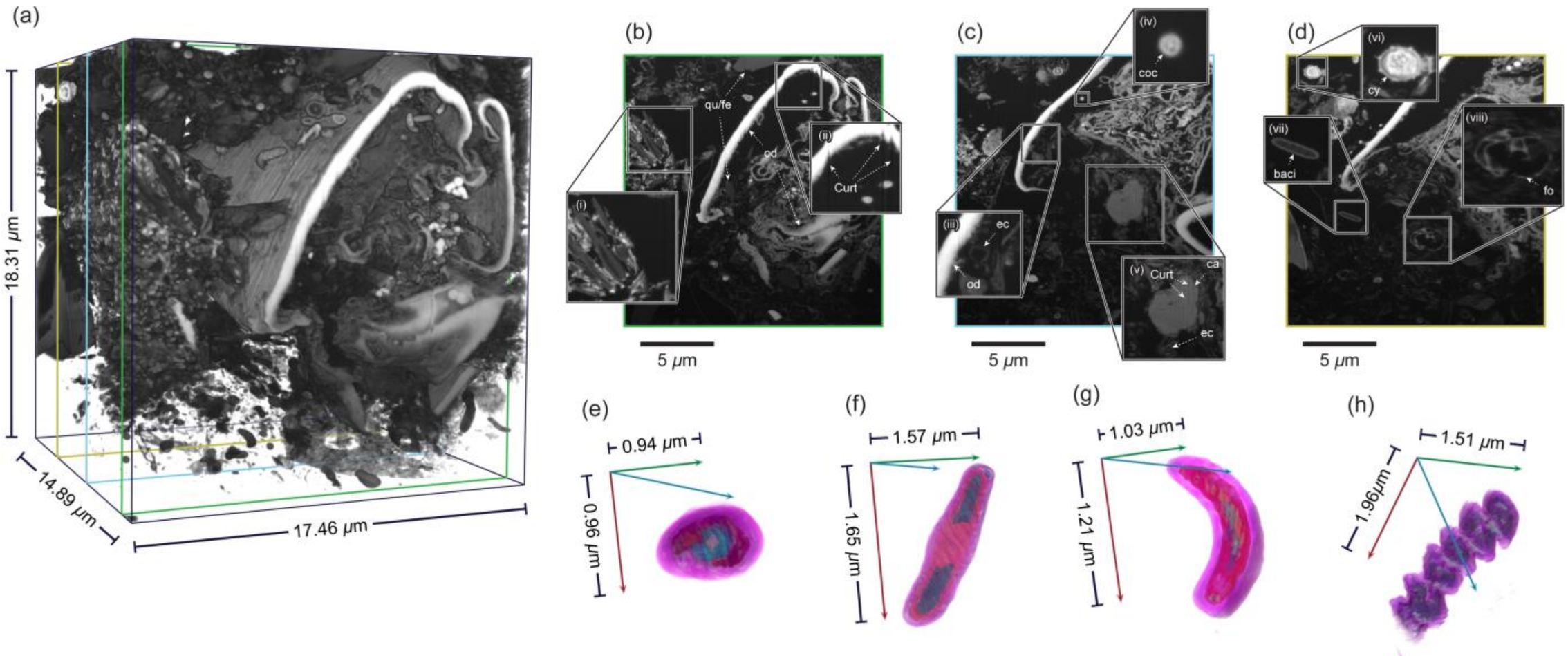

Figure 3.14. 3D reconstruction of FIB-nt volume S5.2 based on BSE images generated in the 3D viewer in Fiji/ImageJ: (a) Grey-scale reconstruction of S5.1 in which material(s) with grey level values <2 (i.e. resin) have been rendered transparent; organic materials exhibit high grey-scale values due to staining, whilst darker objects are mostly inorganic minerals; (b – d) Selected BSE images from the original image stack (locations within S5.1 indicated by coloured lines shown in (a)); (e – h) Examples of different bacterial cellular morphologies including, (e) cocci, (f) bacilli, (g) vibrio and (h) spirillum; (i – viii) sub-sets taken from BSE images shown in (b – d). Pixel dimension of S5.1 image stack: 2,048 x 1,768; voxel size: 15 nm. ca, carbonate mineral; cy, cyanobacterium; curt, curtaining artefacts; ec, empty cell (moribund or dead); fe, feldspar; fo, foraminifera; od, organic detritus; pro, prokaryote cell (bacterium); qu, quartz

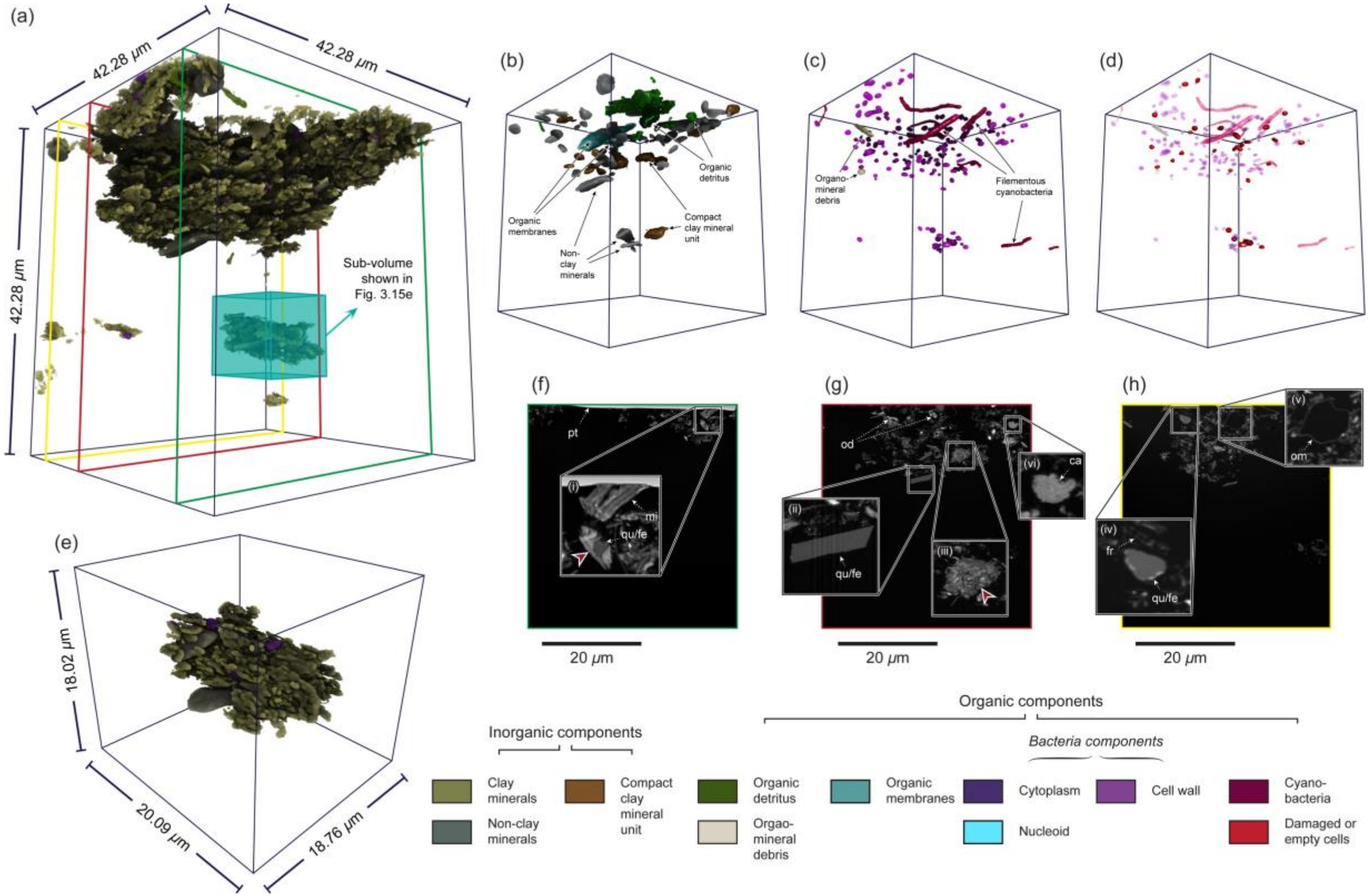

Figure 3.15. 3D reconstructions of FIB-nt volume S5.2 based on BSE images generated in Drishti: (a) Segmented components identified within volume S5.2 and the location of the magnified sub-volume depicted in (e); (b) Same as (a) but with certain materials rendered transparent to reveal the non-clay minerals, organic membranes and amorphous organic detritus; (c) Same as (a) but with certain materials rendered transparent to reveal the individual bacteria, cyanobacteria and organomineral debris (diatom frustules); (d) Same as (c) but with intact bacteria, cyanobacteria and organomineral debris (diatom frustules) render translucent in order to highlight damaged and empty bacterial cells which are false coloured red; (e)) Sub-volume selected from S5.2 showing an isolated microfloc; (f – h) Selected BSE images from the original image stack (locations within S5.2 indicated by coloured lines shown in (a)); (i – v) Sub-sets from BSE images shown in (f), (g) and (h). Pixel dimension of S5.2 image stack: 1,024 x 884; voxel size: 67 nm. ca, carbonate; fe, feldspar; fr, frustule; mi, mica grain; od, organic detritus; om, organic membrane; pc, plant cell; qu, quartz; sd.

Microbial cells were classified based on their morphotype, with examples of the five main cell morphologies being present in the FIB-nt volumes. Cocci were characterised by their spherical shape and ranged in diameter from 0.5 to 1.5 μm (Figure 3.14e). Unlike other cell types which were usually observed as solitary cells, cocci in a number of instances were observed in small groups consisting of 4 – 6 individuals. Bacilli were rod-shaped bacteria the long axis of which measured 1.5 – 2 μm in length (Figure 3.14f). Cells with a comma-shape morphology were identified as vibrio, and usually had similar dimensions to bacilli (Figure 3.14g). Spirilla or spiral bacteria had a distinctive corkscrew-shape (Figure 3.14h), and although present in both volumes, were comparatively rare. Filamentous cyanobacteria bacteria were also present in a number of forms, and ranged from large cyanobacterial cells up to 5 μm in diameter (Figure 3.14d:vi) to several smaller varieties with diameters of between 1 to 2 μm (Figure 3.15c).

A total of 110 and 239 individual cells were identified in volumes S5.1 and S5.2 respectively. The dimensions of the segmented bacteria present in S5.1 were measured allowing the relative frequency of occurrence of 'rod' (bacilli, vibrio, and spirilla) and 'sphere' (cocci) shaped bacteria to be quantified. Cells with a ratio of at least 2:1 were classified as rods, whilst those with a ratio of >2:1 were categorised as spheroid. Of the cells recognised in S5.1, 28.5% were classified as being spheroid in shape whilst 71.5% were rod-like. In addition to being able to quantify cell morphotype, the metabolic state of microbial cells could be inferred from an analysis of their structural integrity. This was achieved by extending the method defined by Heissenberger *et al.* (1996a) for characterising the metabolic state of bacteria in 2D images (described in § 3.2.2) into 3D. The high voxel resolution of S5.1 (15 nm^3) ensured that the fine detail of individual microbial cells could be distinguished, and in certain instances the flagella of bacteria were visible. Of the total number of cells identified in S5.1, 76.4% were recognised as being intact whilst 10% and 13.6% were categorised as being damaged and empty respectively. Unlike S5.1, the coarser voxel resolution of S5.2 (67 nm^3) prevented the internal cellular detail of bacteria from being resolved, reducing the level of confidence with which cells could be classified. Microbial cells exhibiting a high, homogenous grey-scale value were interrupted as being intact and accounted for 73.2% of the cells present within the data volume. Damaged and empty cells could not be differentiated, and were consequently grouped together. The total number of cells identified as being either damaged or empty amounted to 26.8%.

Volume S5.1 contained a significant quantity of organic material, and was largely dominated by a single organic structure (Figures 3.14a – d). This structure was previously identified in both the SEM-BSE and dark-field STEM image montages taken from the surface of floc S5, as shown in Figures 3.6a and 3.8d respectively. Common to both volumes was the presence of organic membranes, fine sheaths of material that were often curled or coiled into irregular tube-like structures (Figure 3.15b). These could only be recognised in 3D. When bisected crosswise membranes present the appearance of an irregular 'blob' with a definable bright edge and a featureless, resin-filled interior (Figure 3.15h:v). The remains of marine plankton (e.g., foram tests; Figure 3.15:viii) were also found to be present in both data volumes.

The lower resolution of S5.2 had the most noticeable impact when trying to segment clay minerals. This is demonstrated Figures 3.15f – h which show the voxel resolution was insufficient to separate individual clay platelets from their close neighbours, particularly where clays formed closely packed units (e.g., Figure 3.15g:iii). In comparison, visual inspection of the image slices taken from S5.1 (Figures 3.14b – d) show that the void space between clay platelets were often represented by several voxels, making precise object recognition feasible. Due to their larger size (diameter, >5 μm), distinctive morphology and grey-scale value non-clay mineral grains in both volumes could be recognised with a high level of precision. Distinction could be made between different types of particles following the same criteria as described for TEM and STEM (§ 3.2.2). Viewed in 3D, carbonate minerals were found to contain intragranular porosity, exhibiting circular to elongate pore spaces that were often isolated from the exterior pore network of the floc (Figures 3.14c:v and 3.15g:vi). In a number of instances bacteria were observed occupying the recesses of large non-clay mineral grains.

The structural information obtainable from S5.1 and S5.2 varied considerably. To an extent, this is due to the location of the datasets within the floc (see Figure 3.8d), but also volume size and resolution. While S5.1 offered few new insights into the organisation of primary particles, containing particle and structural associations similar to those described in the test datasets (S3.1 and S3.5), the wider field of view achieved with S5.2 provided further information regarding the organisation of larger structures (e.g., microflocs identified in 2D STEM and SEM montages; § 3.2.2 and 3.3.2). Figures 3.15f:i and g:iii show units of compact clay minerals (described previously in 2D in § 3.3.2) alongside the primary clay associations: clay minerals aligned face-to-face and/or edge-to-face and bacteria surrounded by clay

platelets. These units were organised into larger microflocs that could be defined from one another based on inter-aggregate pore space. An example of an isolated microfloc is given in Figure 3.15e. Filamentous bacteria were observed to extend through the volume, and were often associated with several microflocs.

3.3.4. Summary

An initial comparison of the primary imaging modalities of the SEM (SE and BSE) showed that while BSE had a lower spatial resolution, its ability to provide compositional information made it more suitable for the investigation of complex flocculated material. Micrometre data volumes obtained from flocs S4 and S5 corroborate compositional and structural information obtained at the nanometre-scale by TEM-EDS and STEM (§ 3.2). However, the 3-dimensionality of these datasets provided a significantly better understanding of the true geometry of floc constituents and particle and structural associations.

3.4. 3D X-ray μCT Dataset Obtained at the Millimetre-Scale

3.4.1. Introduction

This section describes the output of duplicate μCT scans of floc samples S4 and S5. Scans conducted prior to trimming and sectioning of the blocks (S4-Pre and S5-Pre) were used to characterise the millimetre-scale properties of the flocs, whilst those conducted post-sectioning (S4-Post and S5-Post) provided the location of the block-face created during the sectioning procedure upon co-registration (see § 3.5).

3.4.2. 3D X-ray μCT

The output of the individual μCT scans were image stacks consisting of 1,022 – 1,024 images with pixel resolutions of 10.066 μm^2 that mapped the variation of X-ray attenuation through the sample blocks. The scan parameters for all X-ray datasets were kept the same (Table 3.5), making their grey-scale values directly comparable. Contrast within the μCT images was sufficient to identify different structural features based on shape and grey-scale value, and for both samples flocculated material could be readily distinguished from the surrounding resin and metal registration pins. This is demonstrated in Figure 3.16 which shows slices taken

Sample		Label	Scan Parameters					
			Filter (mm)	Voltage (kV)	Current (μA)	Exposure (ms)	Gain (dB)	Voxel Size (μm)
S4	Pre-microtoming	S4-Pre	1 (Cu)	150	160	2829	12	10.066
	Post-microtoming	S4-Post	1 (Cu)	150	160	2829	12	10.066
S5	Pre-microtoming	S5-Pre	1 (Cu)	150	160	2829	12	10.066
	Post-microtoming	S5-Post	1 (Cu)	150	160	2829	12	10.066

Table 3.5. Scanning parameters selected for the acquisition of X-ray datasets. Floc samples were scanned in duplicate, once before sectioning and once after to allow the working surface within the original volume to be located during co-registration.

from the X-ray datasets S4-Pre and S5-Pre alongside 3D reconstructions of the floc samples. Flocculated material is shown to have mid-range grey-scale values, whilst resin is defined as structureless regions exhibiting low, homogenous grey level values. In comparison, the metal registration pins exhibited high grey-scale values (between ~250 – 255, Figures 3.16e and f) and could be further identified by their distinctive shape (U-shape in Figures 3.17 and 3.18).

The resolution of μCT makes the identification of individual floc constituents impossible and grey-scale values are an average of the attenuation properties of the different materials contain within each pixel (partial volume effect). Inspection of the image slices shows that the grey-scale values of both flocs vary, with regions of high and low X-ray attenuation being recognisable. These variations in grey level values are likely to reflect the differences in the concentration of floc constituents and subsequently sub-voxel porosity and/or the X-ray attenuation values of certain materials (e.g., large inorganic particles or heavy metal stained organic structures) (see § 3.5.2). 3D renderings of the flocs in which the regions of low attenuation are rendered semi-transparent show that the regions of high X-ray attenuation are distributed randomly within the flocs (Figures 3.16c and g).

3D visualisations shown in Figures 3.16b and f demonstrate the flocs to be relatively long and thin, and based on their size and elongated shape (h/w>2) both can be classified as stringer-type macroflocs. Whilst S4 and S5 differ in size, being ~1.5 and ~4.6 mm respectively, their morphologies are relatively similar. Both flocs appear to be highly contorted and twisted, with their peripheries folded in towards their central axis. Additionally, inspection of the flocs in 3D show that they consist of several smaller units –

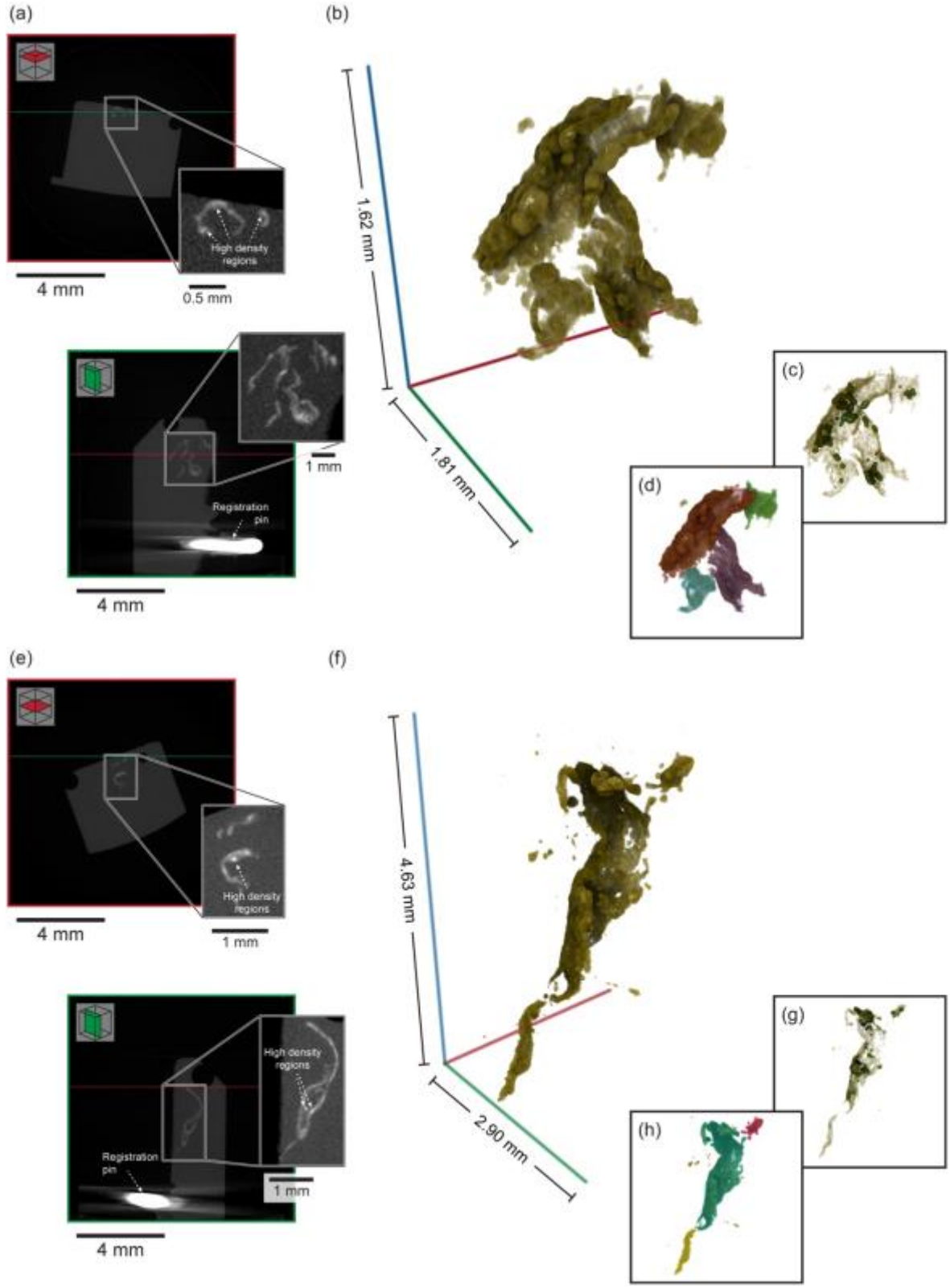

Figure 3.16. 3D visualisations of the floc samples S4 (b) and S5 (f); (a) and (e) Images slices taken in two orthogonal planes from S4-Pre and S5-Pre respectively. Note the regions of high and low X-ray attenuation within the floc; (c) and (g) Same as (b) and (f) but with the regions of low X-ray attenuation rendered semi-transparent to reveal the pockets of high attenuation; (d) and (h) Same as (b) and (f) but with sub-flocs colour coded.

termed here as 'sub-flocs' – which range in size from 0.5 to 2 mm in diameter (Figures 3.16d and i). This is particularly evident in the case of floc S4 that seems to consist of four distinct structures, some of which appear to be disconnected from the main body of the floc. However, it is conceivable that fine detail such as small bridging structures has been lost due to the insufficient resolution of the X-ray datasets.

Using the 3D Object Counter plugin available in Fiji/ImageJ (Bolte & Cordelières, 2006), the total volume of the flocs was determined to be 2.89×10^8 and 5.79×10^8 μm^3 respectively. These values include the apparently disconnected sub-flocs.

3.4.3. Summary

Low-resolution X-ray CT datasets demonstrate the complex external morphology of the floc samples, and provide some insights regarding their internal structure. Variations in X-ray attenuation were observed, and are likely to correspond to regions within the flocs that have a higher density of material. Both flocs were observed to be composed of smaller 'sub-flocs' connected by narrow bridges of material.

3.5. Description of the Co-Registered Datasets

3.5.1. Introduction

To co-visualise the multi-modal, multi-scale datasets described above (§ 3.2 – 3.4), stack-to-stack registration of the datasets was conducted. In the following section the proficiency with which the datasets were aligned is described, in addition to misalignment errors which are quantified where possible.

3.5.2. 2D and 3D Correlated Datasets

For the co-registration of the 2D and 3D datasets both manual and automated alignment techniques were applied in the 3D visualisation software Avizo®. Registration relied upon the identification of corresponding landmark features in the different datasets. Figures 3.17 and 3.18 show the correlative work-flow and sequence of steps taken to register datasets obtained from flocs S4 and S5 respectively. Low-resolution X-ray μCT scans of the flocs conducted prior to ultramicrotomy (S4-Pre and S5-Pre) acted as 'parent' datasets to which all other

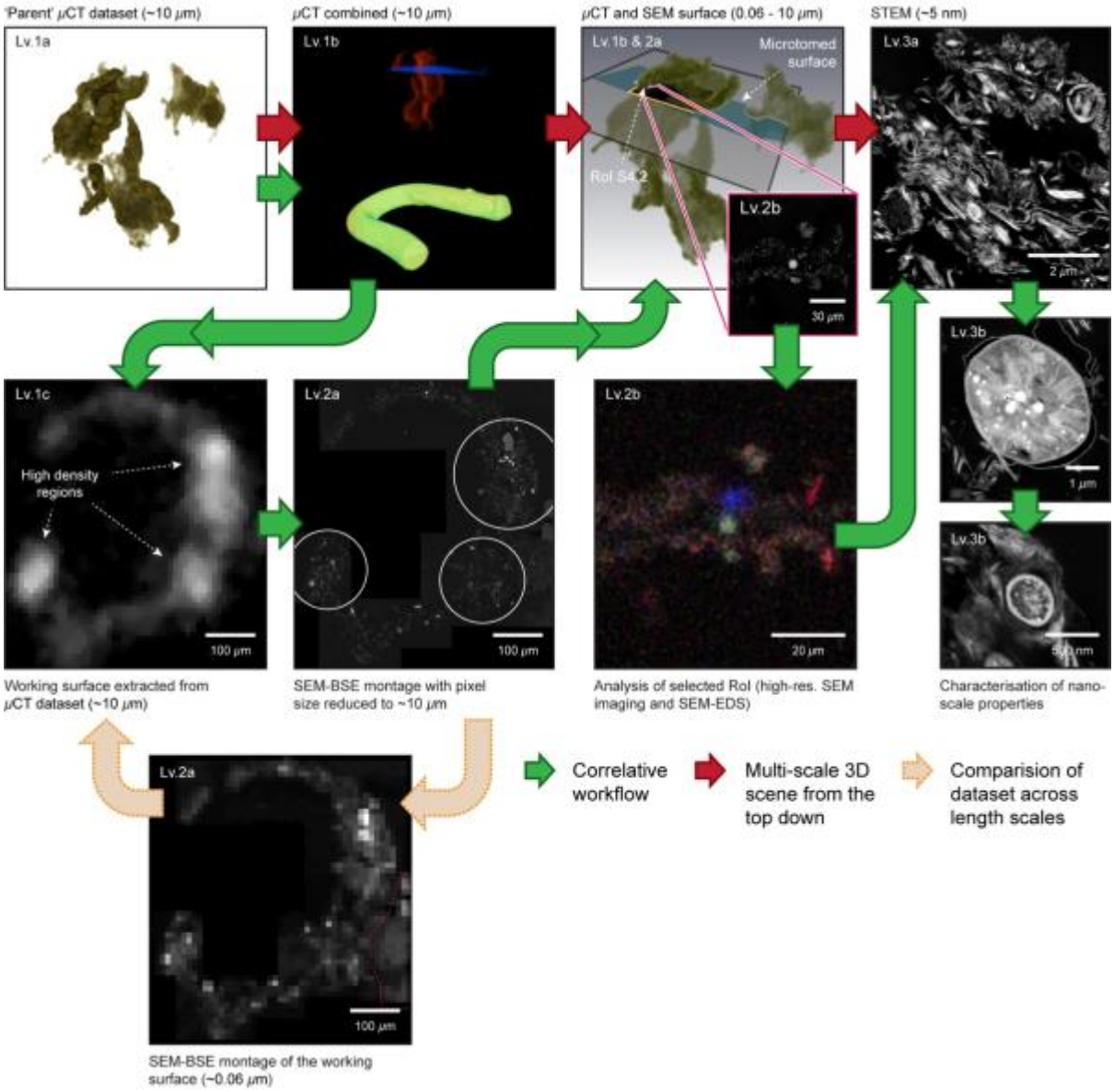

Figure 3.17. Visualisation of the correlative datasets obtained from floc sample S4. Registration of the μCT datasets relied upon the use of the metal pins inserted into the resin post polymerization, whilst aligning the SEM-BSE image montage required downscaling the pixel resolution of the voxel montage to match the voxel resolution of the CT scan (~10 μm) (Lv.1c and 2a). Downscaling also provided a means of validating the potential floc structures responsible for different the grey-scale values observed in the CT scans. Note that dense areas of the floc identified in SEM-BSE montages (denoted by circles) correspond to areas exhibiting high X-ray attenuating values.

information would be aligned. Orientation of the X-ray datasets obtained post-sectioning of the sample blocks (S4-Post and S5-Post) was achieved using the registration pins added to the sample blocks post polymerization. Course alignment was initially conducted by hand using the *Transform Editor*. Subsequently, fine registration of the datasets was performed using the *Landmark Surface Warp* module, which applied a rigid transformation algorithm

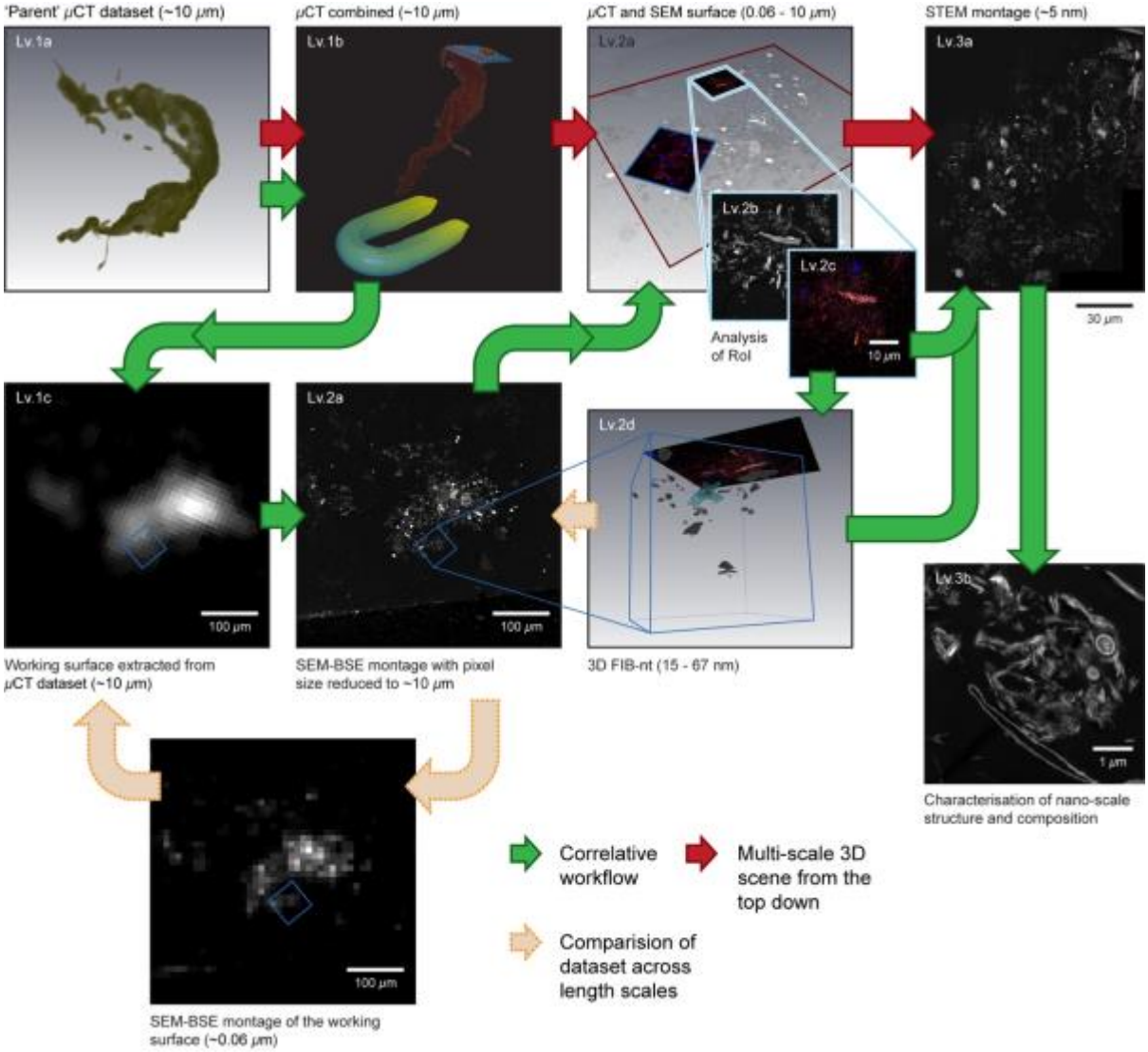

Figure 3.18. Visualisation of the correlative datasets obtained from floc sample S5. Registration of the μCT datasets relied upon the use of the metal pins inserted into the resin post polymerization, whilst aligning the SEM-BSE image montage required downscaling the pixel resolution of the voxel montage to match the voxel resolution of the CT scan (~10 μm) (Lv.1c and 2a). The location of FIB-nt data volume S5.2 (shown in Lv.2d) is indicated on the working surface by a blue box. Registration of the FIB-nt datasets was achieved by comparing SEM images taken prior to serial section with the BSE montage.

(consisting of both translation and rotation of one dataset into another). For accurate registration features used as landmarks should be represented by the same number of voxels. This is dependent on the segmentation results, which may vary between datasets depending on the image quality, resolution and orientation of the sample relative to the pixel grid. Table 3.6 shows that slight discrepancies in the total number of voxels contained within the metal pins which amounted to 1.6% for sample S4 and 3.8% for S5. Visual inspection of the

Sample		Vol. (μm^3)	No. of Object Voxels	% Vol. Difference (Post - Pre)
S4	Pre	2.88×10^9	2.82×10^6	1.6
	Post	2.92×10^9	2.87×10^6	
S5	Pre	3.66×10^9	3.59×10^6	3.8
	Post	3.80×10^9	3.72×10^6	

Table 3.6. Difference in the segmentation results for the the metal pins used for registration.

aligned μCT scans showed peripheral misalignment in some features, but generally good agreement was observed for the registered flocs.

Once the μCT data volumes were aligned, 2D SEM-BSE image montages were added and oriented based on the trapezoid shape of the working surface. Following the initial alignment of the datasets duplicates of the SEM-BSEM montages were created and their resolution downscaled to match that of the X-ray μCT scans (~10 μm). This enabled an appraisal of the position of the floc boundary in the aligned datasets, and from visual inspection both datasets showed good agreement (Figures 3.17 and 3.18: Lv.1c and 2a). The same features can be recognised in both μCT and SEM-BSE images, even though the contrast mechanism is not exactly the same and resolution of the data sets is quite different.

3.5.3. Summary

It is demonstrated that the datasets generated by the different techniques used in this work can be correlated to extract morphological and compositional information at length-scales from nanometres to millimetres. This includes 2D and 3D data-sets as well as chemical analysis maps from EDS measurements, allowing constituents to be recognised and 3D structures of the floc to be characterised from primary particles to whole flocs.

Chapter Four: Discussion

4.1. Introduction

In this chapter, it is considered whether the results presented in Chapter 3 meet the objectives of the thesis stated in § 1.5. To this effect the results are discussed in 3 sections: Section 4.2 considers how well the embedded floc represents the aqueous material and whether the stabilisation and embedding process has influenced the data obtained; Section 4.3 considers each of the datasets individually in an attempt to establish what information can be obtained about the floc structure and chemistry at each of the spatial scales investigated; Section 4.4 considers the advantages of a multi-scale approach to floc characterisation; and finally, Section 4.5 summarises what new information has been obtained from this work leading to the conclusion of the thesis.

4.2. Critical Assessment of the Floc Stabilisation Technique

Accurate floc characterisation depends crucially on the ability to distinguish between features that are real and inherent to the floc, from those that are artefacts introduced during the capture and stabilisation procedure. Whilst measures can be taken to mitigate against floc perturbation some preservation artefacts are unavoidable (Leppard, 1992a; Buffle & Leppard, 1995b; Liss *et al*., 1996; Leppard *et al*., 1996). An ideal stabilisation procedure is one that successfully minimises these artefacts (Liss *et al*., 1996; Mavrocordatos *et al*., 2007). Evaluating the success of floc stabilisation, however, is hampered by the lack of *a priori* knowledge of natural floc structure prior to stabilisation. In the absence of such information, it is necessary to anticipate the potential effects that the different stages of the stabilisation procedure could have on fragile aqueous floc samples and compare those expected artefacts with what is seen in the image data (Leppard, 1992a; Leppard *et al*., 1996). These artefacts may manifest themselves at different length scales. With the ability to interrogate floc samples at multiple spatial scales and in 3D, the correlative datasets offer a large evidence base for evaluating the success of the stabilisation procedure.

Sampling may induce floc breakage and other morphological change (e.g., distortion) (Eisma *et al*., 1986; Droppo *et al*., 1996; Manning *et al*., 2010; 2011). For estuarine flocs like

S4 and S5 (herein described as macroflocs, see § 4.3) that typically have a high organic content (Dade *et al*., 1996; Manning *et al*., 2010; Furukawa *et al*., 2014), it is likely that their internal structure will not be altered by the relatively low shear forces created by pipettes used for sampling (Gibbs & Konwar, 1982; Droppo *et al*., 1996). The use of pipettes, however, can cause breakage and/or distortion of more delicate macroflocs (e.g., Manning & Dyer, 1999; Jarvis *et al*., 2005), and evidence for this is more likely to be found at the millimetre-scale. Volumetric renderings (from X-ray μCT) reveal the highly irregular 3D morphologies of macroflocs S4 and S5, which consist of smaller micro- and sub-flocs held together by narrow bridging structures (Figures 16a and f). Despite the fragility of these linkages, peripheral sub-flocs are still clearly connected with the main body of the floc. There are few examples of visible discontinuities. Given the areas of weakness described above, the tendency would be for macroflocs to evolve towards stability in the event of turbulent shear (Dyer & Manning, 1999; Manning & Dyer, 1999); i.e. disaggregation into smaller sub-flocs. The preservation of a high degree of irregularity is therefore evidence of minimal perturbation from the macrofloc's natural form. However, it must be acknowledged that the available imagery fails to inform on the properties of the macroflocs prior to their stabilisation, and that some symptoms of change are more difficult to diagnose as a result. This includes the physical deformation of floc samples by pseudo-plastic contortion (e.g., twisting) (Droppo *et al*., 1996), which cannot be ruled out completely. In any case floc structure is dynamic and the stabilisation process only captures one moment in time.

Within the image data collected from macroflocs S4 and S5 at the nano- and micrometre-scales various constituents can be recognised and are similar to those seen in previous TEM studies (Liss *et al*., 1996). 2D STEM images demonstrate that the stains used imparted sufficient contrast to organic structures to enable their distinction from inorganic materials (Figure 3.1). Similarly, organics can be identified in the 3D data volumes generated using FIB-nt (Figures 3.14 and 3.15). By far the most common artefacts cited as affecting organic material result from poor fixation (Hayat, 1981; Glauert, 1987; Bozzola & Russell, 1999). Of primary concern is the distortion and/or rupture of delicate cellular structures (Leppard, 1992a; Liss *et al*., 1996; Leppard *et al*., 1996). The intracellular integrity of bacterial cells can therefore be considered as a key indicator of the success of fixation. Based on the criteria outlined by Heissenberger *et al*. (1996a) (§ 3.2), 55.5% of the bacteria identified within the 2D STEM montage collected from floc S5 were classified as intact, whilst 44.5% were found to be either damaged or empty (see Figures 3.3 and 3.6). A slightly

higher proportion of bacteria were recognised as being intact within FIB-nt volumes S5.1 and S5.2, which on average contained ~74% bacteria that were intact and ~26% that were either damaged or empty (Figures 3.14 and 3.15). Intact bacteria can be considered as either metabolically active or dormant but viable, whilst damaged and empty cells are interpreted as moribund or dead (Heissenberger *et al*., 1996a). The presence of damaged or empty cells is not indicative of a failure in the fixation process since active microbial communities would be expected to contain cells of all states of life including decay (Leppard, 1992a; Leppard *et al*., 1997; Ward & Johnson, 1996; Leppard *et al*., 2003). Indeed, metabolically active bacteria usually only account for small percentage (<30%) of the total number of cells within a given community (Marxsen, 1988; Ward & Johnson, 1996). More diagnostic of the state of preservation is the presence of intact cells, as rupture due to stabilisation would be expected to be systemic if fixation was disruptive. The high proportion of intact cells within both the 2D STEM and 3D FIB-nt volumes suggests that fixation was successful, and was able to prevent the rupture and/or distortion of delicate organic structures during dehydration and subsequent resin embedding. Despite the success of fixation, organic constituents will have experienced volumetric changes that are likely to have amounted in net shrinkage (Hayat, 1981; Leppard *et al*., 1996; Bozzola & Russell, 1999). This is caused by the extraction of proteins and lipids during different stages of the stabilisation procedure (§ 2.2.2) (Hayat, 1981; Glauert, 1987). The amount of shrinkage experienced by organic material depends in part on the ability of the primary fixative (in this case glutaraldehyde/formaldehyde) to prevent dimensional alterations, but usually does not exceed 13% in cell biology (Hayat, 1981). The epoxy resin will also shrink during chemical curing and this is usually measured to be of the order of 5.5% (Zarrelli *et al*., 2002). In any case the shrinkage will not change the local arrangement of the constituents but may change their relative spacing compared to the native state.

Loosely associated organic colloids, including EPS fibrils, are susceptible to extraction during fluid exchanges (Leppard, 1992a; Liss *et al*., 1996; Leppard *et al*., 1996). High-resolution STEM imagery permits an assessment of these nanometre-scale particles, and shows the dense network of exopolymeric material within the matrix of the macroflocs S4 and S5, filling the nanometre pore space between larger particles (e.g., clay minerals and bacteria) (Figures 3.1a – b and 3.4). Within the inter-aggregate pores, however, EPS is notably absent (Figure 3.6). This pattern is consistent with loss due to extraction, as solvent fluid flow through the larger interconnected pore channels of flocs is likely to be more

efficient in removing EPS. If extraction is restricted to the inter-aggregate pores the effects on floc structure are relatively minor, resulting in an increase in the total pore space of the floc samples (e.g., Leppard *et al*., 1996) with the loss of loosely associated colloids. In comparison, the extraction of nano-pore EPS may result in severe perturbation of floc structure, since EPS fibrils represent the dominant bridging mechanism between floc constituents (Filella *et al*., 1993; Liss *et al*., 1996; Droppo, 2001; Burd & Jackson, 2009). Artefacts associated with the loss of these polymer bridges include the rearrangement of particle units and compression of particle-particle associations (recorded as shrinkage) (Leppard, 1992b; Leppard *et al*., 1996). Based on the comparative analysis of the effects of different stabilisation methods, including a 'benchmark' technique designed specifically to minimise EPS extraction (Mavrocordatos *et al*., 1994), previous studies have shown that under certain conditions 50 – 80% of matrix EPS can be removed following stabilisation (e.g., Liss *et al*., 1996; Leppard *et al*., 1996; 1998). Despite using a similar stabilisation method as the one described by Leppard *et al*. (1996), our results do not exhibit the same visual markers of excessive extraction such as the absence of both bound and soluble EPS. Additionally, FIB-nt datasets show little evidence of particle-to-particle compression (i.e. shrinkage; see below) (Figures 3.11h – j).

3D FIB-nt data volumes and 2D STEM images show particle associations and structural entities similar to those described elsewhere in the literature (see § 4.3). This would suggest the natural associations of macroflocs S4 and S5 remained relatively undisturbed. However, unlike organic floc constituents for which the effects of stabilisation can be assessed by examining their resulting properties (e.g., shape, structural integrity, etc.). An absolute check on the damage caused to the arrangement of clay minerals is difficult without conducting a comparative analysis of stabilisation techniques. Clay minerals are sensitive to physical and chemical changes in their immediate environment (e.g., changes in pH, ionic strength, etc.) (Leppard, 1992a; Mitchell & Soga, 2005; Partheniades, 2007), and the reagents used for fixation, staining and dehydration can easily perturb their delicate structure (Buffle & Leppard, 1995b). To an extent, damage can be moderated by adjusting the conditions of the buffer solution in which chemical reagents are delivered, to match that of the sample pore water (§ 2.2.2). Assuming this calibration is correct, the primary risk to clay structure is compression (recorded as matrix shrinkage) due to dehydration (Leppard, 1993; Liss *et al*., 1996; Leppard *et al*., 1996); i.e. the collapse of planar pore space between individual platelets. The known presence of EPS (Figures 3.1a – b and 3.4) provides some confidence

that clay structure has been preserved, as EPS fibrils act as a structural support network within the floc (Droppo, 2001).

Although some loss of EPS from within the floc pore space is likely to have occurred, there is minimal evidence of physical rupture or shrinkage of the floc, or damage to bacteria. Any damage that is observed is certainly no greater than that observed during the stabilisation of 2D samples, for example TEM analysis and therefore, this technique for the capture and stabilisation of flocs offers the potential to examine the 3D structure of these fragile materials for the first time.

4.3. Critical Evaluation of the Information Obtained at the Different Length-Scales

Improved model predictions of the transport and fate of sediment are reliant on the accuracy with which the physical properties of flocs can be measured. Currently, floc size and settling velocity are the most widely measured floc characteristic (Liss *et al*., 2005), with the classification of microflocs and macroflocs based on their diameter [e.g., macrofloc >~125 – 160 μm (Eisma, 1986; Manning, 2001)] being imposed relatively arbitrarily (Mikkelsen *et al*., 2006). Such classifications allow distinction between different groups within a floc population that may behave differently, and recognise that flocs are structured entities. However, this descriptive approach to floc structure classification is non-functional, i.e. it fails to consider the processes and mechanisms driving the development of particle associations which may vary spatially and temporally. The 3D data derived here enables a far more sophisticated classification of floc hierarchy, which is informed by the interactions and associations between different floc constituents and their spatial arrangements that can only be observed in 3D and at correlated length scales from nanometres to microns. Based on the results of the correlative datasets presented in Chapter 3, a new conceptual model is proposed that describes the most frequent structural associations observed within macroflocs S4 and S5 at different length-scales, as illustrated in (Figure 4.1). This model identifies five levels of organisation: Level 0 – *Primary particles*, Level 1 – *Primary associations*, Level 2 – *Microflocs*, Level 3 – *Sub-flocs* and Level 4 – *Macroflocs*.

High-resolution TEM and STEM imagery (resolution ~6 nm^2, area analysed 10 × 10 μm^2) in conjunction with STEM-EDS yielded detailed information regarding the composition of primary particles (Level 0). Materials could be characterised on a per particle basis, and macroflocs S4 and S5 were found to composed of a diverse range of materials consistent with

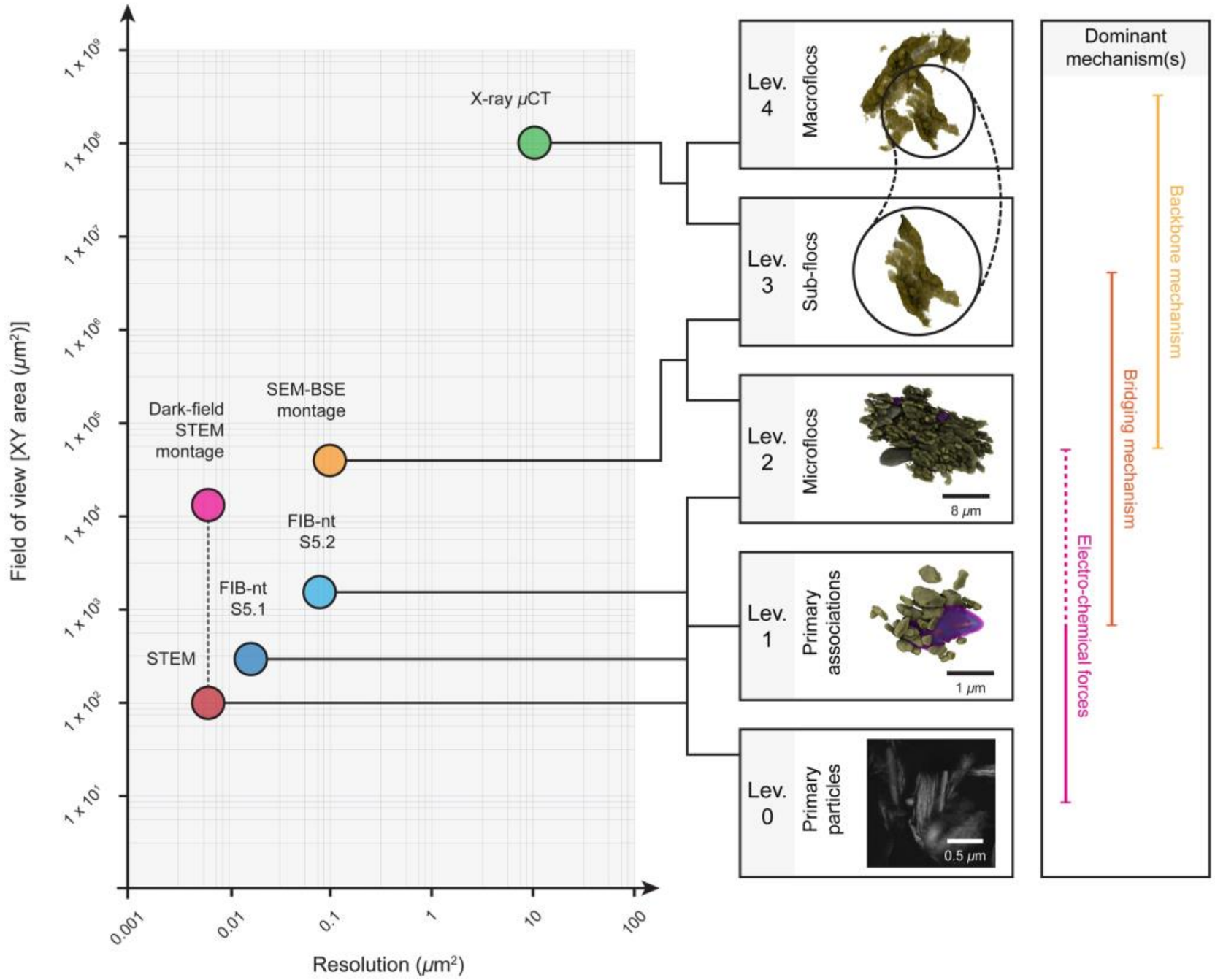

Figure 4.1. Schematic showing the hierarchical structure of the aqueous floc samples revealed by the correlative datasets. The graph shows the datasets collected from flocs S4 and S5 which are plotted by their resolution and field of view (XY). Five levels of organisation are identified within the floc samples*: Level 0* – Primary particles*, Level 1* – Primary associations*, Level 2* – Microflocs*, Level 3* – Sub-flocs *and Level 4* – Macroflocs. Also shown are the mechanisms that are believed to govern floc structure and the length-scales over which they operate.

what would be expected in natural estuarine flocs (e.g., Eisma, 1986; Alldredge & Silver, 1988; Leppard *et al*., 1997; Droppo, 2001; Burd & Jackson, 2009), including inorganic particles (e.g., clays and non-clay minerals) and an abundance of organic material (e.g., bacteria, organic debris and fibrillar EPS) (Figure 3.1). Further information regarding the fine-scale structure of the flocs (Levels 1 and 2) was obtained by artificially extending the field of view of STEM by image montaging (area analysed 113 × 147 μm^2).

A critical limitation of TEM and STEM is that the analysis is restricted to 2D imagery, which may result in erroneous interpretations of 3D structure (Holzer *et al*., 2004; Uchic *et al*., 2007; Münch *et al*., 2006; Singh & Gokhale, 2005). A degree of error may accrue from the extrapolation to a 3D entity of quantitative metrics measured from a 2D surface. An estimate of this error was obtained by comparing the values of multiple quantitative parameters obtained from three different 2D slices of a 3D FIB-nt dataset to their respective values obtained from the volume as a whole. For the sub-volume S5.2-2 (Figure 3.12a), three slices evenly distributed in the sample were queried in comparison to the total volume and size parameters measured as shown in Table 3.2. Measure of the density of occupation of the floc varied by 12% with occupied volume overestimated by as much as 11 percentage points or nearly one third of the actual occupied volume. The largest discrepancies occurred for discrete structural entities distributed randomly within the volume, i.e. non-clay minerals and organic material (debris and microbial cells). For these features the probability of being captured in a slice decreases with their size and frequency. For example, slice S5.2-2_0 passed through a large non-clay mineral grain which on its own comprised >50% of the non-clay mineral fraction of the sample. As a result, the measured non-clay mineral fraction was significantly overestimated. Slices S5.2-2_127 and S5.2-2_254 in contrast do not pass through this grain and significantly underestimate the non-clay mineral fraction of the volume. Extrapolation is dependent on the assumption that materials are evenly distributed throughout the volume, an assumption that is incompatible with the established irregularity in floc shape and structure. 2D TEM and STEM images are therefore unsuitable for the reconstruction of 3D geometries. However, the limited resolution of FIB-nt prevents the recognition of certain floc constituents (e.g., fibrillar EPS), and TEM and STEM data can therefore provide valuable insights regarding floc composition and the disposition of certain structural elements.

Level 0 is considered to consist of the elementary building blocks of all other floc structures, ranging from individual clay platelets to larger silt grains and organic debris

(Figure 3.1). Whilst some primary particles may appear in isolation (e.g., silts grains), clay minerals appear to be transported in discrete multi-platelet units. This is illustrated in Figures 3.6c and d in which clay platelets are observed to be organised into multi-particle units, aligned in either 'stacked' or 'stepped' arrangements. In marine and sedimentary geology associations of this type are usually referred to as 'domains' (Aylmore & Quirk, 1959; Moon, 1972; Bennett *et al*., 1991; Curry *et al*., 2007). Based on the result of ultrasonication, Jorand *et al*. (1995) illustrated that flocs could not be broken down beyond these elementary units. These results corroborated computer simulations that showed failure only after consolidation and/or significant shear (Bennett, 1976; Bennett *et al*., 1977). As a consequence of their significant structural integrity, these units behave functionally as single particles (Bennett *et al*., 1991). The size of the pure clay domains within macroflocs S4 and S5 were found to vary between ~0.5 and 3 μm, with variation likely to be a reflection of clay mineralogy.

Within the floc samples primary and multi-platelet particles were found to be arranged into discrete units that are defined here as *primary associations*. These structures occupy the second level of organisation within the hierarchical model (Level 1; see Figure 4.1). This term encompasses several well-defined arrangements of particulate material. Elsewhere in the literature such associations are recognised as microfabric 'signatures' (e.g., Bohlke & Bennett, 1980; Bennett & Hulbert, 1986; Bennett *et al*., 1991; Curry *et al*., 2009). By far the most frequent primary associations observed within macroflocs S4 and S5 were clay domains aligned face-to-face and/or edge-to-face (Figures 3.1a and 3.11) and bacterial cells surrounded by clay domains in an 'onion skin' pattern (Figures 3.1b and 3.13j and k). The EPS present within the nanometre pores of these types of primary associations is presumed to have a stabilising effect, acting to physically bridge clay domains and microbes (Liss *et al*., 1996; Droppo, 2001; Liss, 2002; Winterwerp & van Kesteren, 2004). The frequency of occurrence of these bacteria-clay domains and the spatial arrangement of clays around the bacteria, which can only be observed using these volumetric techniques, emphasises the importance of bacteria as building blocks and providing floc stability.

2D dark-field STEM (Figure 3.6a) and SEM-BSE image montages (Figures 3.8a and d) collected from the surface of the sample blocks show how primary associations are arranged into larger structures, which are classified here as microflocs. These occupy Level 2 of the hierarchical model (see Figure 4.1), and can be characterised by their open card-house structure with primary associations arranged with edge-to-face contacts. In 3D, it is possible to differentiate between microflocs based on inter-aggregate porosity (Figures 3.15a and e),

and a qualitative assessment of their size shows that they typically have a diameter of <40 μm. High-resolution imagery obtained via STEM shows that the intra-aggregate pores of these structures are often filled the polymeric fibrils (Figures 3.1a and 3.6a). This soluble EPS is distinct from the EPS observed linking bacteria and clay particles in primary associations (Level 1), which is tightly bound to the exterior of cell walls (Liss, 2002). Whilst a large proportion of soluble EPS within the flocs are likely to originate from the metabolic synthesis of floc colonising bacteria, Yallop *et al*. (2000) and Gerbersdorf *et al*. (2009) have demonstrated that there are multiple sources of fibrillar EPS within aquatic sediments, including diatoms which are known to produce copious quantities of fibrillar material (Smith & Underwood, 1998; Garcia-Aragon *et al*., 2011).

Previously, the classification of floc sub-structure has been reliant on relatively arbitrary size brackets and/or proxy indications of structure such as stability (Mikkelsen *et al*., 2006). The term 'microfloc' has been used as an umbrella term to designate floc sub-structures with a diameter of <~100 μm (e.g., Eimsa, 1986; Manning, 2001), which have been shown by experimental (e.g., Hill *et al*., 2001; Agrawal & Traykovski, 2001; Tan *et al*., 2014) and *in situ* observational studies (e.g., Eimsa, 1986; Kranck & Milligan, 1992; Manning & Dyer, 1999; Mikkelsen *et al*., 2006; Manning *et al*., 2011) to be difficult to disaggregate under high turbulent shear (see § 1.2). These methods of classification, however, fail to account for the variability in floc characteristics observed between environments, and do not inform on the mechanisms controlling their stability, without which a coherent model of flocculation remains elusive. The datasets present here offer a means of obtaining an alternative structural definition based on direct observations of structural associations, which may provide a more robust understanding of the origin of different floc sub-structures and their long term stability.

Both floc samples were shown to contain units of densely packed material (diameter, ~30 μm) (Figure 3.6i). Particle forms of this nature are not uncommon within flocs, and have been reported by several studies (e.g., Walling & Woodward, 2000; Droppo & Amos, 2001; Droppo *et al*., 2005a; Garcia-Aragon *et al*., 2011). These units are usually interpreted as being either: i) water stable soil aggregates originating from outside of the water column, or ii) flocculated material that has undergone self-weight consolidation in the bed and that has subsequently been resuspended following erosion (Wall *et al*., 1978; Partheniades, 1986; Droppo & Amos, 2001; Droppo *et al*., 2005a). These previous studies have found it difficult to distinguish between aggregates originating from surface overland flow and resuspended

material. The distinction is important when considering the movement of contaminants through an aquatic system, as they will usually do so in association with delivered aggregates (i.e. soil aggregates) or with material remobilised from the bed (i.e. legacy contaminants associated with bed aggregates) (Droppo *et al.*, 1998; 2001; Garcia-Aragon *et al.*, 2011; Droppo *et al.*, 2014). Therefore, different contaminants may have different modes of transport and delivery (e.g., nutrients and fertilisers from agricultural run-off). Whilst it is impossible to assume the origin of the majority of dense aggregates observed in macroflocs S4 and S5, certain examples are shown to contain material indicative of their origin, including bioclasts, e.g., diatom frustules, that point towards initial formation in suspension in the aquatic environment, rather than terrestrial (Figure 3.8d).

Unlike loosely bound particles flocculated in suspension that are prone to breakage, these denser aggregates are more resilient (Milligan & Hill, 1998; Garcia-Aragon *et al.*, 2011). Erosion experiments conducted by Droppo & Amos (2001) found that aggregates resuspended from the bed exhibited an inherent shear strength that was likely to be the result of biostabilisation and consolidation. Soil aggregates, which originate through ballistic rain-splash, surface wash or rill erosion (e.g., Moss & Green, 1983; Poesen *et al.*, 1996), will possibly display a similar degree of strength (Droppo *et al.*, 2005a). Consequently, whilst these consolidated aggregates are often significantly larger than multi-particle units they can be considered to occupy the same level of organisation, behaving in a functional sense as a single unit (Figure 4.1). Quantifying the physical characteristics of these microfloc units, such as their porosity and density, which is now possible utilising these 3D FIB-nt data, could have very significant implications for understanding the transport characteristics of contaminants either delivered to the aquatic environment associated with soil aggregates, or reworked from *in-situ* historically contaminated sediments.

At the millimetre-scale the macrofloc structure (Levels 4) can be subdivided into several smaller structures termed here as sub-flocs (Levels 3), which are held together by narrow linkages. This is illustrated in Figure 3.16, which show reconstructions of the 3D X-ray μCT scans of macroflocs S4 and S5. The structure(s) responsible for binding sub-flocs into macroflocs could not be confirmed due to the limited voxel resolution of the μCT scans (10 μm). However, the 2D and 3D nano- and micrometre datasets showed that macroflocs S4 and S5 contained significant quantities of organic material (see §3.2 and 3.3 and above), including fibrillar EPS which is believed to be responsible for the strength and pseudo-plastic nature of flocculated material (Droppo and Ongley, 1992, 1994; Liss *et al.*, 1996; Droppo,

2001). As discussed above, EPS can clearly be seen linking multi-platelet clay particles within primary associations (Figures 3.1a) and can be observed filling the micrometre pore space between floc sub-structures (e.g., microflocs) (Figure 3.6a). Previous studies investigating the external characteristics of flocs using ESEM (e.g., Droppo, 2001; Garcia-Aragon *et al*. 2011) have demonstrated that EPS fibrils often extend beyond the limits of the main floc structure (defined by inorganic clays), forming organic coatings at the floc surface. These coatings are likely to help in the aggregation process of small structures (e.g., primary associations and microflocs) (Droppo, 2001), but additional support structures are required to prevent disaggregation of larger sub-flocs following initial contact. This can be provided by filamentous bacteria, which due to their length and association with EPS (Urbain *et al*., 1993), act as anchors between multiple floc sub-structures, forming a skeleton or 'backbone' within large (macro)flocs (Sezgin *et al*., 1987; Liss, 2002; Chung & Lee, 2003; Martins *et al*., 2004) resulting in the backbone bridging mechanism described in Figure 4.1. The presence of filamentous organisms within flocs directs their development (Sezgin *et al*., 1987), and promotes the growth of flocs with shapes other than spherical, i.e. irregularly shaped 'stringer' type macroflocs such as S4 and S5 (Nguyen *et al*., 2007). Observations made using 2D STEM and SEM showed several species of filamentous bacteria to be present within macroflocs S4 and S5 (Figures 3.1e, 3.6a and 3.8). 3D FIB-nt confirmed that these extended through the floc sub-structure (Figure 3.15), and it is likely that these filamentous bacteria were responsible for binding sub-flocs together. During sampling it is possible that the additional support provided by these organisms helped prevent floc-breakage. Although this study did not collect nano- or micrometre datasets at the linkages of sub-flocs, these are could be in future target as an region of interest using the methodology described here. This would provide the opportunity to confirm the structural elements connecting sub-flocs to form the larger moieties.

As described above, flocs in suspension will often contain a variety of material from different sources (e.g., water stable soil aggregates as opposed to material flocculated in suspension), the transport histories of which may vary significantly. When discussing floc structure, it is therefore important to bear in mind that certain structures may be 'relics' or recycled material that have undergone several phases of settling, erosion and resuspension during their life cycle (Droppo *et al*., 1998; Droppo *et al*., 2001; Droppo, 2004). The longevity of such structures is ultimately dictated by their stability, which at higher scales is largely determined by the presence of organics which provide additional strength. With this

in mind, it is suggested that some of the sub-flocs identified in macroflocs S4 and S5 could be relics that resisted disaggregation when resuspended during the flocculation experiments (§ 2.2.1). However, this is difficult to confirm with the current datasets. Given that organics play such a strong role in determining the size and shape of flocs at these higher length scales, it follows that these levels of organisation of the floc structures most likely to be variable between environments. This is supported by observational studies conducted in environments that are less biologically active such as alpine lakes (e.g., Woodward *et al.*, 2002; Hodder & Gilbert, 2007; Hodder, 2009)] in which floc diameters are shown to be several orders of magnitude smaller than those found in environments such as estuaries the organic content of which accounts for a significant proportion of SPM.

It is recognised that the mechanisms responsible for the development of different floc (sub-)structures operate over specific length-scales (Figure 4.1) (Bennett *et al.*, 1991; Curry *et al.*, 2009). At the nanometre-scale, strong electro-chemical forces are responsible for the development of multi-platelet particles (domains) and primary associations (Levels 0 and 1) (Bennett *et al.*, 1991; Grabowski *et al.*, 2011), but these become progressively weaker with increasing structure size (Bennett *et al.*, 1991). Larger micro-flocs and sub-flocs (Levels 2 and 3) occur as a result of inter-particle cohesion at the micrometre-scale, with EPS providing a support structure that binds and strengthens material together (Liss *et al.*, 1996; Droppo *et al.*, 1997; Droppo, 2001). At the (sub)millimetre-scale macroflocs (Levels 4) occur and are highly fragile, only developing in the presence of biological material such as filamentous algae (Manning & Dyer, 2002; Chen *et al.*, 2005), with filamentous bacteria providing a backbone support structure in addition to bridging EPS (Jenkins *et al.*, 1993; Liss, 2002; Chung & Lee, 2003; Martins *et al.*, 2004). Only by investigating floc structure across a range of spatial scales can an adequate understanding of the mechanisms responsible for floc development be formulated.

The reliance on fractal theory in parametrising sediment transport models persists in the absence of a fully elaborated understanding of the functional relationships between floc structure and behaviour. In order to account for variable floc structures (e.g., microflocs and macroflocs) it has been necessary to modify the theory by the addition of variable fractal dimensions. However, this convention is not underpinned by a theoretical understanding of why these structures form, but is rather a reaction to their presence. The results presented here suggests that fractal geometry is unstable for the description of these flocs, which consists of a variety of material with different properties (e.g., size, shape etc.) that can be

seen to form a diverse range of structures that may be similar in size but differ in character. The correlative workflow offers a means of understanding particle and structural associations and the mechanisms operating at different length-scales that promote flocculation.

4.4. Critical Evaluation of Correlative Tomography

4.4.1. Merits of the Correlative Workflow

The task of correlating submerged high-resolution 3D volumes and 2D images within lower resolution scans of an entire specimen is challenging, and represents a critical potential source of error within the correlative workflow. However, the results presented in Section 3.5 demonstrate that alignment of the 2D and 3D multi-scale datasets obtained from the macroflocs S4 and S5 could be achieved within an acceptable level of accuracy. Similar to previous studies, registration was influenced by the quality (i.e. resolution, contrast and signal-to-noise ratio) and degree of similarity (i.e. resolution and mechanisms for contrast generation) between the different datasets (e.g., Caplan *et al.*, 2011; Murphy *et al.*, 2011; Handschuh *et al.*, 2013; Cao *et al.*, 2014).

Within the X-ray data volumes, the metal registration pins were easily identifiable by their distinctive shape and high grey-scale values (Figure 3.16), making them suitable for landmark-based registration. Segmentation was required to delineate the metal registration pins positioned within the two corresponding millimetre-scale μCT datasets, and for accurate registration the pins would ideally be represented by a similar number of voxels. The observed discrepancy in the size of the pin between the two datasets was 1.6% (macrofloc S4) and 3.8% (macrofloc S5) (Table 3.6). This can be attributed primarily to scan artefacts (Figures 3.16a and b) with secondary edge effects arising from different mixed pixel (or 'mixels') classifications where the orientation of the voxel grid with reference to the pin was not consistent. Assuming an even distribution of the extraneous voxels around the perimeter of the pin, the minimum offset between co-registered datasets can be estimated to be of the order of less than a voxel (~3 – 6 μm) over a total 3D size of 10×10^8 μm. With evidence of only minor peripheral misalignment of the registered datasets, the co-registration of the X-ray scans is considered to have been successful.

2D SEM-BSE images montages taken from the surface of the flocs were critical to the co-registration of the nano- and micrometre datasets with the larger X-ray CT scans (Figures

3.17 and 3.18). When aligning two or more datasets with different resolutions, the accuracy of registration is determined by the proficiency with which landmark features within the dataset with the lowest resolution can be recognised (Caplan *et al*., 2011). Feature boundaries within an image are usually defined by a grey-scale gradient (Holzer *et al*., 2004), as illustrated in Figure 3.7. Consequently, the error margin will be determined by the size of this transition zone, which may consist of several pixels depending on image quality. The trapezoidal shape of the sectioned surface of sample blocks could be clearly defined in the X-ray datasets, enabling the SEM-BSE montages to be tied to the surface within an accuracy of 3 – 6 voxels (~30 – 60 μm). However, further confidence can be obtained by comparing the actual shape of the floc in the two datasets. Downscaling the SEM-BSE image montages to the same resolution as that of the X-ray μCT data volumes (~10 μm) enabled a direct comparison of the relative positions of the floc boundary (Figures 3.17 and 3.18), the result of which indicate the accuracy of co-registration to be less than a voxel (<10 μm). A comparison of the downscaled SEM-BSE image montage with the corresponding μCT slice provides a means of validating the potential floc structures responsible for different grey-scale values, and regions of the floc observed to contain high concentrations of particles in the BSE-SEM montages were shown to exhibit high grey-scale values in the X-ray CT datasets.

Images obtained from the surface of the sample blocks prior to and post 3D serial sectioning ensured a static frame of reference with which to orient FIB-nt data volumes relative to the SEM-BSE montages. The similar (BSE) imaging conditions selected for both SEM image montaging and FIB-nt allowed reference landmarks within the corresponding datasets to be recognised with a high degree of certainty (20 – 60 nm). As the contrast mechanisms in both SEM-BSE and dark-field STEM are similar and are related to atomic number, tie-point features were easily identifiable. However, inspection of the over-laid images following registration revealed discrepancies in position of key landmarks. Given the known orientation of the sample relative to the ultrathin-sections these observed off-sets cannot be explained entirely by sample geometry alone. It is more likely that these displacements are the result of ultramicrotomy, as shear stresses imposed during sectioning are known to cause thin-section compression (Smart & Tovey, 1982). This is supported by the presence of several artefacts associated with compression (e.g., folds and rumples, slip planes etc.) (Figures 3.5 and 3.6).

Whilst the different datasets could be registered with an acceptable degree of accuracy based on landmarks features, the correlation of structural elements between the length-scales was rendered difficult in certain instances where there was a large gap in resolution between the image data. Figure 4.1 shows a graphical representation of the datasets collected from macroflocs S4 and S5, which are plotted by their resolution and field of view (XY). It is clear from this graph that a significant gap in resolution exists between FIB-nt and X-ray μCT. The volume of a voxel in the μCT datasets (10 μm, vol. 1000 μm^3) is 2.9×10^8 times larger than in S5.1 (15 nm, vol. 3375 nm^3), and 3.3×10^6 larger than in S5.2 (67 nm, vol. 300763 nm^3). Consequently, the volumes of S5.1 and of S5.2 occupy the equivalent of ~4.3 and ~75.6 voxels of the μCT datasets respectively. The lack of overlap between the datasets inhibited the correlation of structural features observed in the FIB-nt datasets at the micrometre-scale with millimetre-scale floc structure. However, the observed variability in X-ray attenuation through the flocs likely reflects density variations at the sub-voxel (micrometre) scale in response to the partial volume effect (e.g., Long *et al.*, 2009; Ketcham & Carlson, 2001; Cnudde & Boone, 2013; Bendle *et al.*, 2015), and that areas exhibiting higher X-ray attenuating properties contain a higher concentration of material and are consequently less porous. Down scaling the high-resolution SEM-BSE image montages to match the resolution of the X-ray CT datasets supports this hypothesis (Figure 3.18). In contrast, the similar resolution between dark-field STEM (~6 nm^2) imagery and FIB-nt (BSE) data volumes and the similarity of their contrast mechanisms, enabled the same structural elements to be identified within both datasets.

4.4.2. The Suitability of Correlative Tomography for Future Floc Studies

The results presented above demonstrate that correlative tomography can be successfully applied to investigate the multi-scale 3D structure and composition of fragile aqueous flocs. This is a significant advance on current analytical techniques (e.g., photo and video image analysis) that can only measure 3D flocs as 2D geometric simplifications. The correlative datasets collected from macroflocs S4 and S5 provide an improved understanding of the hierarchical structure of flocculated material, revealing new information regarding particle and structural associations and confirming that flocs are not fractal in nature. However, it is important to note that the correlative workflow when employed in its entirety is time consuming and technically demanding (see § 4.4.1). By far the most labour intensive aspect of the workflow is that of data processing (i.e. image enhancement, segmentation and

correlation), which severely limits the total number of samples that can be analysed. Indeed, a single FIB-nt dataset may require days or weeks of processing, making the analysis of 100's – 1,000's of flocs [as is usually achieved when using *in situ* techniques such as video image analysis, e.g., (Manning & Dyer, 2007; Milligan *et al*., 2007)] impractical. Realistically the number of floc samples that can be investigated in detail using the entire workflow described here (from millimetre-scale through to nanometre-scale) is limited to 10's of samples.

Of importance then, is the development of a sampling strategy that permits an assessment to be made of both the representativeness of individual samples and the degree of variance across a floc population. This study has been primarily concerned with establishing the methodology of the correlative workflow, and it has been outside the scope of this study to assess macroflocs S4 and S5 within the context of the floc population from which they were sampled. That said, the correlative approach is well suited to the application of a targeted imaging strategy, whereby the results of low resolution scans inform on representative floc samples for analysis and the siting of a RoI for imaging at finer-scales.

The methodology outlined in Figure 2.2 can be adapted to include a preliminary step that would permit representative flocs to be selected for analysis. These adaptations and the rationale behind them are discussed in detail in Section 5.2 (Future Improvements and Applications), however, the key points of the workflow are:

- The incorporation of a video imaging system [e.g., LabSFLOC (Manning *et al*. 2010)] to facilitate the measurement of floc settling velocities. This would allow the empirical relationship between internal floc structure and settling velocity to be investigated with the aim of improving/modifying Stokes' Law.

- The use of plankton chambers for sampling fragile flocs and agarose as a means of immobilising flocs prior to stabilisation.

- The scoping of floc samples by non-destructive X-ray μCT, the efficiency and speed of which (scan time, ~2.5 hours) permits 100's – 1,000's of individual flocs to be scanned in a single session. This will statistically describe the parameters of the floc population, and identify those parameters which distinguish different populations. Based on these results, representative individual floc samples can be selected for further correlative analysis.

If successful, this approach will provide a more robust means of defining floc structure-function relationships.

4.5. Implications of Findings

This study has successfully developed a novel method for investigating floc composition and 3D structure at multiple length-scales. These results have corroborated certain elements of our understanding of flocs, but have called into questions other aspects, including the validity of fractal behaviour. The implications of this work are as follows:

- Whilst the stabilisation procedure likely results in the extraction of certain structural elements (e.g., fibrillar EPS) and volume shrinkage, floc samples can be stabilised with minimal perturbation allowing accurate 3D description. This method is suitable for preparing flocs from different environments, and could be used in conjunction with the correlative workflow to assess how different aquatic conditions influence floc structure.

- TEM and STEM are required for nanometre-scale floc characterisation, but the 2D imagery these techniques provide cannot be used to reconstruct accurate 3D geometries. 3D information over a range of scales is essential to understand floc structure, and can only be achieved via correlative tomography, which threads together multiple 3D imaging techniques (e.g., FIB-nt and X-ray μCT).

- The correlative workflow was applied here to test its feasibility for investigating the hierarchical structure of aqueous flocs. The results presented here, therefore, are not attempting to describe a 'typical' floc. Instead, a methodology is successfully tested that could allow future studies to identify and investigate the hierarchical structure of a representative sample of flocs.

- The quantification of various floc metrics is possible by sophisticated image analysis and provides a better understanding of floc characteristics (e.g., porosity, mineral content and the viability and distribution of microbial communities etc.).

- The correlative datasets allow a new model of floc structure to be proposed that is based on the association of structural components and their stability, rather than arbitrary size brackets and/or gross settling behaviour. This approach will enable a

better understanding of the behaviour of different floc systems (dynamic and transport behaviour), the influence of environmental conditions (e.g., composition, fresh vs salt water), influence of pollutants on the structure of flocs, transport of pollutants in aquatic environments and potential methods for removal of contaminants from water systems.

- The data presented here suggest that a fractal-based method for describing the structure of macroflocs S4 and S5 would be unsuitable. The use of fractal geometry as a descriptor of floc structure is not, therefore, applicable to all flocs. The model of floc structure proposed here (Figure 4.1) could provide the foundations for universal description, allowing more adaptive and predictive simulations of floc transport to be developed.

Chapter Five: Conclusion

5.1. Concluding Remarks

In this study, the potential of correlative tomography for investigating the hierarchical 3D structure and composition of flocculated sediment was assessed. It has been shown that by combining several imaging modalities into a single correlative workflow, access can be gained to much larger range of spatial scales for a single region of interest than would otherwise be possible using a single technique alone. Here, this is achieved by threading together X-ray μCT datasets (resolution ~10 μm^3, volume of several mm^3), SEM-BSE images montages (resolution ~60 nm^2, area analysed ~218 × 170 μm^2), FIB-nt data volumes (resolution ~15 – 70 nm^3, maximum volume size ~1.25 × 10^5) and TEM and STEM imagery (resolution ~6 nm^2, 10 × 10 μm^2), which allow flocs to be characterised from the millimetre-scale through to the nanometre-scale.

Specifically, this initial application of correlative tomography has shown that:

- The techniques utilised for the capture of fragile hydrated flocs result in minimal structural damage, and flocs can be successfully rendered vacuum stable for correlative analysis using the protocol described here.
- The correlative workflow enables the collection of datasets that can be successfully aligned in 3D space based on landmark features. At present, the resolution gap between 3D FIB-nt and X-ray CT prevents certain structural entities from being directly correlated. However, by downscaling high-resolution SEM-BSE image montages an understanding of the floc structures responsible for the grey-scale values observed in the X-ray CT datasets can be gained. Due to the similarity in resolution and contrast mechanisms FIB-nt datasets are directly comparable.
- FIB-nt and X-ray CT can provide accurate 3D data that is suitable for quantitative analysis, and this enabled the complex 3D shape and structure of flocs at different length-scales to be described accurately for the first time. Using FIB-nt datasets compositionally information could be extracted and the datasets demonstrated flocs to be composed of a diverse range of materials the interactions between which result in an array of structures.

- Structural and compositional information obtained using correlative tomography enabled the development of a new model that describes the hierarchical structure of flocculated sediment, in addition to an understanding of the mechanisms responsible for the development of these structures and the length-scale over which they operate.

5.2. Future Improvements and Applications

This investigation has demonstrated the potential of correlative tomography for the investigation of aqueous floc samples. Nevertheless, it is recognised that several areas of the correlative workflow require future improvements. These include:

- *Floc acquisition*: A major source of uncertainty for the study was the effect of pipetting on fragile floc samples. Whilst macroflocs S4 and S5 showed minimal signs of breakage, future studies should aim to mitigate against any destructive forces which may occur during sampling. Several techniques for sampling delicate flocs have been proposed (Liss *et al*., 2005), but by far the most successful is outlined by Droppo *et al*. (1996). This method utilises plankton chambers for the capture of flocs and agarose as a medium in which to 'immobilise' them prior to stabilisation. Plankton chambers are suitable for both field (e.g., Droppo *et al*., 1997; Woodward *et al*., 2002; Leppard *et al*., 2003; Plach *et al*., 2011; Elliott *et al*., 2012) and laboratory (e.g., Liss, 2002) based studies, and their use in conjunction with agarose eliminates the need for bulk transfer, storage, and subsampling in preparation for microscopic investigation (Droppo *et al*., 1996). Once flocs have settled into the plankton chamber excess water is removed from the chamber leaving the flocs suspended in 3 ml of water. Low-melting point agarose (previously held at 35°C) is then added to the chamber and allowed to solidify. The result of this procedure is that floc samples are retained in a resilient medium which can be transported, stored and subsequently stabilised for correlative analysis (Droppo *et al*., 1996; Liss, 2002). Whilst the primary objective of immobilisation is to prevent morphological changes to the flocs brought about during sampling, the use of agarose could also provide a means of quantifying stabilisation artefacts by enabling flocs to be imaged both before and after stabilisation (see below). 'Wet' immobilised flocs would not be suitable for imaging with all techniques (e.g., FIB-nt and TEM), but 3D X-ray μCT offers a viable method

for performing a preliminary scan allowing morphological changes at millimetre scale to be assessed.

- *Floc stabilisation*: Currently no one technique exists which allows flocs to be rendered vacuum stable without perturbation, and the effects of resin based stabilisation represent a critical source of error that is difficult to quantify. Recent studies (e.g., Leppard, 1992a; Liss *et al*., 1996; Leppard *et al*., 1996) have adopted a multi-preparatory method for floc stabilisation, which combines several preparation techniques and applies them in comparative manner in order to overcome the specific artefacts inherent to each of the individual methods (see § 1.3.5 and 2.2.2). While this approach is useful, the inability to image flocs prior to stabilisation prevent the effects of stabilisation from being quantified, and a comprehensive study of the artefacts associated with the different imaging methods is yet to be undertaken. As discussed above, the use of agarose for the 'wet' immobilisation of floc samples provides a potential means by which to image fragile flocs prior to stabilisation using 3D μCT. This would allow any morphological changes induced by stabilisation at the millimetre-scale to be measured. However, many of the changes that occur during stabilisation are known to take place at the nano- and micrometre-scales, and these cannot be investigate using the techniques deployed in the current correlative workflow, i.e. TEM and FIB-nt, as these operate at a high vacuum and cannot be used to analyse 'wet' samples. Structural changes at the nano- and micrometre-scale could be inferred using CLSM, which has a limited resolution but does has the capability to resolve individual bacteria. The use of bacteria as structural landmarks of change therefore could be an option, as samples could be scanned in agarose using X-ray CT and CLSM prior to and post resin embedding to identify millimetre and micrometre structural change.

Whilst an assessment of the traditional stabilisation methods is critical, the suitability of new techniques should also be explored. For example, recent technological innovations have made cryo-fixation a viable means of floc stabilisation. While conventional methods of shock freezing resulted in the growth of large destructive ice crystals (Zingg *et al*., 2008; Holzer *et al*., 2010), these artefacts are reduced considerably in newly designed high-pressure freezing (HPF) apparatus (Studer *et al*., 2001). Recently HPF has been successfully used to stabilise fragile hydrated cement pastes (e.g., Holzer *et al*., 2007; Zingg *et al*., 2008; Holzer *et al*.,

2010; Lubelli *et al*., 2013) and consolidated clays (Keller *et al*., 2011a; 2011b; 2013) for microstructural analysis using FIB-nt.

- *Imaging methods*: The correlative workflow is flexible and can be adapted to incorporate other imaging methods. The most obvious technique that future studies may want to employ is video or photographic imaging systems, which would provide a means of measuring of floc settling velocities, enabling floc structure-function relationships to be investigate. Under laboratory conditions this could be achieved by settling flocs directly into plankton chambers and immobilising settled flocs within agarose for eventual stabilisation and imaging at higher resolution.

  To enable a better understanding of how floc structures at the micrometre-scale relate to whole floc samples at the millimetre-scale it is suggested that future work attempt to address the resolution gap between X-ray μCT and 3D FIB-nt. As described in Section 1.4, Hemes *et al*. (2015) and used BIB-tomography to bridge the gap between micrometre FIB-nt datasets and X-ray CT scans when investigating consolidated clays, and this is a suitable technique that could be integrated within the workflow. However, this approach is destructive limiting further analysis with higher resolution imaging techniques to areas of the sample that have not been milled. An alternative technique which may address this problem is X-ray nano-CT, which is non-destructive (Farah Ahmed *pers. comm.*).

- *Offline data processing*: Image processing is critical to ensure accurate quantitative results and that all information present within the images can be extracted. By far the most important area that requires future improvement is that of segmentation. Segmentation was achieved here using the TWS plugin in Fiji/ImageJ, a semi-automated technique which was shown to provide good results for different material. Any method based on grey-scale contrast will have difficulties when distinguishing closely packed particles with similar grey-level values, e.g., clay platelets aligned face-to-face. More sophisticated processing algorithms that employ 3D shape as means of segmentation e.g., concave curvature segmentation (e.g., Hobson *et al*., 2009; Wang *et al*., 2012) have the potential to extract these difficult to segment particles.

References

Abramoff, M.D., Magalhães, P.J., Ram, S.J. (2004). Image processing with ImageJ. *Biophotonics International*, **11**(7): 36-43.

Agrawal, Y.C., Pottsmith, H.C. (2000). Instruments for particle size and settling velocity observations in sediment transport. *Marine Geology*, **168**: 89-114.

Agrawal, Y.C., Traykovski, P. (2001). Particles in the bottom boundary layer: Concentration and size dynamics through events. *Journal of Geophysical Research*, **106**(C5): 9533-9542.

Alldredge, A.L., Silver, M.W. (1988). Characteristics, dynamics and significance of marine snow. *Progress in Oceanography*, **20**(1): 41-82.

Amos, C.L., Droppo, I.G. (1996). The stability of remediated lakebed sediment, Hamilton Harbour, Lake Ontario, Canada. *Geological Survey of Canada Open File Report*, No. 2276.

Arganda-Carreras, I. (Sept 2015). *Trainable Weka Segmentation: A tool for machine-learning-based image segmentation*. Poster presentation, Image-J User and Developer Conference, Madison, WI.

Armer, H.E.J., Mariggi, G., P'ng, K.M.Y., Genoud, C., Monteith, A.G., Bushby, A.J., Gerhardt, H., Collinson, L.M. (2009). Imaging transient blood vessel fusion events in zebrafish by correlative volume electron microscopy. *PLoS One*, **4**: e7716.

Axford, S.D.T., Herrington, T.M. (1994). Determination of aggregate structures by combined light-scattering and rheological studies. *Journal of the Chemical Society-Faraday Transactions*, **90**: 2085-2093.

Aylmore, L.A.G., Quirk, J.P. (1960). Domain or turbostratic structure in clays. *Nature*, **187**: 1046-1048.

Baas, J.H., Davies, A.G., Malarkey, J. (2013). Bedform development in mixed sand–mud: The contrasting role of cohesive forces in flow and bed. *Geomorphology*, **182**: 19-32.

Braet, F., Geerts, W.J. (2009). Foreword to the themed issue on correlative microscopy. *Journal of Microscopy*, **235**(3): 239-240.

Baerwald, R.J., Burkett, P.J., Bennett, R.H. (1991). Techniques for the preparation of submarine sediments for electron microscopy. In R.H. Bennett, W.R. Bryant, M.H. Hulbert (Eds.), *Microstructure of Fine-Grained Sediments: From Mud to Shale* (pp. 309–320). Berlin: Springer-Verlag.

Bassim, N.D., De Gregorio, B.T., Kilcoyne, A.L.D., Scott, K., Chou, T., Wirick, S., Cody, G., Stroud, R.M. (2012). Minimizing damage during FIB sample preparation of soft materials. *Journal of Microscopy*, **245**(3): 288-301.

Bendle, J.M., Palmer, A.P., Carr, S.J. (2015). A comparison of micro-CT and thin section analysis of Lateglacial glaciolacustrine varves from Glen Roy, Scotland. *Quaternary Science Reviews*, **114**: 61-77.

Bennett, R.H. (1976). *Clay fabric and geotechnical properties of selected submarine sediment cores from the Mississippi Delta*. Ph.D. dissertation. Texas A&M University.

Bennett R. H., Bryant W. R., and Keller G. H. (1977) Clay fabric and geotechnical properties of selected submarine sediment cores from the Mississippi Delta. NOAA Professional Paper No. 9. U.S. Department of Commerce/NOAA/ERL, pp. 1–86.

Bennett, R.H., Hulbert, M.H. (1986). *Clay Microstructure*. Boston, MA: IHRDC Press.

Bennett, R.H., Ransom, B., Kastner, M., Baerwald, R.J., Hulbert, M.H., Sawyer, W.B., Olsen, H., Lambert, M.W. (1991). Early diagenesis: impact of organic matter on mass physical properties and processes, California continental margin. *Marine Geology*, **159**: 7-34.

Bennett, R.H., Hulbert, M.H., Meyer, M.M., Lavoie, D.M., Briggs, K.B., Lavoie, D.L., Baerwald, R.J., Chiou, W.A. (1996). Fundamental response of pore-water pressure to microfabric and permeability characteristics: Eckernförde Bay. *Geo-Marine Letters*, **16**: 182-188.

Benson, T., French, J.R. (2007). InSiPID: a new low-cost instrument for in situ particle size measurements in estuarine and coastal waters. *Journal of Sea Research*, **58**(3): 167-188.

Bhawana, J.L.M., Cahoon, B.A. (2014). 3D Plant cell architecture of Arabidopsis thaliana (Brassicaceae) using focused ion beam–scanning electron microscopy. *Applications in Plant Sciences*, **2**(6): 10.3732/apps.1300090.s2.

Bohlke, B.M., Bennett, R.H. (1980). Mississippi prodelta crusts: a clay fabric and geotechnical analysis. *Marine Geotechnology*, **4**: 55-82.

Bolte, S., Cordelières, F.P. (2006). A guided tour into subcellular colocalization analysis in light microscopy. *Journal of microscopy*, **224**(3): 213-232.

Bozzola, J.J., Russell, L.D. (1999). *Electron microscopy: principles and techniques for biologists* (2nd edn). Boston: Jones & Bartlett Learning.

Buffle, J. Leppard, G.G. (1995a). Characterization of aquatic colloids and macromolecules. 1. Structure and behavior of colloidal material. *Environmental Science & Technology*, **29**(9): 2169-2175.

Buffle, J., Leppard, G.G. (1995b). Characterization of aquatic colloids and macromolecules. 2. Key role of physical structures on analytical results. *Environmental Science & Technology*, **29**(9): 2176-2184.

Bura, R., Cheung, M., Liao, B., Finlayson, J., Lee, B.C., Droppo, I.G., Leppard, G.G., Liss, S.N. (1998). Composition of extracellular polymeric substances in the activated sludge floc matrix. *Water Science and Technology*, **37**: 325-333.

Burd, B.A., Jackson, G.A. (2009). Particle aggregation. *Annual Review of Marine Science*, **1**(1): 65-90.

Burnett, T.L., McDonald, S.A., Gholinia1, A., Geurts, R., Janus, M., Slater, T., Haigh, S.J., Ornek, C., Almuaili, F., Engelberg, D.L., Thompson, G.E., Withers, P.J. (2014). Correlative tomography. *Scientific Reports,* **4711**: 1-6.

Bushby, A.J., Png, K.M.Y., Young, R.D., Pinali, C., Knupp C., Quantock A.J. (2011). Imaging Three-Dimensional Tissue Architectures by Focused Ion Beam Scanning Electron Microscopy. *Nature Protocols*, **6**(6): 845-858.

Bushby, A.J., Mariggi, G., Armer, H.E.J., Collinson, L.M. (2012). Correlative Light and Volume EM: Using Focused Ion Beam Scanning Electron Microscopy to image transient events in model organisms. *Methods in Cell Biology*, **111**: 357-382.

Bushell, G.C., Yan, Y.D., Woodfield, D., Raper, J.A., Amal, R. (2002). On techniques for the measurement of the mass fractal dimension of aggregates. *Advances in Colloid and Interface Science,* **95**: 1-50.

Cairney, J.M., Munroe, P.R., Schneibel, J.H. (2000). Examination of fracture surfaces using focused ion beam milling. *Scripta Mater,* **42**: 473-478.

Cantoni, M., Holzer, L. (2014). Advances in 3D focused ion beam tomography. *MRS Bulletin,* **39**: 354-360.

Cao, T., Zach, C., Modla, S., Powell, D., Czymmek, K., Niethammer, M. (2014). Multi-modal registration for correlative microscopy using image analogies. *Medical Image Analysis*, **18**(6): 914-926.

Caplan, J., Niethammer, M., Taylor, R.M., Czymmek, K.J. (2011). The power of correlative microscopy: multi-modal, multi-scale, multi-dimensional. *Current Opinion in Structural Biology*, **21**(5): 686-693.

Cardona, A., Saalfeld, S., Preibisch, S., Schmid, B., Cheng, A., Pulokas, J., Tomancak, P., Hartenstein, V. (2010). An integrated micro- and macroarchitectural analysis of the Drosophila brain by computer-assisted serial section electron microscopy. *PLoS Biology*, **8**(10): e1000502.

Carlson, W.D. (2006). Three-dimensional imaging of earth and planetary materials. *Earth and Planetary Science Letters*, **249**(3-4): 133-147.

Casagrande, A. (1932). *The structure of clay and its importance in foundation engineering, Contributions to Soil Mechanics, 1925– 1940* (pp. 72–112). Boston, MA: Boston Society of Civil Engineers Press.

Chakraborti, R.K., Gardner, K.H., Atkinson, J.F., Van Benschotena, J.E. (2003). Changes in fractal dimensions during aggregation. *Water Research*, **37**(4): 873-883.

Chen, S., Eisma, D. (1995). Fractal geometry of in-situ flocs in the estuarine and coastal environments. *Netherlands Journal of Sea Research*, **32**: 173-182.

Chen, M.S., Wartel, S., Temmerman, S. (2005). Seasonal variation of floc characteristics on tidal flats, the Scheldt estuary. *Hydrobiologia*, **540**(1): 181-195.

Chin, W.C., Orellana, M.V., Verdugo P. (1998). Spontaneous assembly of marine dissolved organic carbon into polymer gels. *Nature*, **391**: 568-72.

Chu, C.P., Lee, D.J. (2004). Multiscale structures of biological flocs. *Chemical Engineering Science*, **59**(8-9): 1875-1883.

Chung, H.Y., Lee, D.J. (2003). Porosity and interior structure of flocculated activated sludge floc. *Journal of Colloid and Interface Science*, **267**: 136-143.

Cnudde, V., Cwirzen, A., Masschaele, B., Jacobs, P.J.S. (2009). Porosity and microstructure characterization of building stones and concretes. *Earth Science Reviews*, **103**: 76-83.

Cnudde, V., Boone, M.N. (2013). High-resolution X-ray computed tomography in geosciences: A review of the current technology and applications. *Earth Science Reviews*, **23**: 1-17.

Collins, K., McGown, A.M. (1974). The form and function of microfabric features in a variety of natural soils. *Geotechniques*, **24**: 223-254.

Costerton, J.W., Lewandowski, Z., Caldwell, D.E., Korber, D.R., Lappin-Scott, H.M. (1995). Microbial biofilms. In L.N. Ornston (Ed.), *Annual Review of Microbiology* (pp. 711-745). Palo Alto, CA: Annual Reviews Inc.

Costerton, J.W., Cheng, K.L., Geesey, G.G., Ladd, T., Nickel, J. C., Dasgupta, M., Marrie, T.J. (1987). Bacterial biofilms in nature and disease. *Annual Review of Microbiology*, **41**: 435-464.

Cousin, C.P., Ganczarczyk, J.J. (1998). Effect of calcium ion concentration on the structure of activated sludge flocs. *Environmental Technology*, **20**: 1129-1138.

Curry, K.J., Abril, M., Avant, J.B., Curry, C., Bennett, R.H., Hulbert, M.H. (2002). A technique for processing undisturbed marine sand sediments and reconstructing fabric and porometry. *Journal of Sedimentary Research*, **72**: 933-937.

Curry, K.J., Bennett, R.H., Mayer, L.M., Curry, A., Abril, M., Biesiot, P.M., Hulbert M.H. (2007). Direct visualization of clay microfabric signatures driving organic matter preservation in fine-grained sediment. *Geochimica et Cosmochimica Acta*, **71**: 1709-1720.

Curry, K.J., Bennett, R.H., Smithka, P.J., Hulbert, M.H. (2009). Hierarchal modeling: Biogeochemical processes and mechanisms that drive clay nano- and microfabric development. In A. Malik, R.J. Rawat (Eds.), *New Nanotechniques* (pp. 287-317). Haupage, NY: Nova Science Publishers.

Dade, W.B., Self, R.L., Pellerin, N.B., Moffet, A., Jumars, P.A., Nowell, A.R.M. (1996). The effects of bacteria on the flow behavior of clay–seawater suspensions. *Journal of Sedimentary Research*, **66**: 39-42.

Davis, G.R., Elliott, J.C. (2006). Artefacts in X-ray microtomography of materials. *Materials Science and Technology*, **22**: 1011-1018.

De Boer, D.H., Stone, M., Levesque, M.J. (2000). Fractal Dimensions of Individual Flocs and Floc Populations in Streams. *Hydrological Processes*, **14**, 653-667.

Decho, A.W., Kawaguchi, T. (1999). Confocal imaging of in situ natural micro- bial communities and their extracellular polymeric secretions using Nanoplast resin. *Biotechniques*, **27**(6): 1246-1252.

Deerinck, T.J., Bushong, E.A., Thor, A., Ellisman, M.H. (2010). *NCMIR methods for 3D EM: A new protocol for preparation of biological specimens for serial block face scanning electron microscopy.* San Diego, CA: University of California. Available from: http://ncmir.ucsd.edu/sbfsem-protocol.pdf.

Denison, C., Carlson, W.D., Ketcham, R.A., (1997). Three-dimensional quantitative textural analysis of metamorphic rocks using high-resolution computed X-ray tomography: Part 1. Methods and techniques. *Journal of Metamorphic Geology*, **15**: 29-44.

Denk, W., Horstmann, H. (2004). Serial block-face scanning electron microscopy to reconstruct three-dimensional tissue nanostructure. *PLoS Biology*, **2**(11): e329.

Derjaguin, B.V., Landau, L. (1941). Theory of the stability of strongly charged lyophobic sols and the adhesion of strongly charged particles in solutions of electrolyte. *Acta Physicochimica USSR*, **14**: 633-662.

Desbois, G., Urai, J.L., Perez-Willard, F., Radi, Z., Offern, S., Burkart, I., Kukla, P.A., Wollenberg, U. (2013). Argon broad ion beam tomography in a cryogenic scanning electron microscope: a novel tool for the investigation of representative microstructures in sedimentary rocks containing pore fluid. *Journal of Microscopy*, **249**(3): 215-235.

Desbois, G., Urai, J.L., Kukla, P.A. (2009). Morphology of the pore space in claystones - evidence from BIB/FIB ion beam sectioning and cryo-SEM observations. *E-Earth*, **4**: 15-22.

Dewanckele, J., De Kock, T., Boone, M.A., Cnudde, V., Brabant, L., Boone, M.N., Fronteau, G., Van Hoorebeke, L., Jacobs, P. (2012). 4D imaging and quantification of pore structure modifications inside natural building stones by means of high resolution X-ray CT. *Science of the Total Environment*, **416**: 436-448.

Droppo, I.G. (2001). Rethinking what constitutes suspended sediments. *Hydrological Processes*, **15**(9): 1551-1564.

Droppo, I.G. (2004). Structural controls on floc strength and transport. *Canadian Journal of Civil Engineering*, **31**: 569-578.

Droppo, I.G., Amos, C.L. (2001). Structure, stability, and transformation of contaminated lacustrine surface fine-grained laminae. *Journal of Sedimentary Research*, **71**: 717-726.

Droppo, I.G., Ongley, E.D. (1992). The state of suspended sediment in the freshwater fluvial environment: a method of analysis. *Water Research*, **26**(1): 65- 72.

Droppo, I.G. Ongley, E.D. (1994). Flocculation of suspended sediment in rivers of southeastern Canada. *Water Research*, **28**(8): 1799-1809.

Droppo, I.G., Stone, M. (1994). In-channel surficial fine-grained sediment laminae (Part I): Physical characteristics and formational processes: *Hydrological Processes*, **8**: 101-111.

Droppo, I.G., Flannigan, D.T., Leppard, G.G., Jaskot, C., Liss, S.N. (1996). Floc stabilization for multiple microscopic techniques. *Applied and Environmental Microbiology*, **62**: 3508-3515.

Droppo, I.G., Leppard, G.G., Flannigan, D.T., Liss, S.N. (1997). The freshwater floc: a functional relationship of water and organic and inorganic floc constituents affecting suspended sediment properties. *Water, Air & Soil Pollution*, **99**: 43-53.

Droppo, I.G., Walling, D.E., Ongley, E.D. (1998). Suspended sediment structure: implications for sediment and contaminant transport modelling. In W. Summer, E. Klaghofer, W. Zhang (Eds.) *Modelling Soil Erosion, Sediment Transport and Closely Related Hydrological Processes*, (pp. 437-444). Wallingford: International Association of Hydrological Science Publication, No. 249.

Droppo, I.G., Walling, D.E., Ongley, E.D. (1999). *Suspended sediment structure: implications for sediment transport/yield modelling*. (NWRI Contribution no. 99-098), National Water Research Institute, Burlington, ON, Canada.

Droppo, I.G., Walling, D.E., Ongley, E.D. (2000). Influence of floc size, density and porosity on sediment and contaminant transport. In M. Stone (Ed.), *The Role of Erosion and Sediment Transport in Nutrient and Contaminent* Transfer (pp. 141-147). Wallingford: International Association of Hydrological Sciences Publication, No. 263.

Droppo, I.G., Lau, Y.L., Mitchell, C. (2001). The effect of depositional history on contaminated bed sediment stability. *Science of the Total Environment*, **266**(1): 7-13.

Droppo, I.G., Nackaerts, K., Walling, D.E., Williams, N. (2005a). Can flocs and water stable soil aggregates be differentiated within fluvial systems? *Catena,* **60**(1): 1-18.

Droppo, I.G., Leppard, G.G., Liss, S.N., Milligan, T.G. (2005b). Opportunities, needs, and strategic direction for research on flocculation in natural and engineered systems. In I.G. Droppo, G.G. Leppard, S.N. Liss, T.G. Milligan (Eds.), *Flocculation in Natural and Engineered Environmental Systems* (pp. 1-22.). London: CRC Press.

Droppo, I.G., D'Andrea, L., Krishnappan, B.G., Jaskot, C., Trapp, B., Basuvaraj, M., Liss, S.N. (2014). Fine-sediment dynamics: towards an improved understanding of sediment erosion and transport. *Journal of Soils and Sediments*, **15**(2): 467-479.

Dufek, M. (2005). Auto Slice & View (2nd edn.). FEI Company, 14 pp.

Visualization Sciences Group (2015). Avizo 9 Users' Guide. FEI Company, SAS and Konrad-Zuse-Zentrum für Informationstechnik Berlin (ZIB).

Duliu, O.G. (1999). Computer axial tomography in geosciences: an overview. *Earth-Science Reviews*, **48**: 265 - 281.

Dyer, K.R. (1986). *Coastal and Estuarine Sediment Dynamics*. Chichester: John Wiley and Sons.

Dyer, K.R. (1989). Sediment processes in estuaries: future research requirements. *Journal of Geophysical Research*, **94**: 14327-14339.

Dyer, K.R., Manning, A.J. (1999). Observation of the size, settling velocity and effective density of flocs, and their fractal dimensions. *Journal of Sea Research*, **41**(1): 87-95.

Dyer, K.R., Cornelisse, J.M., Dearnaley, M., Jago, C., Kappenburg, J., McCave, I.N., Pejrup, M., Puls, W., Van Leussen, W., Wolfstein, K. (1996). A comparison of in-situ techniques for estuarine floc settling velocity measurements. *Journal of Sea* Research, **36**: 15-29.

Dyer, K.R., Bale, A.J., Christie, M.C., Feates, N., Jones, S. and Manning, A.J. (2002). The turbidity maximum in a mesotidal estuary, the Tamar Estuary, UK. Part II: The floc properties. In J.C. Winterwerp, C. Kranenburg (Eds.), *Fine Sediment Dynamics in the Marine Environment - Proceedings in Marine Science* 5 (pp. 219-232). Amsterdam: Elsevier.

Eisma, D. (1986). Flocculation and de-flocculation of suspended matter in estuaries. *Netherlands Journal of Sea Research*, **20**(1-2): 183-199.

Eisma, D., Boon, J., Groenewegen, R., Ittekkot, V., Kalf, J., Mook, W.G. (1983). Observations on macro-aggregates, particle size and organic composition of suspended

matter in the Ems estuary. *Mitteilungen aus dem Geologisch-Paläontologischen Institut der Universität Hamburg*. SCOPE/UNEP Sonderbereich, **55**: 295-314.

Eisma, D., Bale, A.J., Dearnaley, M.P., Fennessy, M.J., Van Leussen, W., Maldiney, M.-A., Pfeiffer, A., Wells, J.T. (1986). Intercomparison of *in situ* suspended matter (floc) size measurements. *Journal of Sea Research*, **36**(1-2): 3-14.

Eisma, D., Schuhmacher, T., Boekel, H., Van Heerwaarden, J., Franken, H., Lann, M., Vaars, A., Eijgenraam, F., Kalf, J. (1990) A camera and image analysis system for *in situ* observation of flocs in natural waters. *Netherlands Journal of Sea Research*, **27**: 43-56.

Elliott, A.V.C., Plach, J.M., Droppo, I.G., Warren, L.A. (2012). Comparative floc-bed sediment trace element portioning across variably contaminated aquatic ecosystems. *Environmental Science & Technology*, **46**: 209-216.

Engel, A. (2000). The role of transparent exopolymer particles (TEP) in the increase in apparent particle stickiness (α) during the decline of a diatom bloom. *Journal of Plankton Research*, **22**: 485-497.

Filella, M., Buffle, J., Leppard., G.G. (1993). Characterization of submicrometre colloids in freshwaters: evidence for their bridging by organic structures: *Water Science and Technology*, **27**(11): 91-102.

Frølund, B., Palmgren, R., Keiding, K., Nielsen, P.H. (1996). Extraction of extracellular polymers from activated sludge using a cation exchange resin. *Water Research*, **30**: 1749-1758.

Frösch, D., Westphal, C. (1989). Melamine resins and their application in electron microscopy. *Electron microscopy reviews*, **2**(2): 231-255.

Fortin, D., Leppard, G.G. Tessier, A. (1993). Characteristics of lacustrine diagenetic iron oxyhydroxides. *Geochimica et Cosmochimica Acta*, **57**: 4391-4404.

Furukawa, Y., Watkins, J.L., Kim, J., Curry, K.J., Bennett. R.H. (2009). Aggregation of montmorillonite and organic matter in aqueous media containing artificial seawater. *Geochemical Transactions*, **10**(1): 1-11.

Furukawa, Y., Reed, A.H., Zhang, G. (2014). Effect of organic matter on estuarine flocculation: a laboratory study using montmorillonite, humic acid, xanthan gum, guar gum and natural estuarine flocs. *Geochemical Transactions*, **15**(1): 1-9.

Garcia-Aragon, J., Droppo, I.G., Krishnappan, B.G., Trapp, B., Jaskot, C. (2011). Erosion characteristics and floc strength of Athabasca River cohesive sediments: towards managing sediment-related issues. *Journal of Soils & Sediments*, **11**: 679-689.

Geesey, G.G. (1982). Microbial exopolymers: ecological and economic considerations. *ASM News*, **48**: 9-14.

Gehr, R., Henry, J.G. (1983). Removal of extracellular material techniques and pitfalls. *Water Research*, **17**(12): 1743-1748.

Gerbersdorf, S.U., Westrich, B., Paterson, D.M. (2009). Microbial extracellular polymeric substances (EPS) in fresh water sediments. *Microbial Ecology*, **58**: 334-349.

Gibbs, R.J., Konwar, L. (1986). Coagulation and settling of Amazon River sediment. *Continental Shelf Research*, **6**: 127-148.

Gillott, J.E. (1987). *Clay in Engineering Geology*. Amsterdam: Elsevier

Glauert, A.M. (1987). *Fixation, dehydration and embedding of biological specimens.* Amsterdam: Elsevier.

Goldstein, J., Newbury, D., Joy, D., Lyman, C., Echlin, P., Lifshin, E., Sawyer, L., Michael, J. (2007). *Scanning Electron Microscopy and X-ray Microanalysis, a text for biologists, materials scientists and geologists* (3rd edn). New York, NY: Plenum Press.

Goodhew, P.J., Humphreys, J., Beanland, R. (2000). *Electron microscopy and analysis* (3rd edn). London: Taylor & Francis.

Grabowski, R.C., Droppo, I.G., Wharton, G. (2011). Erodibility of cohesive sediment: The importance of sediment properties. *Earth-Science Reviews*, **105**: 101-120.

Gregory, J. (1978). Flocculation by inorganic salts. In K. J. Ives (Ed.), *The Scientific Basis of Flocculation*, (pp. 89-99). Alphen aan den Rijn, NL: Sijthoff & Noordhoff.

Grim, R.E. (1968). *Clay Mineralogy*. New York, NY: McGraw-Hill Book Company.

Handschuh, S., Baeumler, N., Schwaha, T., Ruthensteiner, B. (2013). A correlative approach for combining microCT, light and transmission electron microscopy in a single 3D scenario. *Frontiers in Zoology*, **10**: 1-16.

Hayat, M. (1981). *Fixation for electron microscopy*: London: Academic Press.

Heissenberger, A., Leppard, G.G., Herndl, G.J. (1996a). Relationship between the intracellular integrity and the morphology of the capsular envelope in attached and free-living marine bacteria. *Applied and Environmental Microbiology*, **62**: 4521-4528.

Heissenberger, A., Leppard, G.G., Herndl, G.J. (1996b). Ultrastructure of marine snow. 11. Microbiological considerations. *Marine Ecology Progress Series*, **135**: 299-308.

Hemes, S., Desbois, G., Urai, J.L., Schröppel, B., Schwarz, J-O. (2015). Multi-scale characterization of porosity in Boom Clay (HADES-level, Mol, Belgium) using a combination of X-ray m-CT, 2D BIB-SEM and FIB-SEM tomography. *Microporous and Mesoporous Materials*, **208**: 1-20.

Hill, P.S. (1996). Sectional and discrete representations of floc breakage in agitated suspensions. *Journal of Deep Sea Research*, **43**: 679-702.

Hill, P.S., Voulgaris, G., Trowbridge, J.H. (2001). Controls on floc size in a continental shelf bottom boundary layer. *Journal of Geophysical Research*, **106**(C5): 9543-9549.

Hobson, D.M., Carter, R.M., Yan, Y. (2009). Rule based concave curvature segmentation for touching rice grains in binary digital images. In *IEEE Instrumentation and Measurement Technology Conference,* 1685-1689.

Hodder, K.R. (2009). Flocculation: a key process in the sediment flux of a large, glacier-fed lake. *Earth Surface Processes and Landforms*, **34**(8): 1151-1163.

Hodder, K.R. Gilbert, R. (2009). Evidence for flocculation in glacier-fed Lillooet Lake, British Columbia. *Water Research*, **41**(12): 2748-2762.

Holzer, L., Indutnyi, F., Gasser, P.H., Münch, B., Wegmann, M. (2004). Three-dimensional analysis of porous BaTiO3 ceramics using FIB nanotomography. *Journal of Microscopy*, **216**(1): 84-95.

Holzer, L.H., Münch, B., Wegmann, M., Gasser, P., Flatt, R.J. (2006). FIB-nanotomography of particulate systems-Part I: Particle shape and topology of interfaces. *Journal of the American Ceramic Society*, **89**(8): 2577-2585.

Holzer, L., Gasser, P.H., Kaech, A., Wegmann, M., Zingg, A., Wepf, R., Münch, B. (2007). Cryo-FIB-nanotomography for quantitative analysis of particle structures in cement suspensions. *Journal of Microscopy*, **227**(3): 216-228.

Holzer, L., Münch, B., Rizzi, M., Wepf, R., Marschall, P., Graule, T. (2010). 3D-microstructure analysis of hydrated bentonite with cryo-stabilized pore water. *Applied Clay Science*, **47**(3-4): 330-342.

Houben, M.E., Desbois, G., Urai, J.L. (2013). Pore morphology and distribution in the shaly facies of Opalinus Clay (Mont Terri, Switzerland): Insights from representative 2D BIB–SEM investigations on mm to nm scale. *Applied Clay Science*, **71**: 82-97.

Houben, M.E., Desbois, G., Urai, J.L. (2014). A comparative study of representative 2D microstructures in shaly and Sandy facies of Opalinus Clay (Mont Terri, Switzerland) inferred form BIB-SEM and MIP methods. *Marine and Petroleum Geology*, **49**: 143-161.

Hunter, K.A., Leonard, M.W. (1988). Colloid stability and aggregation in estuaries: 1. Aggregation kinetics of riverine dissolved iron after mixing with seawater. *Geochimica et Cosmochimica Acta*, **55**(5): 1123-1130.

Hunter, R.J. (2001). Foundations of Colloid Science (2nd edn). Oxford: Oxford University Press.

Jarvis, P., Jefferson, B., Gregory, J., Parsons, S.A. (2005). A review of floc strength and breakage. *Water Research*, **39**(14): 3121-3137.

Jenkins, D., Richard, M.G., Daigger, G.T. (1993). *Manual on the cause and control of sludge bulking and foaming* (2nd edn). Boca Raton, FL: Lewis Publishers.

Johnson, C.P., Li, X., and Logan, B.E. (1996). Settling velocities of fractal aggregates. *Environmental Science & Technology*, **30**: 1911-1918.

Jorand, F., Zartarian, F., Thomas, F., Block, J.C., Bottero, J.Y., Villemin, G., Urbain, V., Manem, J. (1995). Chemical and structural (2D) linkage between bacteria within activated sludge flocs. *Water Research*, **29**(7): 1639-1647.

Jung, A.-V., Chanudet, V., Ghanbaja, J., Lartiges, B.S., Bersillon, J.-L. (1995). Coagulation of humic substances and dissolved organic matter with a ferric salt: An electron energy loss spectroscopy investigation. *Water Research*, **39**(16): 3849-3862.

Keller, L.M., Holzer, L., Wepf, R., Gasser, P. (2011). 3D geometry and topology of pore pathways in Opalinus clay: Implications for mass transport. *Applied Clay Science*, **52**(1-2): 85-95.

Keller, L.M., Holzer, L., Wepf, R., Gasser, P., Münch, B., Marschall, P. (2011). On the application of focused ion beam nanotomography in characterizing the 3D pore space geometry of Opalinus clay. *Physics & Chemistry of the Earth*, **36**(17-18): 1539 – 1544.

Keller, L.M., Schuetz, P., Erni, R., Rossell, M., Lucas, F., Gasser, P., Holzer, L. (2013). Characterization of multi-scale microstructural features in Opalinus Clay. *Microporous and Mesoporous Materials*, **170**(C): 83-94.

Ketcham, R.A. (2005). Improved methods for quantitative analysis of three-dimensional porphyroblastic textures. *Geosphere*, **1**(1): 32-41.

Ketcham, R.A., Carlson, W.D. (2001). Acquisition, optimization and interpretation of X-ray computed tomographic imagery: applications to the geosciences. *Computers & Geosciences*, **27**: 381-400.

Kettridge, N., Binley, A. (2008). X-ray computed tomography of peat soils: measuring gas content and peat structure. *Hydrological Processes*, **22**(25): 4827-4837.

Khelifa, A., Hill, P.S. (2006). Models for effective density and settling velocity of flocs. *Journal of Hydraulic Research*, **44**(3): 390-401.

Kim, J.-W., Furukawa, W., Dong, H., Newell, S.W. (2005). The role of microbial Fe(III) reduction in the clay flocculation. *Clays and Clay Minerals*, **53**: 572-579.

Kim, J., Furukawa, Y., Curry, K.J., Bennett R.H. (2012). Role of Chitin in montmorillonite fabric: Transmission electron microscope observations. *Clays and Clay Minerals*, **60**(1): 89-98.

Klimpel, R.C., Hogg, R. (1986). Effects of flocculation conditions on aggregate structure. *Journal Colloid Interface Science*, **113**: 121-131.

Kranenburg, C. (1994). On the fractal structure of cohesive sediment aggregates. *Continental and Shelf Science*, **39**(6): 451-460.

Kranenburg, C. (1999). Effects of floc strength on viscosity and deposition of cohesive sediment suspensions. *Continental Shelf Research*, **19**: 1665-1680.

Krank, K., Milligan, T.G. (1992). Characteristics of suspended particles at an 11-hour anchor station in San Francisco Bay, California. *Journal of Geophysical Research*, **97**: 11373-11382.

Krone, R.B. (1962). Flume studies of the transport of sediment in estuarial shoaling processes. *Hydraulic Engineering Laboratory and Sanitary Engineering Research Laboratory*, University of California, Berkeley. Final Report.

Krone, R.B. (1963). A study of rheological properties of estuarial sediments. Report prepared for the Committee on Tidal Hydraulics under contract DA-22-079-CIVENG-61-7 with Waterways Experiment Station, Corps of Engineers, US Army.

Krone, R.B. (1978). Aggregation of suspended particles in estuaries. In B. Kjerfve (Ed.), *Estuaries Transport Processes*. Columbia, SC: University of South Carolina Press.

Krone, R.B. (1986). The significance of aggregate properties to transport processes. In A.J. Mehta (Ed.), *Estuarine Cohesive Sediment Dynamics*. Berlin: Springer-Verlag.

Lambe, T.W. (1953). The structure of inorganic soil. *Proceedings of the American Society of Civil Engineers*, **79**: 1-49.

Lawrence, J.R., Swerhorne, G.D.W., Leppard, G.G., Araki, T., Zhang, X., West, M.M., Hitchcock, A.P. (2003). Scanning transmission X-ray, laser scanning, and transmission electron microscopy mapping of the exopolymeric matrix of microbial biofilms. *Applied and Environmental Microbiology*, **69**: 5543-5554.

Lee, B.J., Toorman, E., Molz, F.J., Wang, J. (2011). A two-class population balance equation yielding bimodal flocculation of marine or estuarine sediments. *Water Research*, **45**(5): 2131-2145.

Leppard, G.G. (1992a). Evaluation of electron microscope techniques for the description of aquatic colloids. In J. Buffle, H.P. van Leeuwen (Eds.), *Environmental particles* (Vol. 1) (pp. 231-289). Boca Raton, FL: Lewis Publishers.

Leppard, G.G. (1992b). Size, morphology and composition of particulates in aquatic ecosystems: solving speciation problems by correlative electron microscopy. *The Analyst*, **117**(3): 595-603.

Leppard, G.G. (1993). Organic flocs in surface waters: their native state and aggregation behavior in relation to contaminant dispersion. In S.S. Rao (Ed.), *Particulate matter and aquatic contaminants* (pp. 169-195). Boca Raton, FL: Lewis Publishers.

Leppard, G.G. (1997). Colloidal organic fibrils of acid polysaccharides in surface waters: Electron-optical characteristics, activities and chemical estimates of abundance. *Colloids and Surfaces A: Physicochemical and Engineering Aspects*, **120**(1-2): 1-3.

Leppard, G.G., Droppo, I.G. (2005). Overview of flocculation processes in freshwater ecosystems. In I.G. Droppo, G.G. Leppard, S.N. Liss, T.G. Milligan (Eds.), *Flocculation in Natural and Engineered Environmental Systems* (pp. 1-22). London: CRC Press.

Leppard, G.G., De Vitre, R.R., Perret, D., Buffle, J. (1989). Colloidal iron oxyhydroxy-phosphate: The sizing and morphology of an amorphous species in relation to partitioning phenomena. *Science of the Total Environment*, **87/88**: 345-354.

Leppard, G.G., Burnison, K.B., Buffle. J. (1990). Transmission electron microscopy of the natural organic matter of surface waters. *Analytica Chimica Acta*, **232**: 107-121.

Leppard, G.G., Heissenberger, A., Herndl, G.J. (1996). Ultrastructure of marine snow. I. Transmission electron microscopy methodology. *Marine Ecology Progress Series*, **135**: 289-298.

Leppard, G.G., West, M.M., Flannigan, D.T., Carson, J., Lott, J.N. (1997). A classification scheme for marine organic colloids in the Adriatic Sea: Colloid speciation by transmission electron microscopy. *Canadian Journal of Fisheries and Aquatic Sciences*, **54**(10): 2334-2349.

Leppard, G.G., Flannigan, D.T., Mavrocordatos, D., Marvin, C.H., Bryant, D.W., McCarry, B.E. (1998). Binding of polycyclic aromatic hydrocarbons by size classes of particulate in Hamilton Harbor water. *Environmental science & technology*, **32**(22): 3633-3639.

Leppard, G.G., Droppo, I.G., West, M.M., Liss, S.N. (2003). Compartmentalization of metals within the diverse colloidal matrices comprising activated sludge microbial flocs. *Journal of Environmental Quality*, **32**(6): 2100-2108.

Li, D.-H., Ganczarczyk, J.J. (1987). Stroboscopic determination of settling velocity, size, porosity of activated sludge flocs. *Water Research*, **21**(3): 257-262.

Li, D.-H., Ganczarczyk, J.J. (1989). Fractal geometry of particle aggregated in water and waste water treatment processes. *Environmental Science & Technology*, **23**(11): 1385-1389.

Li, X., Logan, B.E. (1995). Size distributions and fractal properties of particles during a simulated phytoplankton bloom in a mesocosm. *Deep-Sea Research Part II: Topical Studies in Oceanography*, **42**(1): 125-138.

Limaye, A. (Oct 2006). *Drishti - Volume Exploration and Presentation Tool*. Poster presentation, IEEE Vis 2006, Baltimore, MD.

Liss, S.N. (2002). Microbial Flocs Suspended Biofilms. In G. Bitton (Ed.), *Encyclopaedia of Environmental Microbiology* (Vol. 4) (pp. 2000-2012). New York, NY: John Wiley and Sons.

Liss, S.N., Droppo, I.G., Flannigan, D.T., Leppard, G.G. (1996). Floc architecture in wastewater and natural riverine systems. *Environmental Science & Technology*, **30**(2): 680-686.

Liss, S. N., Milligan, T. G., Droppo, I. G., Leppard, G. G. (2004). Methods for Analyzing Floc Properties. In I.G. Droppo, G.G. Leppard, S.N. Liss, T.G. Milligan (Eds.), *Flocculation in Natural and Engineered Environmental Systems* (pp. 1-22). London: CRC Press.

Logan, B.E., Wilkinson, D.B. (1991). Fractal dimensions and porosities of Zooglea ramigera and Saccharomyces cerevisiae aggregates. *Biotechnology and Bioengineering*, **38**: 389-396.

Long, H., Swennen, R., Foubert, A., Dierick, M., Jacobs, P.J.S. (2009). 3D quantification of mineral components and porosity distribution in Westphalian C sandstone by microfocus X-ray computed tomography. *Sedimentary Geology*, **220**(1-2): 116-125.

Lubelli, B., de Winter, D.A.M., Post, J.A., van Hees, R.P.J., Drury, M.R. (2013). Cryo-FIB–SEM and MIP study of porosity and pore size distribution of bentonite and kaolin at different moisture contents. *Applied Clay Science*, **80**: 358-365.

Lucas, M.S., Günthert, M., Gasser, P., Lucas, F. Wepf, R. (2012). Bridging microscopes: 3D correlative light and scanning electron microscopy of complex biological structures. *Methods in Cell Biology*, **111**: 325–356.

Lundkvist, M., Gangelhof, U., Lunding, J., Flindt, M.R. (2007). Production and fate of extracellular polymeric substances produced by benthic diatoms and bacteria: a laboratory study. *Estuarine, Coastal and Shelf Science*, **75**(3): 337-346.

Maes, F., Collignon, A., Vandermeulen, D., Marchal, G., Suetens, P. (1997). Multimodality image registration by maximization of mutual information. *IEEE Transactions on Medical Imaging*, **16**(2): 187-198.

Maerza, J., Verneyb, R., Wirtzc, K., Feudela, U. (2011). Modeling flocculation processes: Intercomparison of a size class-based model and a distribution-based model. *Continental Shelf Research*, **31**(10): S84-S93.

Mahendran, B., Lishman, L., Liss, S.N. (2012). Structural, physicochemical and microbial properties of flocs and biofilms in integrated fixed-film activated sludge (IFFAS) systems. *Water Research*, **46**(16): 5085-5101.

Maire, E., Withers, P.J. (2014). Quantitative X-ray tomography. *International Materials Reviews*, **59**(1): 1-43.

Manning, A.J. (2001). *A study of the effects of turbulence on the properties of flocculated mud*. (Ph.D. Thesis). Institute of Marine Studies, University of Plymouth.

Manning, A.J. (2004). The observed effects of turbulence on estuarine flocculation. In P. Ciavola, M. B. Collins (Eds.), *Journal of Coastal Research, Special Issue 41. Sediment Transport in European Estuaries: Proceedings of the STRAEE Workshop* (pp. 90-104).

Manning, A.J., Dyer, K.R. (1999). A laboratory examination of floc characteristics with regard to turbulent shearing. *Marine Geology*, **160**(1): 147-170.

Manning, A.J., Dyer, K.R. (2002a). The use of optics for the in situ determination of flocculated mud characteristics. *Journal of Optics, A: Pure and Applied Optics*, **4**: 71-81.

Manning, A.J., Dyer, K.R. (2002b). A comparison of floc properties observed during neap and spring tidal conditions. In J. Winterwerp, C. Kranenburg (Eds.), *Proceedings in Marine Science* (Vol. 5) (pp. 233-250). Amsterdam: Elsevier.

Manning, A.J., Dyer, K.R. (2007). Mass settling flux of fine sediments in Northern European estuaries: Measurements and predictions. *Marine Geology* **245** (1-4): 107-122.

Manning, A. J., Schoellhamer, D. H. (2013). Factors controlling floc settling velocity along a longitudinal estuarine transect. *Marine Geology*, **345**: 266-280.

Manning, A.J., Langston, W.J., Jonas, P.J.C. (2010). A review of sediment dynamics in the Severn Estuary: Influence of flocculation. *Marine Pollution Bulletin*, **61**(1-3): 37-51.

Manning, A.J., Baugh, J.V., Soulsby, R.L., Spearman, J.R., Whitehouse, R.J.S. (2011). Cohesive sediment flocculation and the application to settling flux modelling. In S.S. Ginsberg (Ed.), *Sediment Transport* (pp. 91-116). InTech Open Access Publisher.

Available from: http://www.intechopen.com/books/sediment-transport/cohesive-sediment-flocculation-and-the-application-tosettling-flux-modelling.

Manning, A.J., Spearman, J.R., Whitehouse, J.R.S., Pidduck, E.L., Baugh, J.V., Spencer, K.L. (2013). Flocculation dynamics of mud: Sand mixed suspensions. In A.J. Manning (Ed.), *Sediment transport processes and their modelling applications* (pp. 120-164). In Tech Open Access Publisher. Available from: http://www.intechopen.com/ books/sediment-transport-processes-and-their-modelling-applications/flocculation-dynamics-of-mud-sand-mixed-suspensions.

Martins, A.M.P., Pagilla, K., Heijnen, J.J., van Loosdrecht, M.C.M. (2004). Filamentous bulking sludge - a critical review. *Water Research*, **38**(4): 793-817.

Marxsen, J. (1988). Investigations into the number of respiring bacteria in groundwater from sandy and gravelly deposits. *Microbial Ecology*, **16**: 65-72.

Mavrocordatos, D., Lienemann, C-P., Perret, D. (1994). Energy filtered transmission electron microscopy for the physico-chemical characterization of aquatic submicron colloids. *Water Science and Technology*, **117**(1): 39-47.

Mavrocordatos, D., Perret, D., Leppard. G.G. (2007). Strategies and Advances in the Characterisation of Environmental Colloids by Electron Microscopy. In K.J. Wilkinson, J.R. Lead (Eds.), *Environmental colloids and particles: Behaviour, separation and characterisation* (pp. 345-404). Chichester, UK: John Wiley & Sons.

McConnachie, J.M., Petticrew, E.L., 2004. Hydrological and biological event based variability in the fine-grained sediment structure of a small undisturbed catchment. In V. Golosov, V. Belyaev, D.E. Walling (Eds.), *Sediment Transfer through the Fluvial System* (pp. 459-465). Wallingford: International Association of Hydrological Sciences Publication, No. 288.

Mees, F., Swennen, R., Van Geet, M., Jacobs, P. (2003). Applications of X-ray computed tomography in the geosciences. *Geological Society, London, Special Publications*, **215**(1), 1-6.

Mehta, A.J., Lott, J.W. (1987). Sorting of fine sediment during deposition. Proceedings of the *Conference on Advances in Understanding Coastal Sediment Processes*, **1**: 348-362.

Mehta, A.J., Partheniades, E.P. (1982). Resuspension of deposited cohesive sediment beds. *Coastal Engineering Proceedings*, **1**(18): 1569-1588.

Mehta, A.J., Manning, A.J., Khare, Y.P. (2014). A note on the Krone deposition equation and significance of floc aggregation. *Marine Geology*, **354**: 34-39.

Mikkelsen, O.A., Milligan, T.G., Hill, P.S., Moffatt, D. (2004). INSSECT-an instrumented platform for floc measurements close to the seabed. *Limnology and Oceanography, Methods*, **2**: 226-236.

Mikkelsen, O.A., Hill, P.S., Milligan, T.G., Chant, R.J. (2005). In situ particle size distributions and volume concentrations from a LISST-100 laser particle sizer and a digital floc camera. *Continental Shelf Research*, **25**: 1959-1978.

Mikkelsen, O.A. Hill, P.S., Milligan, T.G. (2006). Single-grain, microfloc and macrofloc volume variations observed with a LISST-100 and a digital floc camera. *Journal of Sea Research*, **55**(2): 87-102.

Milligan, T.G., Hill, P.S. (1998). A laboratory assessment of the relative importance of turbulence, particle composition, and concentration in limiting maximal floc size and settling behaviour. *Journal of Sea Research*, **39**(3): 227-241.

Milligan, T.G., Hill, P.S., Law, B.A. (2007). Flocculation and the loss of sediment from the Po River plume. *Continental Shelf Research*, **27**(3): 309-321.

Mitchell, J.K., Soga, K. (2005). *Fundamentals of Soil Behaviour* (3rd edn). Chichester, UK: John Wiley and Sons.

Möbus, G., Inkson, B.J. (2007). Nanoscale tomography in materials science. *Materials Today*, **10**(12): 18-25.

Moon, C.F. (1972). The microstructure of clay sediments. *Earth-Science Reviews*, **8**: 303-21.

Moss, A.J., Green, P. (1983). Movement of solids in air and water by raindrop impact. Effects of drop-size and water-depth variations. *Australian Journal of Soil Research*, **21**: 257-269.

Münch, B., Gasser, P., Holzer, L., Flatt, R.J. (2006). FIB-nanotomography of particulate systems - Part II: Particle recognition and effect of boundary truncation. *Journal of the American Ceramic Society*, **89**(8): 2586-2595.

Münch, B., Trtik, P., Marone, F., Stampanoni, M. (2009) Stripe and ring artifact removal with combined wavelet - Fourier filtering. *Optics Express*, **17**: 8567-8591.

Murphy, G.E., Narayan, K., Lowekamp, B.C., Hartnell, L.M., Heymann, J.A.W., Fu, J., Subramaniam, S. (2011). Correlative 3D imaging of whole mammalian cells with light and electron microscopy. *Journal of Structural Biology*, **176**(3): 268-278.

Myklestad, S.M. (1995). Release of extracellular products by phytoplankton with special emphasis on polysaccharides. *Science of the total Environment*, **165**: 155-164.

Nguyen, T. P., Hankins, N. P., Hilal, N. (2007). A comparative study of the flocculation behaviour and final properties of synthetic and activated sludge in wastewater treatment. *Desalination*, **204**(1): 277-295.

Orloff, J., Utlaut, M., Swanson, L. (2003). *High resolution Focused Ion Beams: FIB and its applications*. New York, NY: Kluwer Academic/Plenum Publishers.

Orsi, T.H., Edwards, C.M., Andersron, A.L., (1994). X-ray computed tomography: a nondestructive method for quantitative analysis of sediment cores. *Journal of Sediment. Research*, **64**: 690-693.

Palomino, A.M., Kim, S., Summitt, A., Fratta, D. (2011). Impact of diatoms on fabric and chemical stability of diatom–kaolin mixtures. *Applied Clay Science*, **51**(3): 287-294.

Partheniades E.P. (1986). Turbidity and cohesive sediment dynamics. In E.P. Partheniades, J. C. J. Nihoal (Eds.), *Marine interface ecohydrodynamics* (pp. 515-550). Amsterdam: Elsevier.

Partheniades, E.P. (2007). *Engineering Properties and Hydraulic Behavior of Cohesive Sediments*. Boca Raton, FL: CRC Press.

Passow, U. (2002). Transparent exopolymer particles (TEP) in aquatic environments. *Progress in Oceanography*, **55**: 287-333.

Paterson, D.M. (1997). Biological mediation of sediment erodibility: Ecology and physical dynamics. In N. Burt, R. Parker, J. Watts (Eds.), *Cohesive Sediments* (pp. 215-229). Chichester, UK: John Wiley & Sons.

Paterson, D.M., Hagerthey, S.E. (2001). Microphytobenthos in contrasting coastal ecosystems: Biology and dynamics. In K. Reise (Ed.) *Ecological comparisons of sedimentary shores* (pp.105-125). New York, NY: Springer.

Patterson, B.M., Escobedo-Diaz, J.P., Dennis-Koller, D., Cerreta, E. (2012). Dimensional quantification of embedded voids or objects in three dimensions using X-ray tomography. *Microscopy and Microanalysis*, **18** (2): 390-398.

Peddie, C.J., Collinson, L.M. (2014). Exploring the third dimension: Volume electron microscopy comes of age. *Micron*, **61**: 9-19.

Plach, J.M., Elliott, A.V.C., Droppo, I.G., Warren, L.A. (2011). Physical and Ecological Controls on Freshwater Floc Trace Metal Dynamics. *Environmental & Science Technology*, **45**: 2157-2164.

Poesen, J.W., Vandaele, K., Van Wesemael, B. (1996). Contribution of gully erosion to sediment production on cultivated lands and rangelands. In D.E. Walling, B.W. Webb, (Eds.) *Erosion and Sediment Yield: Global and Regional Perspectives* (pp. 251-266). Wallingford: International Association for Hydrological Sciences Publication, No. 236.

Preibisch, S., Saalfeld, S., Tomancak, P. (2009). Globally optimal stitching of tiled 3D microscopic image acquisitions. *Bioinformatics*, **25**(11): 1463-1465.

Ransom, B., Bennett, R.H., Baerwald, R., Shea, K. (1997). TEM study of in situ organic matter on continental margins: occurrence and the "monolayer" hypothesis. *Marine Geology*, **138**: 1-9.

Ransom, B., Shea, K.F., Bennett, R.H., Baerwald, R. (1998). Comparison of pelagic and nepheloid layer marine snow: implications for carbon cycling. *Marine Geology*, **150**: 39-50.

Ransom, B., Bennett, R.H., Baerwald, R., Hulbert, M.H., Burkett, P.-J. (1999). In situ conditions and interactions between microbes and minerals in fine-grained marine sediments: A TEM microfabric perspective. *American Mineralogist*, **84**: 183-192.

Ray, A. (2011). *CT Pro User Manual*. Nikon Metrology, Hertfordshire, UK.

Remeysen, K., Swennen, R. (2008). Application of microfocus computed tomography in carbonate reservoir characterization: possibilities and limitations. *Marine and Petroleum Geology*, **25**(6): 486-499.

Righetti, M., Lucarelli, C. (2010). Resuspension phenomena of benthic sediments: the role of cohesion and biological adhesion. *River Research and Applications*, **26**: 404-413.

Rogerson, A., Anderson, R.O., Vogel, C. (2003). Are planktonic naked amoebae predominately floc associated or free in the water column? *Journal of Plankton Research*, **25**: 1359-1365.

Rohr, K., Stiehl, H.S., Sprengel, R. (2001). Landmark-based elastic registration using approximating thin-plate splines. *Medical Imaging*, **20**(6): 526-534.

Sabatini, D.D., Bensch, K., Barrnett, R.J. (1963). Cytochemistry and electron microscopy. The preservation of cellular ultrastructure and enzymatic activity by aldehyde fixation. *Journal of Cell Biology*, **17**(1): 19-58.

Sanin, F.D., Vesilind, P.A. (1994) Effect of centrifugation on the removal of extracellular polymers and physical properties of activated sludge. *Water Science & Technology*, **30**(8): 117-127.

Schindelin, J., Arganda-Carreras, I., Frise, E., Kaynig, V., Longair, M., Pietzsch, T., Preibisch, S., Rueden, C., Saalfeld, S., Schmid, B., Tinevez, J-Y., White, D. J., Hartenstein, V., Eliceiri, K., Tomancak, P., Cardona, A. (2012). Fiji: an open-source platform for biological-image analysis. *Nature Methods*, **9**(7): 676-682.

Schindelin, J.; Rueden, C. T.; Hiner, M. C.; Eliceiri, K. W. The ImageJ ecosystem: An open platform for biomedical image analysis. Mol. Reprod. Dev. 2015, 82 (7-8), 518–529.

Schindler, R.J., Parsons, D.R., Ye, L., Hope, J.A., Baas, J.H., Peakall, J., Manning, A.J., Aspden, R.J., Malarkey, J., Simmons, S., Paterson, D.M., Lichtman, I.D., Davies, A.G.; Thorne, P.D., Bass, S.J. (2015). Sticky stuff: redefining bedform prediction in modern and ancient environments. *Geology*, **43**(5): 399-402.

Schiffbauer, J.D., Xiao, S. (2009). Novel application of focused ion beam electron microscopy (FIB-SEM) in preparation and analysis of microfossil ultrastructure: a new view of complexity in early Eukaryotic organisms. *Palaios*, **24**: 616-626.

Selomulya, C., Jia, X., Williams, R.A. (2005). Direct prediction of structure and permeability of flocculated structures and sediments using 3D tomographic imaging. *Chemical Engineering Research and Design*, **83**(7): 844-852.

Sezgin, M., Jenkins, D., Parker, D.S. (1978). A unified theory of filamentous activated sludge bulking. *Journal of the Water Pollution Control Federation*, **50**(2): 362-381.

Singh, H., Gokhale, A.M. (2005). Visualization of three-dimensional microstructures. *Materials Characterization*, **54**(1): 21-29.

Smart, P., Tovey, N.K. (1982). *Electron Microscopy of Soils and Sediments: Techniques*. Oxford: Oxford Science Publications.

Smith, D.J., Underwood, J.C. (1998). Exopolymer production by intertidal epipelic diatoms. *Limnology Oceanography*, **43**(7): 1578-1591.

Snidaro, D., Zartarian, F., Jorand, F., Bottero, J.-Y., Block, J.-C., Manem. J. (1997). Characterization of activated sludge flocs structure. *Water Science and Technology*, **36**: 313-320.

Soulsby, R.L., Manning, A.J., Spearman, J., Whitehouse, R.J.S. (2013). Settling velocity and mass settling flux of flocculated estuarine sediments. *Marine Geology*, **339**: 1-12.

Spencer, K.L., Manning, A.J., Droppo, I.G., Leppard, G.G., Benson, T. (2010). Dynamic interactions between cohesive sediment tracers and natural mud. *Journal of Soils and Sediments*, **10**(7): 1401-1414.

Spurr, A.R. (1969). A low viscosity epoxy resin embedding medium for electron microscopy. *Journal of Ultrastructure Research*, **26**: 31-43.

Stemmann, L., Eloire, D., Sciandra, A., Jackson, G.A., Guidi, L., (2008). Volume distribution for particles between 3.5 to 2000 μm in the upper 200 m region of the South Pacific Gyre. *Biogeosciences*, **5**: 299-310.

Stern, O. (1924). Zur Theorie der Elektrolytischen Doppelschriht. *Zeitschrift Electrochem*, **30**: 508-516.

Stolzenbach, K.D., Elimelich., M. (1994). The effect of density on collisions between sinking particles: implications for particle aggregation in the ocean. *Deep-Sea Research Part I: Oceanographic Research Papers*, **41**(3): 469-483.

Studer, D., Graber, W., Al-Amoudi, A., Eggli, P. (2001). A new approach for cryofixation by high-pressure freezing. *Journal of Microscopy*, **203**: 285-294.

Tambo, N., Watanabe, Y. (1979). Physical characteristics of flocs—I. The floc density function and aluminium floc. *Water Research*, **13**(5): 409-419.

Tan, X., Hu, L., Reed, A. H., Furukawa, Y., Zhang, G. (2014). Flocculation and particle size analysis of expansive clay sediments affected by biological, chemical, and hydrodynamic factors. *Ocean Dynamics*, **64**(1): 143-157.

Tang, P., Greenwood, J., Raper, J.A. (2002). A model to describe the settling behavior of fractal aggregates. *Journal of colloid and interface science*, **247**(1): 210-219.

ten Brinke, W.B.M. (1993). *The impact of biological factors on the deposition of fine-grained sediment in the Oosterschelde (The Netherlands)* (Ph.D. Thesis), Utrecht University.

Terzaghi, K. (1925). Erdbaumechanik auf Bodenphysikalischer Grundlage, Franz Deuticke, Leipzig und Wien.

Thévenaz, P., Ruttimann, U.E., Unser, M. (1998). A pyramid approach to subpixel registration based on intensity. *IEEE Transactions on Image Processing*, **7**(1): 27-41.

Thill, A., Wagner, M., Bottero, J.Y. (1999). Confocal scanning laser microscopy as a tool for the determination of 3D floc structure. *Journal of Colloid and Interface Science*, **220**: 465-467.

Tsai, C.H., Iacobellis, S., Lick, W. (1987). Flocculation of fine-grained lake sediments due to a uniform shear stress. *Journal of Great Lakes Research*, **13**(2): 135-146.

Uchic, M.D., Holzer, L., Inkson, B.J., Principe, E.L., Munroe, P. (2007). Three-dimensional microstructural characterization using focused ion beam tomography. *MRS Bulletin*, **32**(5): 408-416.

Uncles, R.J., Bale, A.J., Stephens, J.A., Frickers, P.E., Harris, C. (2010). Observations of floc sizes in a muddy estuary. *Estuarine, Coastal and Shelf Science*, **87**(2): 186-196.

Urbain, V., Block, J.C., Manem, J. (1993). Bioflocculation in activated sludge: an analytic approach. *Water Research*, **27**: 829-838.

Valioulis I.A. (1983). Particle collisions and coalescence in fluids. Report KH-R-44, CIT.

Van Geet, M., Swennen, R., Wevers, M. (2000). Quantitative analysis of reservoir rocks by microfocus X-ray computerised tomography. *Sedimentary Geology*, **132**(1): 25-36.

van Ledden, M. (2002) Fine Sediment Dynamics in the Marine Environment. In J. Winterwerp, C. Kranenburg (Eds.), *Proceedings in Marine Science* (Vol. 5) (pp.577-594). Amsterdam: Elsevier.

Van Leussen, W. (1988). Aggregation of particles, settling velocity of mud flocs. A review. In J. Dronkers, W. Van Leussen (Eds.), *Physical Processes in Estuaries* (pp. 347–403). Berlin: Springer-Verlag.

Verdugo, P., Alldredge, A.L., Azam, F., Kirchman, D.L., Passow, U., Santschi, P.H. (2004). The oceanic gel phase: a bridge in the DOM-POM continuum. *Marine Chemistry*, **92**: 67-85.

Verney, R., Lafite, R., Brun-Cottan, J. C. (2009). Flocculation potential of estuarine particles: the importance of environmental factors and of the spatial and seasonal variability of suspended particulate matter. *Estuaries and Coasts*, **32**(4): 678-693.

Verwey, E.J.W., Overbeek, J.T.G. (1948). *Theory of the Stability of Hydrophobic Colloids* New York, NY: Elsevier.

Visualization Sciences Group (2015). Avizo 9 Users' Guide. FEI, SAS and Konrad-Zuse-Zentrum für Informationstechnik Berlin (ZIB).

Volkert, C.A., Minor, A.M. (2007). Focused ion beam microscopy and micromachining. *MRS Bulletin*, **32**(5): 389-399.

Wall, G.J., Wilding, L.P., Smeck, N.E. 1978. Physical, chemical and mineralogical properties of fluvial unconsolidated bottom sediments in northwestern Ohio. *Journal of Environmental Quality*, **7**: 319-325.

Walling, D.E., Woodward, J.C., (2000). Effective particle size characteristics of fluvial suspended sediment transported by lowland British rivers. In M. Stone (Ed.), *Role of Erosion and Sediment Transport in Nutrient and Contaminant Transfer* (pp. 129–139). Wallingford: International Association for Hydrological Sciences Publication, No. 263.

Wang, H., Zhang, H., Ray, N. (2012). Clump splitting via bottleneck detection and shape classification. *Pattern Recognition*, **45**(7): 2780-2787

Ward, A.K., Johnson, M.D. (1996). Heterotrophic microorganisms. In F.R. Hauer, G. A. Lamberti (Eds.) *Methods in Stream Ecology* (pp. 233-268). San Diego, CA: Academic Press.

Webb, S.M., Leppard, G.G., Gaillard, J-F. (2000). Zinc speciation in a contaminated aquatic environment: Characterization of environmental particles by analytical electron microscopy. *Environmental Science & Technology*, **34**: 1926-1933.

Whitehouse, R.J.S., Soulsby, R., Roberts, W., Mitchener, H.J. (2000). *Dynamics of estuarine muds.* London: Thomas Telford Publications.

Wilkinson, K.J., Nègre, J-C., Buffle, J. (1995). Coagulation of colloidal material in surface waters: the role of natural organic matter. *Journal of Contaminant Hydrology*, **26**: 229-243.

Wilkinson, K.J., Stoll, S., Buffle, J. (1995). Characterization of NOM-colloid aggregates in surface waters: Coupling transmission electron microscopy staining techniques and mathematical modelling. *Fresenius' journal of analytical chemistry*, **351**(1): 54-61.

Williams, D.B., Carter, B.C. (2013). *Transmission electron microscopy: A text book for materials sciences*. New York, NY: Springer Science-Business Media.

Williams, N.D., Walling, D.E., Leeks, G.J.L. (2008). An analysis of the factors contributing to the settling potential of fine fluvial sediment. *Hydrological Processes*, **22**(20): 4153-4162.

Winterwerp, J.C. (1998). A simple model for turbulence induced flocculation of cohesive sediment. *Journal of Hydraulic Research*, **36** (3): 309-326.

Winterwerp, J.C., van Kesteren, W.G.M. (2004). Introduction to the physics of cohesive sediment in the marine environment. In T. van Loon (Ed.), *Developments in sedimentology*, 56. Amsterdam: Elsevier.

Woodward, J.C., Porter, P.R., Lowe, A.T., Walling, D.E. Evans, A.J. (2002). Composite suspended sediment particles and flocculation in glacial meltwaters: preliminary evidence from Alpine and Himalayan basins. *Hydrological processes*, **16**(9): 1735-1744.

Wotton, R.S. (2005). The essential role of exopolymers (EPS) in aquatic systems, oceanography and marine biology: an annual review. *Oceanography and Marine Biology*, **42**: 57-94.

Wu, R.M., Lee, D.J., Waite, T.D., Guan, J. (2002). Multi-level structure of sludge flocs. *Journal of Colloid and Interface Science*, **252**: 383-392.

Yallop, M.L., Paterson, D.M., Wellsbury, P. (2000). Interrelationships between rates of microbial production, exopolymer production, microbial biomass and sediment stability: biofilms of intertidal sediments. *Microbial Ecology*, **39**: 116-127.

Zahid, W.M., Ganczarczyk, J.J. (1990). Suspended solids in biological filter effluents. *Water Research*, **24**(2): 215-220.

Zarrelli, M., Skordos, A.A., Partridge, I.K. (2002). Investigation of cure induced shrinkage in unreinforced epoxy resins. *Plastics, Rubber and Composite Processing and Applications*, **31**: 377-384.

Zartarian, F., Mustin, C., Botteo, J.Y., Villemin, G., Thomas, F., Aillères, L., Champenois, M., Grulois, P., Manem, J. (1994). Spatial arrangement of the components of activated sludge flocs. *Water Science & Technology*, **30**: 243-250.

Zartarian, F., Mustin, C., Villemin, G., Ait-Ettager, T., Thill, A., Bottero, J.Y., Mallet, J.L., Snidaro, D. (1997). Three-dimensional modeling of an activated sludge floc. *Langmuir*, **13**: 35-40.

Zhang, T., Maire, E., Adrien, J., Onck, P. R., Salvo, L. (2013). Local tomography study of the fracture of an ERG metal foam. *Advanced Engineering Materials*, **15**(8): 767-772.

Zingg, A., Holzer, L., Kaech, A., Winnefeld, F., Pakusch, J., Becker, S., Gauckler, L. (2008). The microstructure of dispersed and non-dispersed fresh cement pastes – new insight by cryo-microscopy. *Cement and Concrete Research*, **38**(4): 522-529.

Appendices

Appendix I – Sample Site Location

As described in Section 2.2.1, floc samples were generated using natural estuarine sediment sourced from the Thames Estuary, SE England (Figure AI.1). Sediment samples were collected at Canvey Island by F. O'Shea in May 2013.

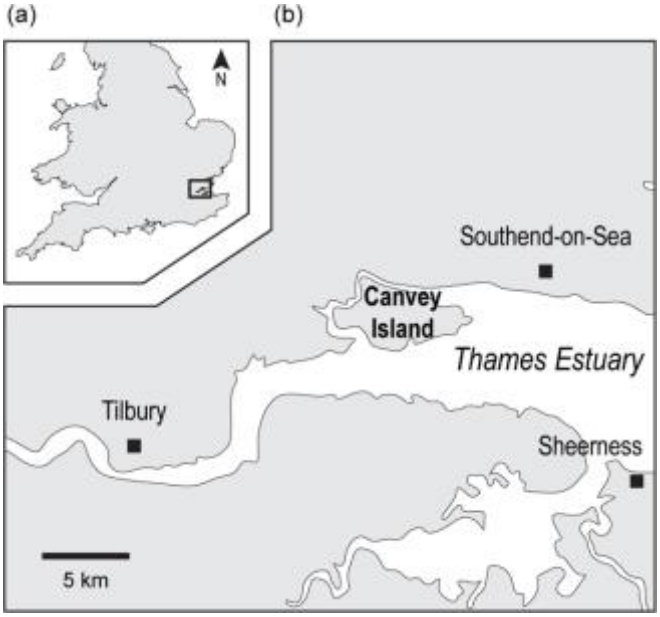

Figure AI.1. Map indicating the location of sampling site Canvey Island, Thames Estuary, SE England.

Appendix II– Stabilisation Procedure

In order to stabilise floc samples for multi-scale imaging a modified version of the preparation protocol developed by Deerinck *et al.* (2010) was employed. A flowchart outlining the steps taken during this procedure is shown in Figure AII.1.

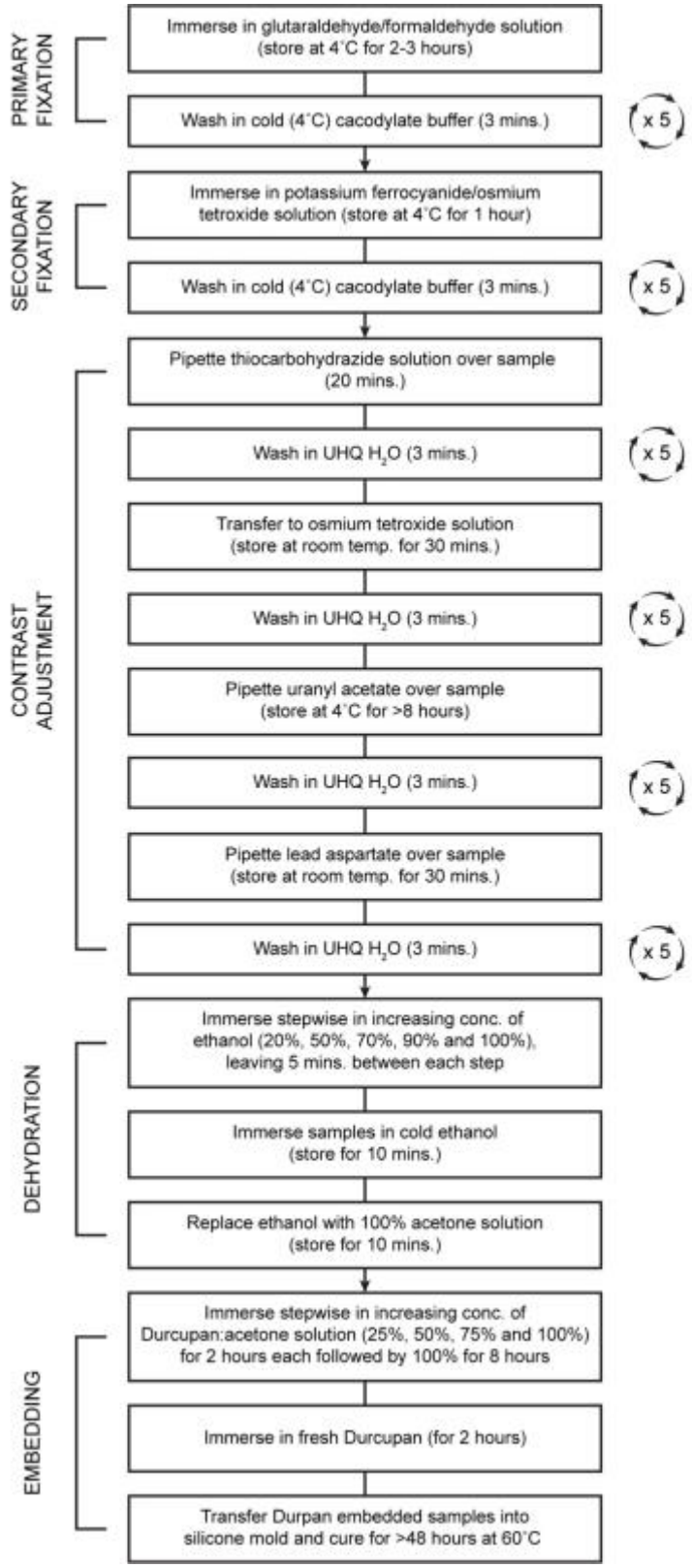

Figure AII.1. Flowchart outlining the steps taken in the stabilisation procedure. Sample stabilisation can be divided into five primary steps: 1) primary fixation, 2) secondary (or post) fixation, 3) contrast adjustment, 4) dehydration and 5) embedding.

Appendix III– Refining FIB-nt Volume Acquisition

III.a. Imaging Parameters

SEM imaging conditions were adjusted for each FIB-nt volume (Table 3.1) to optimise data quality and were determined as follows:

- *Accelerating Voltage (kV) and Current (nA)* – The accelerating voltage and current of the electron beam are key parameters for determining image contrast and resolution (Bushby *et al.*, 2011). For BSE imaging, a low beam voltage (3 – 5 kV) is desirable as this reduces the size of the interaction volume and depth from which BSEs are emitted thus improving image resolution. At low voltages, a high beam current is required (>4 nA) to impart sufficient intensity to the BSEs for improved image contrast and resolution (see Figure AIII.1).

- *Pixel Dimension* – A critical limiting factor for FIB-nt is the pixel density of images in SEM, which along with ion beam milling rate and dwell time influence data quality and volume acquisition time (Holzer *et al.*, 2006; Armer *et al.*, 2009). Ideally, one would select the highest pixel density available (in this case, 4,096 × 1,768) to optimise feature characterisation during segmentation. However, due to time constraints such an approach is not possible, as increasing the pixel dimension dramatically increases the overall acquisition time for a volume. The choice of

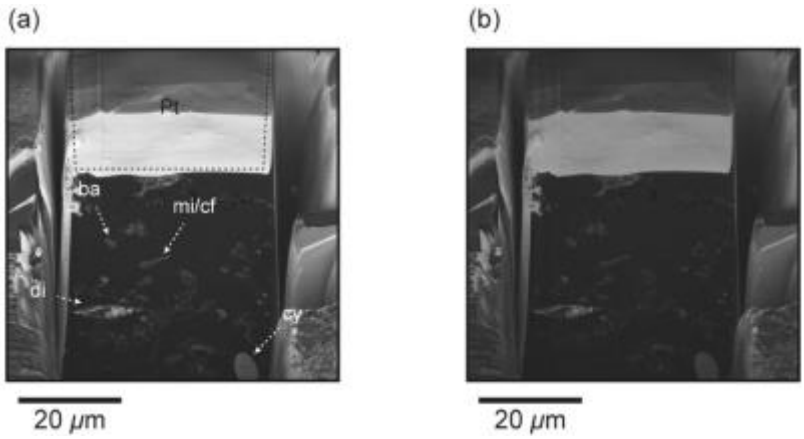

Figure AIII.1. Effect of electron beam conditions (specifically current) on image contrast and resolution: (a) BSE image obtained with an accelerating voltage of 3.5 kV and current of 373 pA, note that the contrast between different features within the image is good (e.g., organic cyanobacteria and inorganic clays) and that the edges of objects are relatively well defined; (b) Same image as in (a) but obtained with a beam current of 173 pA, note the contrast between different materials is poor compared to (a).

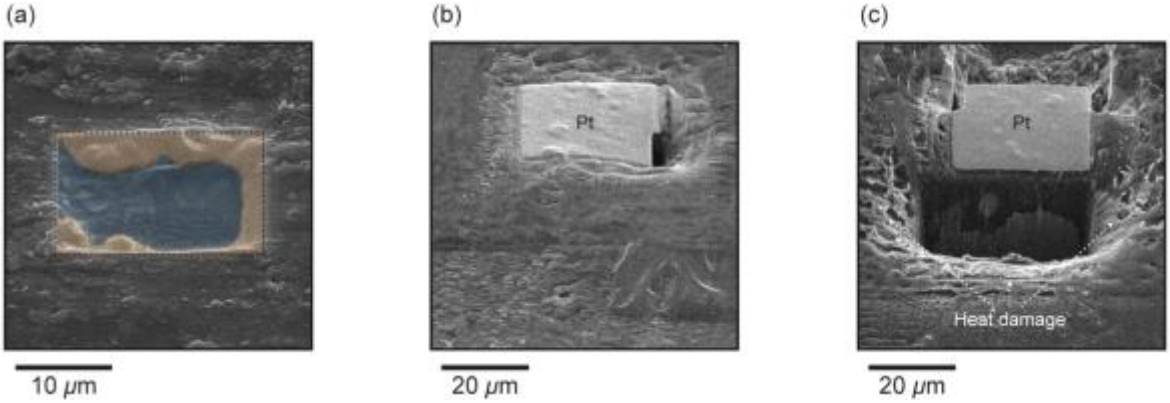

Figure AIII.2. The effects of selecting the wrong ion beam parameters: (a) An example of an unsuccessful platinum deposition over a selected RoI. Whilst some platinum has been deposited (areas highlighted in organe) milling damage to the surface has occurred (highlighted in blue); (b - c) Example of how the use of inappropriate ion beam currents can damage the sample. Image (b) shows the RoI prior to milling and (c) shows the area post ion beam erosion. Note the 'deflated' and pitted appearance of the surface in (b); this is the result of unwanted mass loss and phase change (e.g., melting) of the resin following milling with a high beam current.

parameters is thus dependant on first identifying what pixel resolution is sufficient to characterise the primary features of interest, bearing in mind the trade-off with the acquisition time. In most cases image dimensions of 1,024 × 884 pixels was found to be sufficient. However, for volume S5.1 a higher pixel density (2,048 × 1,768) was employed to investigate the nanometre-scale pore network within the floc.

- *Dwell Time* – SEM image quality is directly correlated with dwell time, with longer acquisition rates resulting in higher intensity SE/BSE signals per pixel, thus images with high signal-to-noise ratios. However, longer dwell times dramatically increase the frame rate and overall acquisition time for a volume, and can result in the build-up of negative charge on the milled surface and charging artefacts (Bushby *et al.*, 2011). To optimise acquisition time and mitigate against charging artefacts datasets were collected with a dwell times of 10 – 30 μs.

III.b. FIB Milling Parameters

The selection of the correct ion beam parameters (e.g., probe voltage and current) is essential to mitigate against FIB-induced surface damage and optimise image data quality (Bassim *et al.*, 2011; Bushy *et al.*, 2011). Prior to the acquisition of FIB-nt volumes ion beam milling conditions were explored. Based on these preliminary tests the milling conditions for each FIB-nt volume (Table 3.1) were selected as follows:

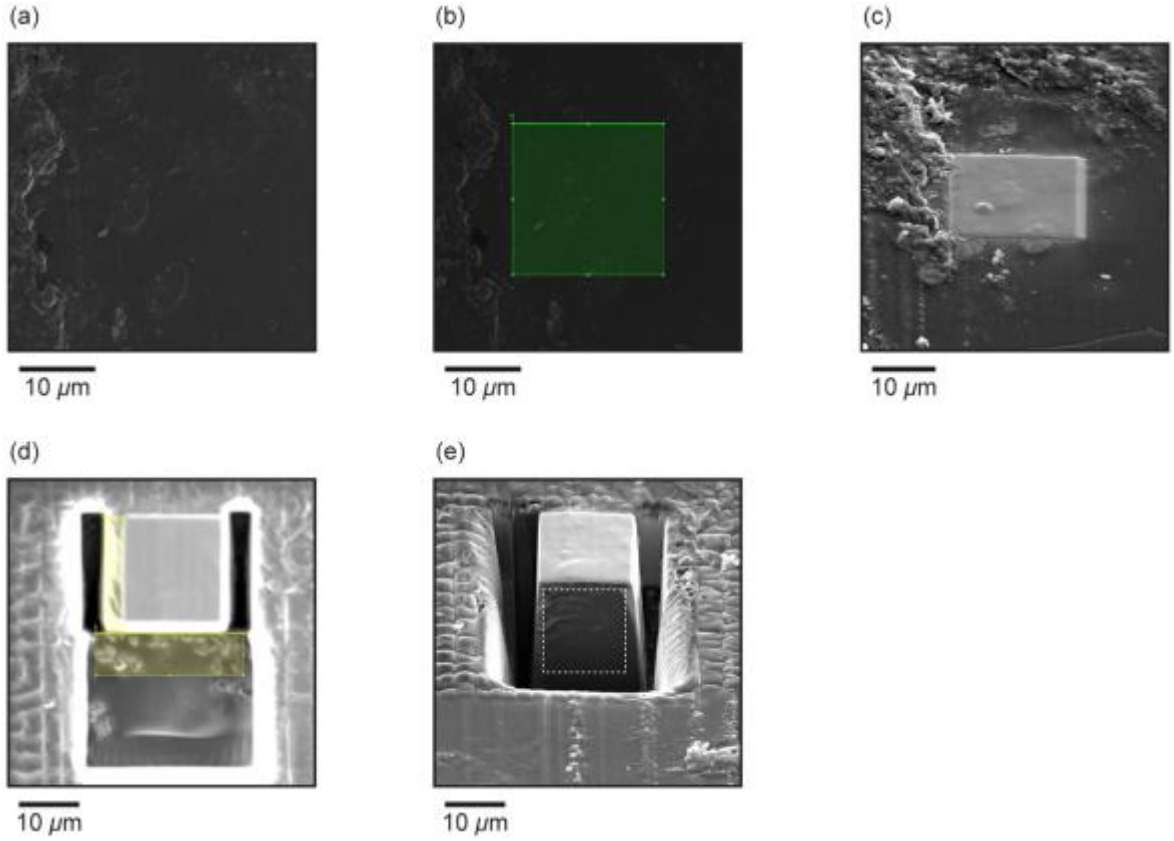

Figure AIII.3. The successful preparation of an RoI for FIB-nt: (a - b) Ion beam images of the RoI showing the pattern drawn for platinum deposition (b); (c) SEM-BSE image of the RoI post-platinum deposition; (d) Ion beam image of the RoI during the trenching procedure; (e) SEM-BSE image of the prepared cube ready for FIB-nt. The dashed line in (e) denotes the area of the image (stack) selected for reconstruction (see Appendix IV).

- The deposition of a smooth layer of platinum over the RoI helps prevents the pitting of the sample surface by stray ions and artefacts associated with milling fluctuations (i.e. curtaining, Figure AIII.2). An ion beam accelerating voltage of 30 kV and a current of 0.5 nA was found to be optimal for platinum deposition, regardless of the size of the pattern area. Higher beam current densities (1 – 3 nA) were tested, but resulted in the beam penetrating the platinum gas cloud and damaging the sample surface (see Figure AIII.3).

- For trenching the ion beam was usually operated at an accelerating voltage of 30 kV and 0.5 – 3 nA beam current. Higher beam currents (3 – 5 nA) were selected to reduce the time taken to erode large areas, but only if the area being eroded was at a distance > 4 μm from the RoI to mitigate against FIB-induced surface damage.

- During milling an accelerating voltage of 30 kV and current of 0.5 – 1 nA was selected for the ion beam. A high voltage is desirable because the beam is at its finest

spot size and most destructive (Bushby *et al*., 2011). Higher beam currents can be used to increase the speed at which slices are taken, however, caution must be exercised as this may result in instabilities in the beam. Beam currents >3 nA were found to be unsuitable for precise milling of larger sample faces (>40 μm) and often resulted in curtaining defects (e.g., Figure AIII.2).

Appendix IV– Supplementary Methodological Information

IV.a. FIB-nt and X-ray CT Data Reconstruction and Segmentation

- *FIB-nt Volume Reconstruction and Processing* – (See procedure described in Figure AIV.1). Reconstruction and processing methods for FIB-nt volumes followed the protocol outlined in Bushby *et al*. (2011), which employs the open source software Fiji/ImageJ. The initial stage of dataset reconstruction involved correcting the inherent misalignment between adjacent images and displacement problems caused by mechanical drift of the stage. Once the images were aligned a crop area was selected to isolate the 'volume of interest' VoI for reconstruction (see Figure AIII.3e and f). During image processing image contrast was manually adjusted to improve the distinction between material phases, and an edge preserving 3D median filter (kernel: 2 × 2 × 2) applied for noise reduction (Holzer *et al*., 2004).

- *X-ray CT Volume Reconstruction and Processing* – (See procedure described in Figure AIV.2). X-ray CT dataset reconstruction was followed the protocol outlined in the CT-Pro 3D user manual. To enable quantitative description and visualisation, the

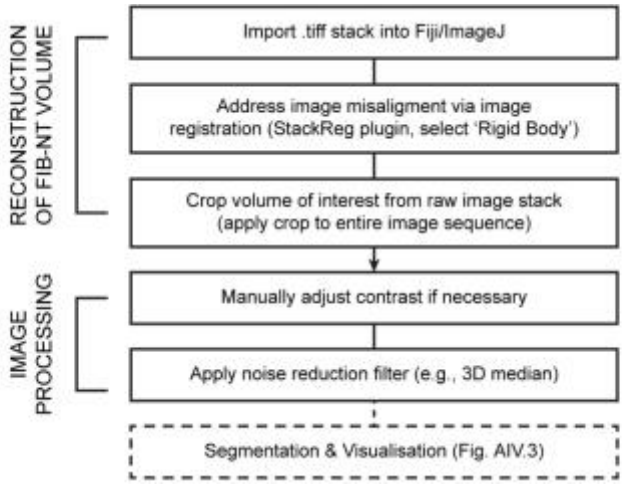

Figure AIV.1. Workflow outlining the steps taken in FIB-nt data reconstruction and processing in Fiji/ImageJ.

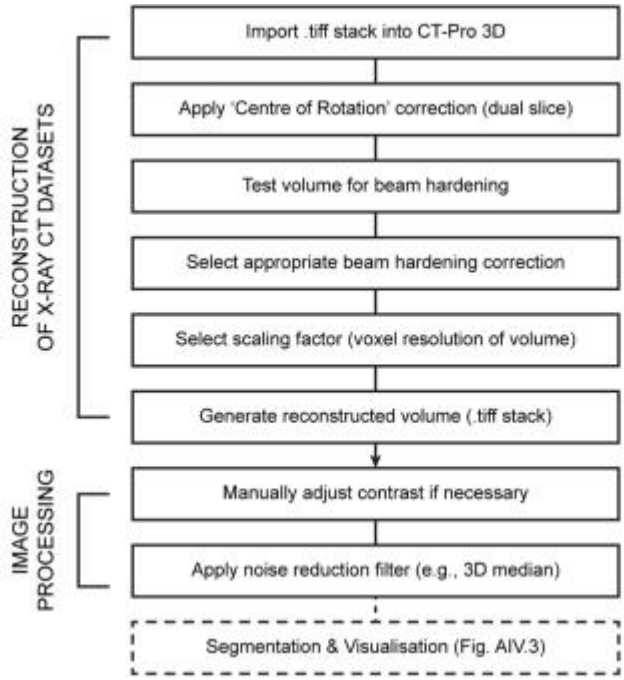

Figure AIV.2. Workflow outlining the steps taken in X-ray CT data reconstruction and processing in CT-Pro 3D and Fiji/ImageJ.

raw radiograms were initially subjected to a reconstruction algorithm to produce a stack of *z* slices. Corrections were then applied to tackle the effects of beam hardening and drift caused by mechanical instabilities in the stage (i.e. 'centre of rotation' corrections).

- *Volume Rendering, Segmentation and Visualisation* – (See procedure described in Figure AIV.3). Prior to segmentation the reconstructed and processed datasets were imported into the visualisation software Drishti (Limaye, 2006) to identify the primary material phases present within the volumes. Based on the preliminary visualisations, selected images from the image stack were imported into Fiji/ImageJ for segmentation using the semi-automated Trainable Weka Segmentation (TWS) plugin v2.1.0 (Arganda-Carreras, 2015). No more than 50 'labels' or training areas were identified for each volume to reduce the level of uncertainty in the segmentation result caused by large numbers of training areas (Arganda-Carreras, *pers. comm.*).

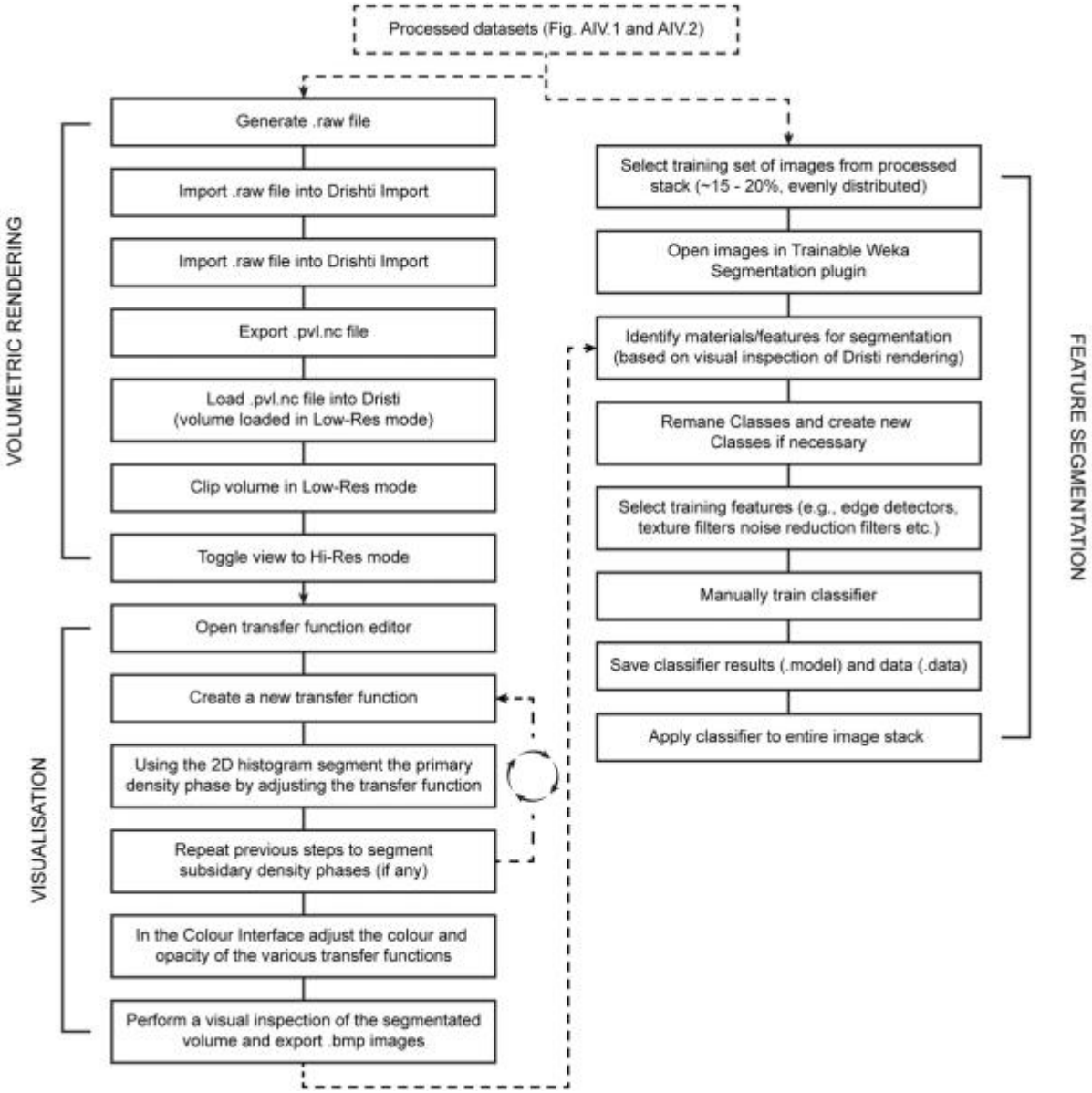

Figure AIV.3. Workflow outlining the steps taken during 3D data rendering, segmentation and visualisation.

IV.b. Generating STEM and SEM-SEM Image Montages

As discussed in §3.2.2 and 3.3.2, dark-field STEM and SEM-BSE image montages were generated using the Grid/Collection Stitching plugin in Fiji/ImageJ (Preibisch *et al*., 2009). Figure AIV.4 outlines the procedure followed in Fiji/ImageJ to create these image montages.

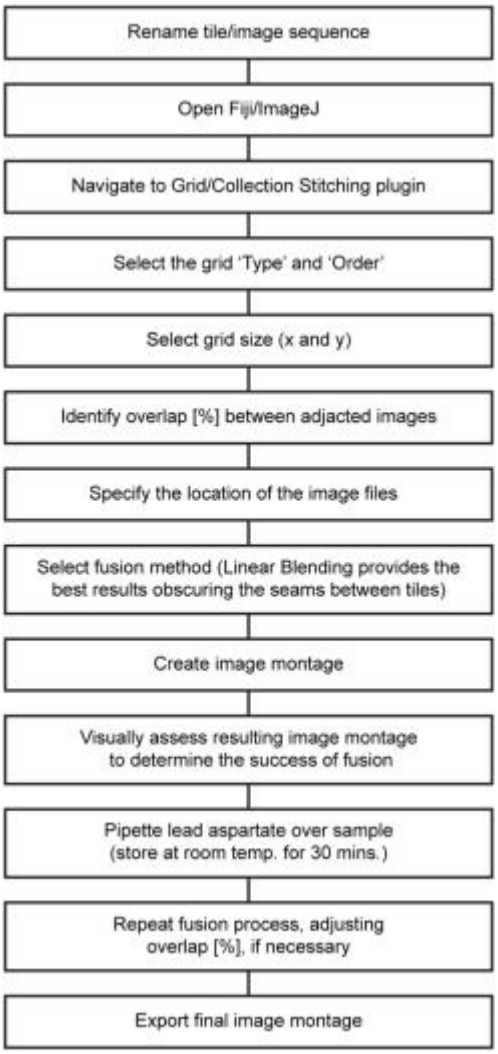

Figure AIV.4. Flowchart outlining the steps taken to create dark-field STEM and SEM-BSE image montages.

IV.c. Registration of Multi-Modal, Multi-Scale Datasets

Registration methods followed protocols described in the Avizo User Manual; the exact procedure followed for the registration of millimetre (X-ray CT), micrometre (SEM and FIB-nt) and nanometre-scale (STEM and TEM) datasets is provided in Figure AIV.5.

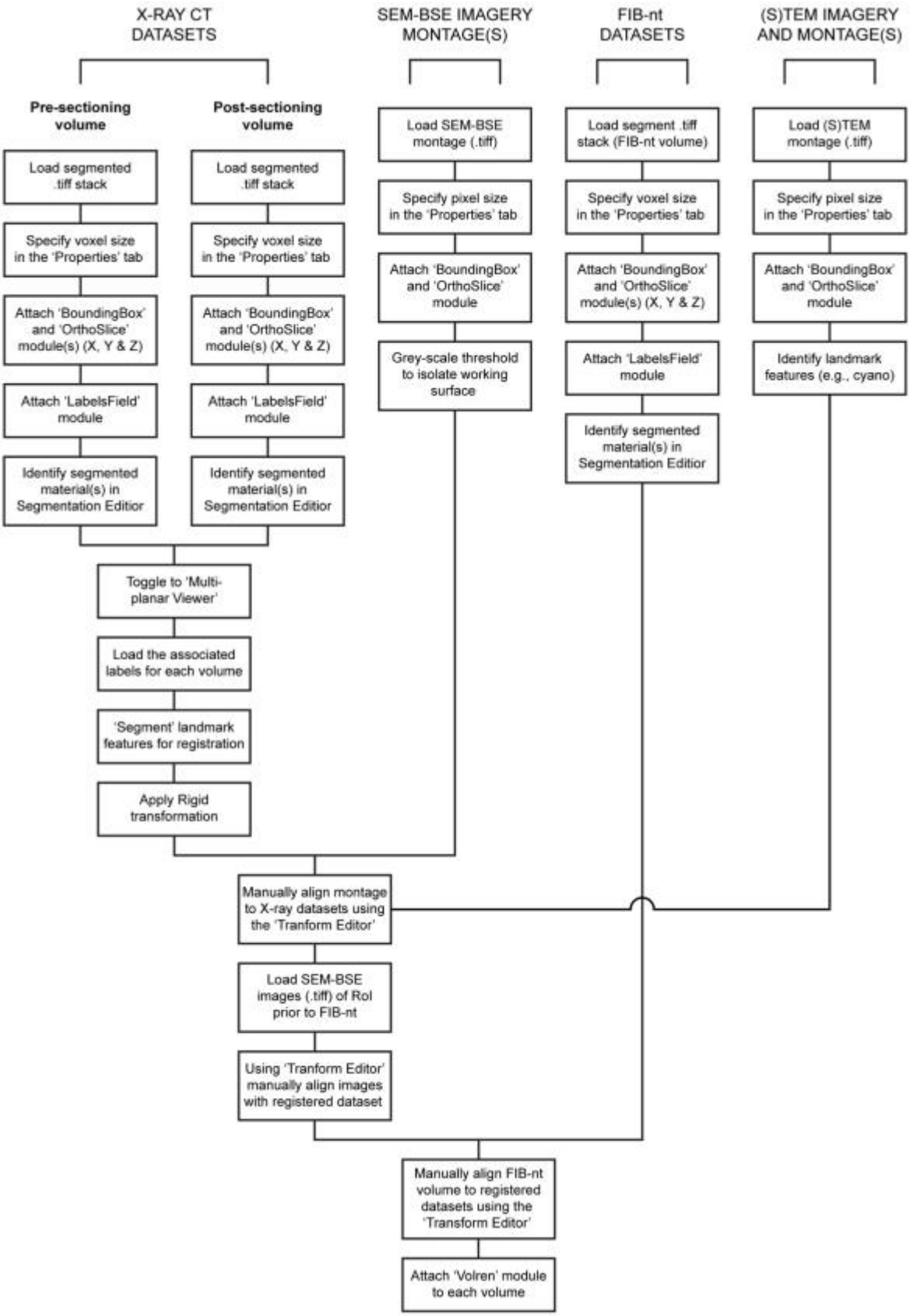

Figure AIV.5. Flow diagram outlining the major steps taken for the registration of the multi-scale datasets and their co-visualisation. *Please note a more detailed description of registration is provided in the Avizo User Manual.*